ABSTRACT

RIZVI, MEHEDI HASAN. Electrostatic Assembly and Magnetic Alignment of Multifunctional Gold Nanorods. (Under the direction of Dr. Joseph B. Tracy).

The vast knowledge of nanoparticles gained over the past 30 years allows researchers to synthesize different classes of nanomaterials with precise size, shape, and surface functionality. A significant need remains to develop improved methods for synthesizing multifunctional nanoparticles without sacrificing the properties of individual components. Multifunctional nanoparticles are promising for a wide range of applications. In comparison with single-component nanoparticles, multicomponent nanoparticles offer multifunctional properties, and novel effects may emerge from interactions among the components. Although there have been many advances in the synthesis of multicomponent nanoparticles, significant challenges remain, and demonstrating a general and robust fabrication technique could accelerate the development and realization of applications of multifunctional nanoparticles.

Ligands or functional molecules on the surfaces of nanoparticles can stabilize them against aggregation, and the tunable interactions between these surface moieties can be used to guide the self-assembly of multicomponent colloidal nanoparticles. In this dissertation, we developed an electrostatic self-assembly technique between anionic gold nanorods coated with bovine serum albumin and cationic satellite nanoparticles, such as Au and Fe_3O_4, coated with polyethyleneimine. Self-assembly of core/satellite nanoparticles based on electrostatic assembly offers vast tunability and reversibility through adjusting the electrostatic behaviors of the component nanoparticles by controlling the pH of the assembly environment. Detailed structural, optical and magnetic characterization are reported. Magnetic functionalization of gold nanorods make it possible to align them in applied magnetic fields, thus enabling magnetic-field control of their optical properties. The magnetochromic effect and controlled rotational and translational motion of the

magnetic gold nanorods allows their design and optimization for applications in imaging and sensing.

Electrostatic Assembly and Magnetic Alignment of Multifunctional Gold Nanorods

by
Mehedi Hasan Rizvi

A dissertation submitted to the Graduate Faculty of
North Carolina State University
in partial fulfillment of the
requirements for the degree of
Doctor of Philosophy

Materials Science and Engineering

Raleigh, North Carolina
2022

APPROVED BY:

_____	_____
Dr. Joseph B. Tracy Committee Chair	Dr. Wenpei Gao
_____	_____
Dr. Orlin D. Velev	Dr. Yaroslava G. Yingling

DEDICATION

I dedicate this to my parents Rubina Yasmin and Nurul Huq Molla, my brother Faisal Rabby, my daughter Mahreen Hasan and My wife Tasnim Jannat Swarna for their never ending love and support during the journey.

BIOGRAPHY

I was born on November 7, 1990, in Bangladesh. I attended Bangladesh University of Engineering and Technology for my undergraduate study. I graduated with Bachelor of Science in Materials Science and Engineering in 2013. I also achieved my Master of Science in Ceramic Engineering from the same institution in 2015. In my master's thesis I worked on synthesis and characterization of multiferroic $BiFeO_3$ nanoparticles. I moved Raleigh and started my PhD in Materials Science and Engineering in spring 2018. I joined Dr. Tracy's research group in summer 2018 to work on projects on nanomaterials synthesis and self-assembly.

ACKNOWLEDGMENTS

I am indebted to Prof. Joseph Tracy for his immense support and guidance in the last four and half years in pursuing my PhD journey. I greatly admire his understanding and respect for the timeline to finish a job. He importantly ensures freedom in doing experiments that I believe helped me to grow as an independent researcher. However, he is very proactive in discussing and offers excellent suggestions and ideas to keep the research smooth and productive.

I am thankful to current and previous lab members of our research group who were always helpful and responsive to my queries. I would especially like to thank Brian Lynch for patiently train me on many of the synthesis techniques that I have utilized in this dissertation. I would also like to mention Melanie for her immense help in the lab for the last four years.

I am very thankful to every member of AIF who was always supportive. It is worth mentioning Dr. Chris Winkler, Toby Tung and Dr. Aaron Bell for their great help with TEM.

I am grateful to my parents and Brother for their sacrifice and effort to bring me where I am now. I want to especially thank Tasnim Swarna, who always encourages me to succeed and supports me in tough times. Thank you very much for taking care of Mahreen for days and nights when I was busy in the lab.

I would also like to thank Abida Sizni and Mahfuza Neeshat for being amazing and supportive neighbors. Thank you for watching Mahreen when Swarna and I were busy in school.

TABLE OF CONTENTS

LIST OF FIGURES

CHAPTER 1. Introduction

1.1 Nanoparticles

Nanotechnology is on the verge of making great breakthroughs in almost every field of science from fundamental developments to engineering applications for sustainability and improved quality of life. The term "nano" is of Greek origin and means something with a very small size. Based on the scale of a nanometer (10^{-9} m), nanoscale materials are defined as the structure, device, or system with size of 1-100 nm in at least one dimension.[1] Nanoscale materials exhibit novel optical, electrical and magnetic properties compared to their bulk counterparts because of the effects of a large proportion of surface atoms and quantum size effects.[2] The concept of manipulating matter on the nanoscale is a relatively recent topic that gained significant attention in Nobel Laurate Richard Feynman's famous lecture in 1959, "There's plenty of room at the bottom."[3] While much progress in manipulating materials on the nanoscale has been realized, many opportunities and challenges remains for achieving the Feynman's vision. Specifically, wet-chemical methods of nanofabrication have been established for many systems to control the size, shape and properties of nanomaterials. There is great interest in developing methods for synthesizing and assembling multicomponent nanoscale materials with high precision and on a large scale for applications.[4,5]

Plasmonic and magnetic nanoparticles (NPs) are two of the most studied classes of nanomaterials because of widespread biomedical and optoelectronic device applications. The applications for plasmonic colloidal NPs include plasmonic heating, photothermal therapy and imaging,[6,7] biosensing,[8,9] plasmonic polarimetry,[10,11] plasmonic lasing,[12,13] energy conversion devices,[14] artificial molecules,[15] plasmonic nanozymes,[16,17] and surface-enhanced fluorescence.[18] Magnetic NPs with superparamagnetic properties have biomedical applications in bioimaging

techniques, such as magnetic particle imaging,[19,20] magnetic resonance imaging,[21,22] hyperthermia,[23,24] drug delivery.[25-27]

1.2 Plasmonic NPs

Plasmonic NPs are metallic or heavily doped semiconductor NPs that interact with photons via a localized surface plasmon resonance (SPR).[28] When the size of the metallic NPs is much smaller than the wavelength of incident light, the electric field component of light drives and displaces the electron cloud of the NP, resulting in an oscillating polarization. The electrons in the metal NP move to oppose the polarization of the oscillating electric field of incident light; this movement is maximized when the frequency of light overlaps with inherent oscillating frequencies of electrons in NPs (Figure 1.1).[29] At the frequency of the SPR, NPs strongly absorb light. The intensity and wavelength of the SPR depend on the composition, size, shape and local dielectric environment of plasmonic NPs.

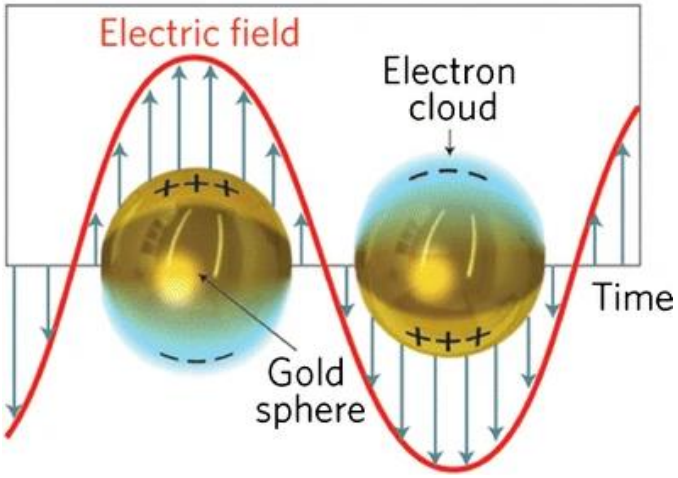

Figure 1.1. Schematic for the localized surface plasmon resonance on the surface of metallic NPs.[29]

Noble metal NPs like gold NPs are most widely studied plasmonic NPs because of their chemical inertness and methods for tuning the SPR by controlling the size and shape of the NPs.[30]

For example, isotropic spherical gold NPs exhibit one SPR mode, while gold nanorods exhibit longitudinal and transverse SPR modes corresponding to electrons oscillating along the long axis along a short axis. Understanding the relationship between the structure of the NP and the SPR makes it possible to design the structure for optical properties that are desired for a wide range of applications.[31] For instance, recent synthetic developments allow fabrication of complex, multicomponent plasmonic NPs, where coupling between two nearby components modifies the plasmon modes and introduces large electric field enhancements. Coupled plasmonic NPs with large field enhancements have applications in surface enhanced Raman scattering (SERS),[32-35] amplification of fluorescence,[36-38] enhanced photocurrent and light emission.[39,40]

1.2.1 Synthesis of Gold NPs

The use of gold NPs in medicine and for decoration dates to ancient times.[41,42] A well-known example is the Lycurgus Cup, which contains gold NPs dispersed in glass and changes color when illuminated from different directions (Figure 1.2).[43]

Figure 1.2. Lycurgus cup under (left) reflected and (right) transmitted light.[43]

The first scientific report on the synthesis of gold NPs was published nearly two centuries ago in 1857 by Michael Faraday, who found that gold salts can be reduced with phosphorus in presence of carbon disulfide, resulting in fine gold particles with a beautiful ruby red color.[44] Gustav Mie in 1908 first mathematically correlated this brilliant ruby color with the absorption scattering of light by the colloidal gold NPs.[45]

Most of the current methods for synthesizing gold NPs follow a similar approach of reducing gold salt in presence of capping agents to avoid aggregation, and altering the ratio of reactants provides control over the size and shape of the NPs.[1] In 1951, Turkevich *et al*. first demonstrated detailed synthetic control and structural analysis of gold NPs.[46] In the citrate reduction method they reported, aqueous dispersions of gold NPs with as average size of 20 nm we synthesized by reducing $HAuCl_4$ with sodium citrate. Frens *et al*. used the Turkevich method in 1973 to demonstrate size-controlled synthesis of citrate stabilized gold NPs by varying the amount of reactants to control the nucleation and growth steps.[47]

In 1981, Schmid *et al.* reported tiny phosphine-stabilized gold clusters with well-defined size (1.4 ± 0.4 nm) and molecular weight, having the molecular formula, $Au_{55}(PPh_3)_{12}Cl_6$. Another breakthrough in gold NPs synthesis is employing alkanethiols of different chain length to stabilize the NPs, developed Mulvaney *et al*.[48] Later, Brust et al. demonstrated a two-phase (water-toluene) synthesis of thiolate-functionalized gold NPs.[49] In the last few years, seeded growth techniques have received significant attention for obtaining monodisperse gold NPs through control of nucleation and growth by adjusting synthetic parameters, including selection of the solvent and ligand (Figure 1.3).[50-53]

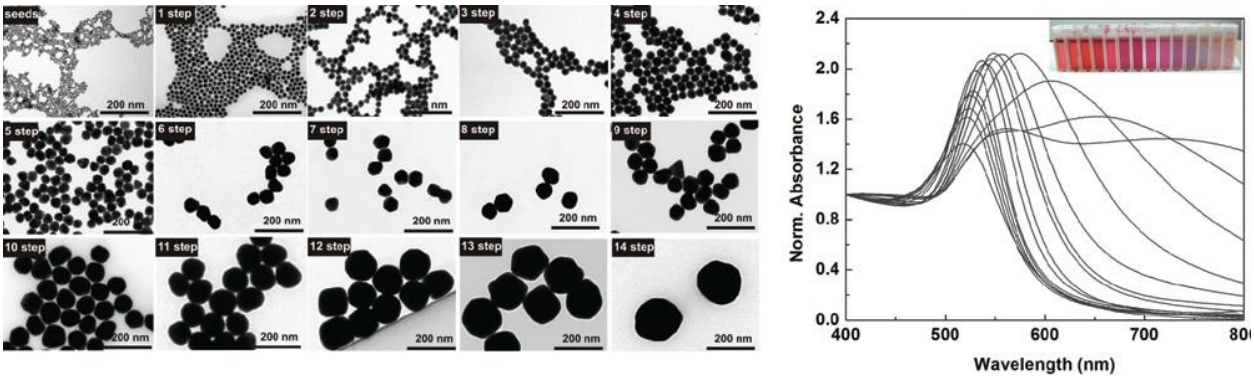

Figure 1.3. Monodisperse citrate-stabilized gold NPs of different sizes up to 200 nm obtained by kinetically controlled seeded growth.[53]

1.2.2 Synthesis of Gold Nanorods

Gold nanorods (GNRs) have received significant attention because of their tunable SPR, which is useful for biomedical applications and optoelectronics. The synthesis and plasmonic properties of GNRs have thus been extensively investigated. Martin *et al.* pioneered techniques to prepare GNRs by electrochemical reduction, but the technique is limited by low yield and large particle size.[54] Wang *et al.* reported the synthesis of smaller GNRs with distinct transverse and longitudinal SPRs by electrochemical oxidation of gold plates the in presence of cetyltrimethylammonium bromide (CTAB).[55]

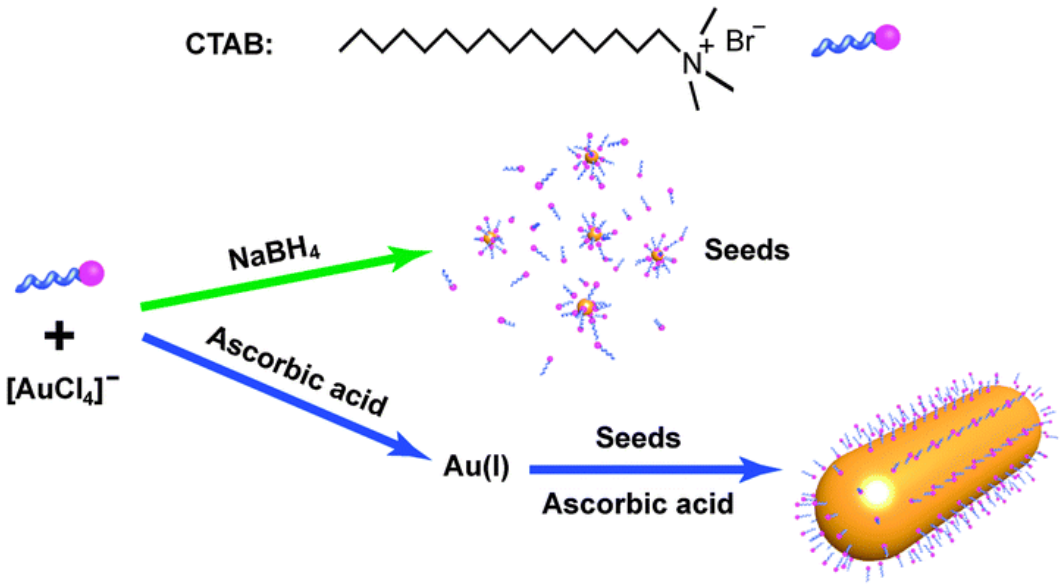

Figure 1.4. Schematic illustration for the seeded growth of GNRs.[56]

Murphy *et al*.[57] and El-Sayed *et al*.[58] achieved a major breakthrough soon thereafter by demonstrating high-yield colloidal synthesis of GNRs based on seeded growth. In this method, small gold NPs are prepared by reducing $HAuCl_4$ with $NaBH_4$, which are added to a growth solution containing partially reduced Au(I) with $AgNO_3$ and surfactant, like CTAB (Figure 1.4). The surfactant inhibits agglomeration and forms rod-shapes micelles that may serve as soft templates for growth into rod shapes.[57] The aspect ratio of GNRs determines their optical properties, and the longitudinal SPR can be tailored across the visible and near infrared spectra (Figure 1.5).[6] The aspect ratio of GNRs can be controlled by altering synthetic parameters, for example the relative amount of seed to $HAuCl_4$ and concentration of impurity ions, such as Ag(I). Although the exact mechanism is yet to be fully established, Ag(I) is thought to be preferentially binds to (110) facets and slows down addition of gold atoms. The gold seed can grow preferentially in the (100) facets, leading to anisotropic axial growth.[57,59] Much effort has been reported to tune the size and shape of GNRs by adjusting the synthetic parameters, for example surfactant composition, temperature, structure of seed and pH of the growth solution.[58-63]

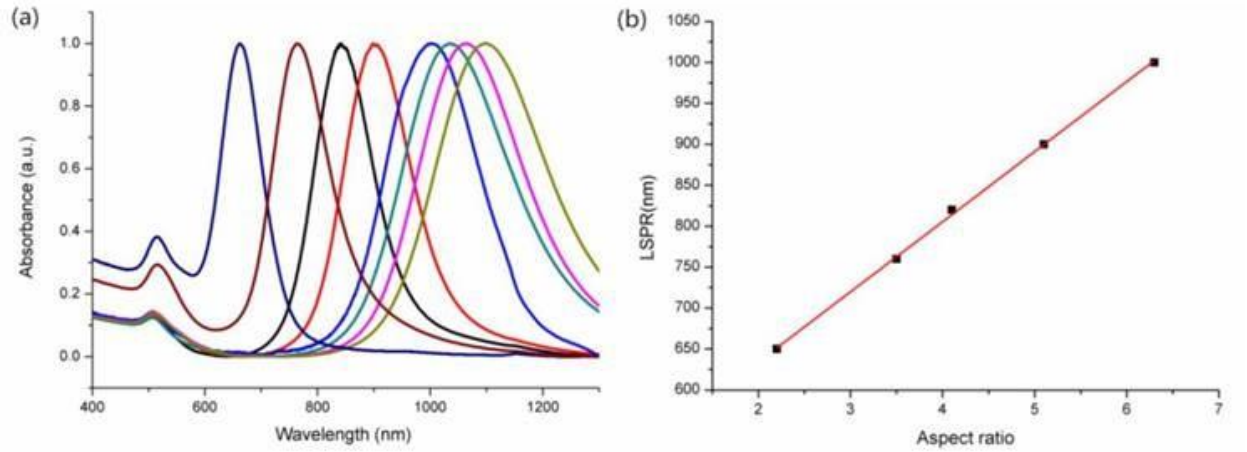

Figure 1.5. (a) Extinction spectra of GNRs with longitudinal SPR ranging from 650 nm to 1100 nm. (b) The relationship between aspect ratio and longitudinal SPR.[64]

The seed-mediated method developed by El-Sayed and coworkers was a revolutionary advance but utilizes only ~30% of Au precursor and thus remains inefficient. Kozek *et al.* later developed a technique to inject reducing agent (aqueous ascorbic acid) continuously to fully reduce the remaining Au(I) to Au(0) and to deposit it onto the GNRs.[65] The injection rate of the ascorbic acid has a significant effect on the size and shape of the GNRs. Faster injection allows gold to deposit preferentially onto the tip of the GNRs and thus yields higher aspect ratios. Decreasing the injection rate makes deposition of Au more uniform and thus decreases the aspect ratio. Moreover, the technique allowed upscaling of the synthesis to a 1 L of solution containing ~190 mg of gold.

1.2.3. Assembly of GNRs

The assembly of GNRs into different architectures is of significant interest for their novel optical properties. Novel sensing applications have been devised based on the unique optical properties of assembled GNRs. Techniques for assembling GNRs can broadly be classified into three categories: assembly on a substrate, assembly in polymer composite and assembly in solution.

A common approach for attaching GNRs to a substrate utilizes electrostatic attraction between cationic CTAB-GNRs and an anionic substrate. Murphy *et al.* assembled GNRs by immersing a glass substrate functionalized with self-assembled monolayers of 16-mercaptohexadecanoic in a CTAB-GNR solution.[66] Immobilization of the GNRs was attributed to electrostatic interactions between the carboxylic acid cationic CTAB. Functionalizing the surface with anionic poly(sodium styrenesulfonate) allows similar immobilization of GNRs.[67] CTAB-GNRs have also been chemisorbed on 1,6-hexanedithiol-modified gold electrodes.[68] Drying a concentrated solution containing GNRs on a surface can drive assembly without any additives and results in an assembled ring of GNRs of 2-5 mm in diameter.[69] Fan *et al.* demonstrated large-area assembly of vertically aligned, hexagonal closed packed GNRs by a controlled evaporation deposition process. The assembled surface exhibits superior SERS signal for molecular detection at low concentrations of ~10^{-15} M.[70]

The assembly of GNRs in polymer matrices is crucial for many applications. Van der Zande *et al.* dispersed GNRs in poly(vinyl alcohol) (PVA) films and aligned them by stretching the films.[71] The aligned GNRs in PVA become sensitive to polarized light. The electric field of polarized light parallel (perpendicular) to the stretching direction only excites the longitudinal (transverse) SPR. Complete alignment was reported after stretching the films to 4-6× the original length. Similar alignment of GNRs in stretched polymer films with detailed characterization was reported later by Perez-Juste *et al.*[72] and Murphy *et al.*[73]

Assembly of GNRs in solution allows scalability and reversibility that is not possible on solid substrates. A well-studied technique is assembling GNRs with nematic and smectic ordering through coalignment with liquid crystals.[74-76] External electric and magnetic field-induced alignment is promising because of the advantages of remotely controlled, dynamic assembly. Van

der Zande *et al.* postulated that GNRs could be aligned under electric fields to control the longitudinal SPR in polarized light.[77] Later studies demonstrated optical and structural characterization of GNRs assembled under electric fields.[78-80] Yin *et al.* demonstrated techniques to attach magnetic phases to GNRs or grew GNRs on magnetic phase to align them under magnetic fields (Figure 1.6).[81,82] However, these approaches result in high background and a broad LSPR, which is discussed in more detail in Chapter 4.

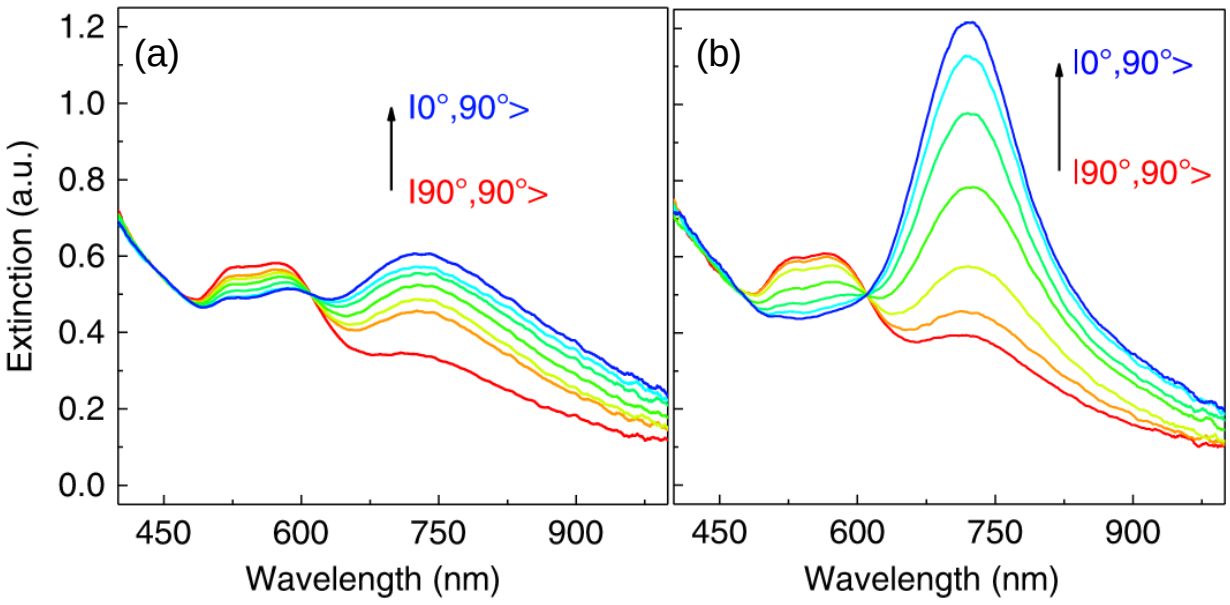

Figure 1.6. Tuning the extinction spectra of magnetic GNRs by (a) unpolarized and (b) polarized (b) light. Electric fields oriented parallel (perpendicular) to long axis of GNRs excite the longitudinal (transverse) SPR.[82]

1.3. Magnetic NPs

Developments in methods for synthesizing magnetic NPs over the past two decades have enabled many fundamental studies and technological applications. For example, magnetic NPs have found applications in catalysis, biomedicine, bioimaging, environmental remediation and data storage. [83] Superparamagnetic iron oxide NPs, and magnetite (Fe_3O_4) and maghemite (γ-

Fe_2O_3) NPs in particular, have been of great interest for their stability, biocompatibility, and size-dependent magnetic properties.[84]

Bulk Fe_3O_4 is multidomain ferrimagnet with a Curie temperature of 858 K. Fe_3O_4 NPs with sizes below ~100 nm become single-domain magnets and exhibit maximum coercivity near the size limit for single-domain behavior. As the Fe_3O_4 NP size decreases, the coercivity diminishes. For sizes below ~20 nm thermal energy at room temperature is sufficient to randomize the magnetization of Fe_3O_4 NPs, which is superparamagnetic behavior (Figure 1.7).[84] The highest temperature for ferromagnetic behavior, above which the NPs exhibit superparamagnetic behavior, is the superparamagnetic blocking temperature (T_B), which is a function of NP size. T_B is expressed as $T_B = KV/25k_B$, where K is the magnetocrystalline anisotropy constant which depends on the composition and structure of the NPs, V is the volume of a single NP, and k_B is the Boltzmann constant.

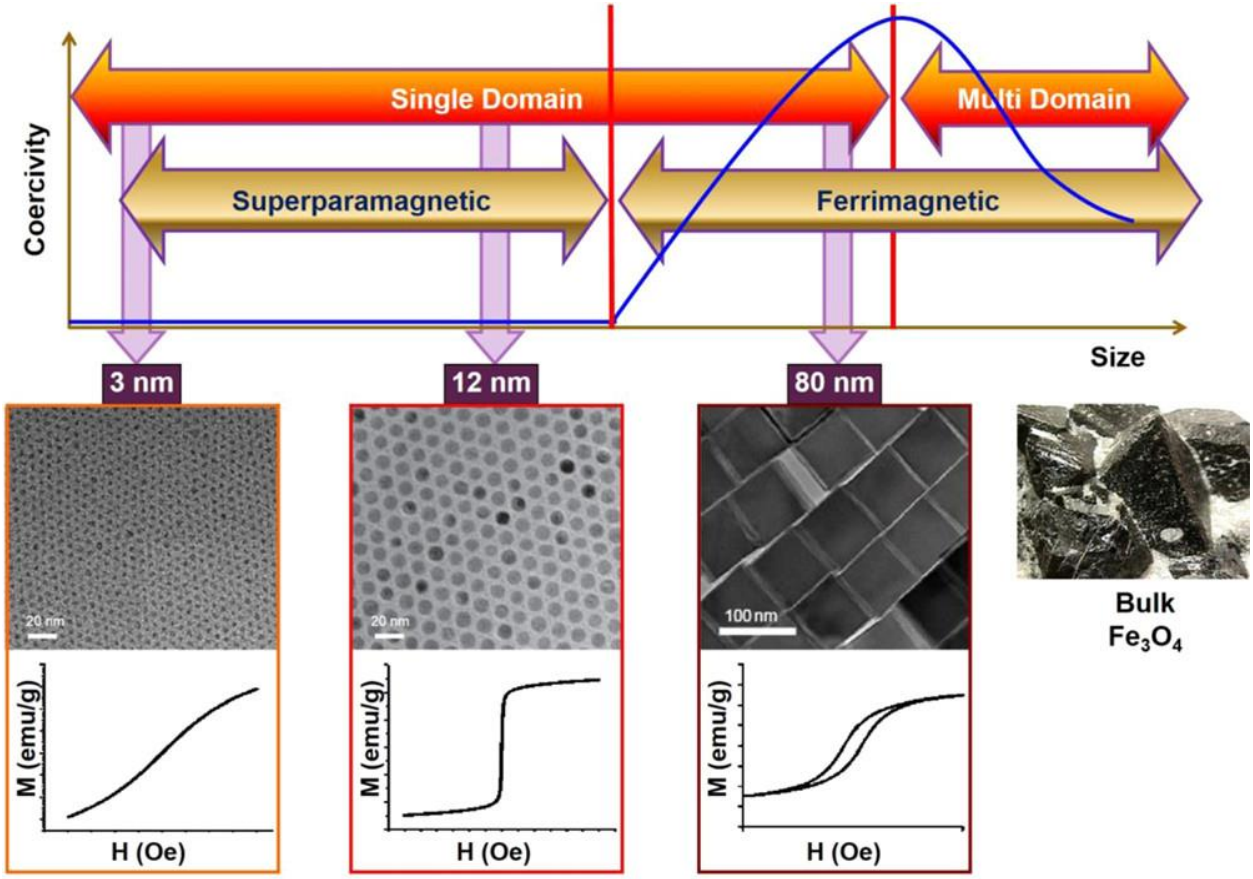

Figure 1.7. Size-dependent magnetic properties of ferrimagnetic Fe_3O_4 NPs.[84-86]

The most widely used technique for measuring T_B is dc magnetometry, where a zero-field-cooled measurement is performed. In a typical experiment, the sample is cooled to ~2-5 K without magnetic field, then a small field (~100 Oe) is applied, followed by measuring while heating back to room temperature. As the temperature increases, the thermal energy helps relax the frozen moments and allows the moments to align with the applied magnetic field. The magnetization increases until reaching a maximum at T_B. With further increasing temperature, the thermal energy also overcomes alignment with the applied magnetic field, thus randomizing the moment and gradually decreasing the magnetization.

1.3.1. Synthesis of Fe_3O_4 NPs

A common approach for synthesizing Fe_3O_4 NPs is thermal decomposition of metal precursors, most frequently organometallic complexes that can readily undergo thermal decomposition because of their metastable nature.[87] Sun *et al.* reported thermal decomposition of $Fe(acac)_3$ in the presence of 1,2-hexadecanediol, oleylamine, and oleic acid in phenyl ether or benzyl ether, resulting in Fe_3O_4 NPs with tunable size, good crystallinity and controlled magnetic properties.[88-90] In those studies, oleylamine and oleic acid serve as ligands and 1,2-hexadecandiol as a reducing agent. Peng *et al.* reported a general decomposition technique to obtain nearly monodisperse Fe_3O_4 NPs with sizes adjustable in the range of 3-50 nm by pyrolysis of metal fatty acid salts in hydrocarbon solvents like octadecene, eicosane, and tetracosane.[91]

Hyeon *et al.* demonstrated a similar thermal decomposition approach for preparing monodisperse iron oxide NPs.[92] Their approach involves thermal decomposition of nontoxic and inexpensive iron oleate, which was prepared by reacting $FeCl_3$ and Na oleate (Figure 1.8). Thermal decomposition of Na oleate at 240-340 °C in different hydrocarbon solvents, including 1-hexadecene, octyl ether, 1-octadecene, 1-eicosene, or trioctylamine, provided size control over the range of 5-22 nm. Despite precise size control, the decomposition of iron oleate in these solvents often results in NPs with mixed polymorphs of iron oxide and unexpected magnetic properties. Chen *et al.* modified the above technique and suggested that use of mixtures of alkenes and benzyl ether as the solvent can avoid wüstite (FeO) formation and achieve crystalline Fe_3O_4 NPs.[93]

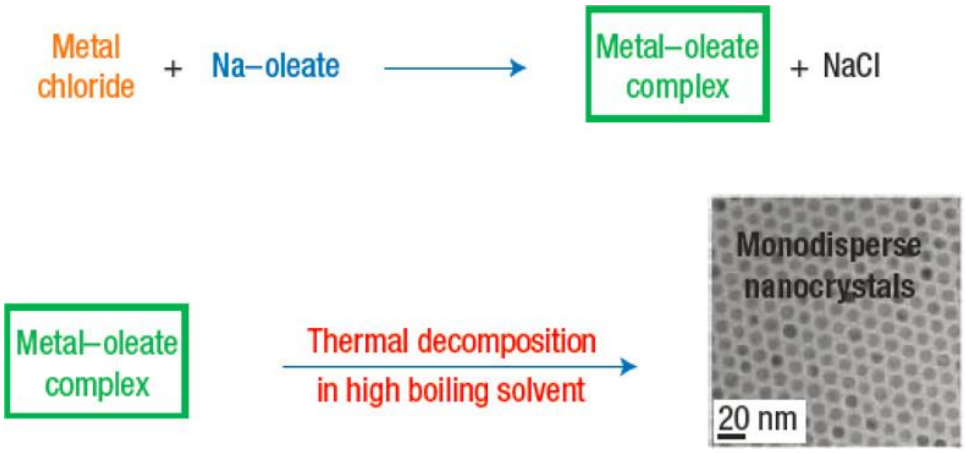

Figure 1.8. Schematic of the preparation of Fe-oleate complex and its decomposition in the synthesis of monodisperse, 12-nm Fe_3O_4 NPs.[92]

1.4. Multicomponent Plasmonic NPs

A wide range of plasmonic nanostructures have been developed in last few decades. Compared to single-component nanostructures, multicomponent nanostructures composed of heterogenous building blocks can possess multifunctional properties that cannot be obtained from single component. Multicomponent NPs can be defined as hybrid nanostructures composed of nanoscale domains that are distinct in composition, size or shape.[94] Although multicomponent nanostructures have been intensively explored, achieving precise control and scalable synthesis of multifunctional plasmonic NPs remains challenging.[94] Plasmonic multicomponent NPs consist of noble metal NPs in conjunction with other metal, dielectric, or semiconducting NPs to exhibit synergistic and novel plasmonic, radiative and magnetic properties. The new functionalities present in hybrid NPs can come from the combination of uncoupled components or coupling among multiple components. For example, plasmon coupling between core and satellite NPs in multicomponent NPs can create hot spots with enhanced electric fields that give rise to dramatically increased SERS sensitivity.[95,96] In another report, plasmonic gold nanorod (GNR) cores enhanced the photoluminescence of satellite quantum dots by 5×.[97] Magnetically

functionalized plasmonic NPs bring allow manipulation with magnetic fields, which is important for many applications like bimodal imaging and therapy.[98]

1.5. Electrostatic Core/Satellite Assembly

A common approach for fabricating multifunctional NPs relies on interactions between ligand-functionalized NPs.[99] Interactions guiding assembly can include hydrogen bonding, molecular crosslinking, and electrostatic interactions. Long-range electrostatic interactions between oppositely charged NPs and substrates have been utilized to fabricate NP monolayers,[66,100] superlattices[101] and core/satellite assemblies (Figure 1.9).[102-104]

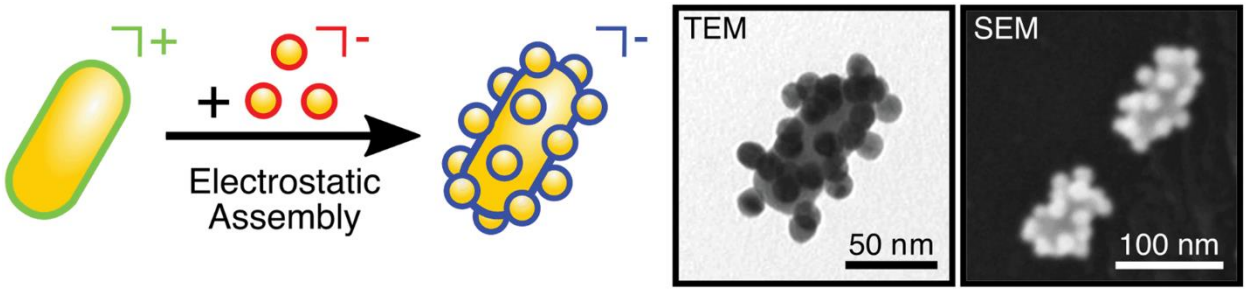

Figure 1.9. Schematic of electrostatic core/satellite assembly of cationic GNR core and anionic satellite gold NPs with experimental TEM and SEM images.[104]

1.6. References

(1) Dreaden, E. C.; Alkilany, A. M.; Huang, X.; Murphy, C. J.; El-Sayed, M. A. The golden age: gold nanoparticles for biomedicine. *Chem. Soc. Rev.* **2012**, *41*, 2740-2779.

(2) Jin, R.; Zeng, C.; Zhou, M.; Chen, Y. Atomically Precise Colloidal Metal Nanoclusters and Nanoparticles: Fundamentals and Opportunities. *Chem. Rev.* **2016**, *116*, 10346-10413.

(3) Feynman, R. P. There's Plenty of Room at the Bottom. *Engineering and Science* **1960**, *23*, 22-36.

(4) Grzelczak, M.; Liz-Marzán, L. M.; Klajn, R. Stimuli-responsive self-assembly of nanoparticles. *Chem. Soc. Rev.* **2019**, *48*, 1342-1361.

(5) Dijkstra, M.; Luijten, E. From predictive modelling to machine learning and reverse engineering of colloidal self-assembly. *Nat. Mater.* **2021**, *20*, 762-773.

(6) Huang, X.; El-Sayed, I. H.; Qian, W.; El-Sayed, M. A. Cancer Cell Imaging and Photothermal Therapy in the Near-Infrared Region by Using Gold Nanorods. *J. Am. Chem. Soc.* **2006**, *128*, 2115-2120.

(7) Hogan, N. J.; Urban, A. S.; Ayala-Orozco, C.; Pimpinelli, A.; Nordlander, P.; Halas, N. J. Nanoparticles Heat through Light Localization. *Nano Lett.* **2014**, *14*, 4640-4645.

(8) Anker, J. N.; Hall, W. P.; Lyandres, O.; Shah, N. C.; Zhao, J.; Van Duyne, R. P. Biosensing with plasmonic nanosensors. *Nat. Mater.* **2008**, *7*, 442-453.

(9) Shrivastav, A. M.; Cvelbar, U.; Abdulhalim, I. A comprehensive review on plasmonic-based biosensors used in viral diagnostics. *Commun. Biol.* **2021**, *4*, 70.

(10) Kleemann, M.-E.; Mertens, J.; Zheng, X.; Cormier, S.; Turek, V.; Benz, F.; Chikkaraddy, R.; Deacon, W.; Lombardi, A.; Moshchalkov, V. V.; Vandenbosch, G. A. E.; Baumberg,

J. J. Revealing Nanostructures through Plasmon Polarimetry. *ACS Nano* **2017**, *11*, 850-855.

(11) Martínez, A. Polarimetry enabled by nanophotonics. *Science* **2018**, *362*, 750-751.

(12) Azzam, S. I.; Kildishev, A. V.; Ma, R.-M.; Ning, C.-Z.; Oulton, R.; Shalaev, V. M.; Stockman, M. I.; Xu, J.-L.; Zhang, X. Ten years of spasers and plasmonic nanolasers. *Light Sci. Appl.* **2020**, *9*, 90.

(13) Wang, D.; Bourgeois, M. R.; Guan, J.; Fumani, A. K.; Schatz, G. C.; Odom, T. W. Lasing from Finite Plasmonic Nanoparticle Lattices. *ACS Photonics* **2020**, *7*, 630-636.

(14) Wang, L.; Hasanzadeh Kafshgari, M.; Meunier, M. Optical Properties and Applications of Plasmonic-Metal Nanoparticles. *Adv. Funct. Mater.* **2020**, *30*, 2005400.

(15) Wang, H.; Brandl, D. W.; Nordlander, P.; Halas, N. J. Plasmonic Nanostructures: Artificial Molecules. *Acc. Chem. Res.* **2007**, *40*, 53-62.

(16) Zhang, Y.; Villarreal, E.; Li, G. G.; Wang, W.; Wang, H. Plasmonic Nanozymes: Engineered Gold Nanoparticles Exhibit Tunable Plasmon-Enhanced Peroxidase-Mimicking Activity. *The Journal of Physical Chemistry Letters* **2020**, *11*, 9321-9328.

(17) Mosquera, J.; Zhao, Y.; Jang, H.-J.; Xie, N.; Xu, C.; Kotov, N. A.; Liz-Marzán, L. M. Plasmonic Nanoparticles with Supramolecular Recognition. *Adv. Funct. Mater.* **2020**, *30*, 1902082.

(18) Tu, S.; Rioux, D.; Perreault, J.; Brouard, D.; Meunier, M. Fluorescence and Scattering Dual-Mode Multiplexed Imaging with Gold–Silver Alloy Core Silica Shell Nanoparticles. *J. Phys. Chem. C* **2017**, *121*, 8944-8951.

(19) Gleich, B.; Weizenecker, J. Tomographic imaging using the nonlinear response of magnetic particles. *Nature* **2005**, *435*, 1214-1217.

(20) Wu, L. C.; Zhang, Y.; Steinberg, G.; Qu, H.; Huang, S.; Cheng, M.; Bliss, T.; Du, F.; Rao, J.; Song, G.; Pisani, L.; Doyle, T.; Conolly, S.; Krishnan, K.; Grant, G.; Wintermark, M. A Review of Magnetic Particle Imaging and Perspectives on Neuroimaging. *AJNR Am. J. Neuroradiol.* **2019**, *40*, 206.

(21) Cheon, J.; Lee, J.-H. Synergistically Integrated Nanoparticles as Multimodal Probes for Nanobiotechnology. *Acc. Chem. Res.* **2008**, *41*, 1630-1640.

(22) Na, H. B.; Song, I. C.; Hyeon, T. Inorganic Nanoparticles for MRI Contrast Agents. *Adv. Mater.* **2009**, *21*, 2133-2148.

(23) Liu, X.; Zhang, Y.; Wang, Y.; Zhu, W.; Li, G.; Ma, X.; Zhang, Y.; Chen, S.; Tiwari, S.; Shi, K.; Zhang, S.; Fan, H. M.; Zhao, Y. X.; Liang, X.-J. Comprehensive understanding of magnetic hyperthermia for improving antitumor therapeutic efficacy. *Theranostics* **2020**, *10*, 3793-3815.

(24) Gavilán, H.; Avugadda, S. K.; Fernández-Cabada, T.; Soni, N.; Cassani, M.; Mai, B. T.; Chantrell, R.; Pellegrino, T. Magnetic nanoparticles and clusters for magnetic hyperthermia: optimizing their heat performance and developing combinatorial therapies to tackle cancer. *Chem. Soc. Rev.* **2021**, *50*, 11614-11667.

(25) Dobson, J. Magnetic nanoparticles for drug delivery. *Drug Dev. Res.* **2006**, *67*, 55-60.

(26) Sun, C.; Lee, J. S. H.; Zhang, M. Magnetic nanoparticles in MR imaging and drug delivery. *Adv. Drug Delivery Rev.* **2008**, *60*, 1252-1265.

(27) Veiseh, O.; Gunn, J. W.; Zhang, M. Design and fabrication of magnetic nanoparticles for targeted drug delivery and imaging. *Adv. Drug Delivery Rev.* **2010**, *62*, 284-304.

(28) Linic, S.; Aslam, U.; Boerigter, C.; Morabito, M. Photochemical transformations on plasmonic metal nanoparticles. *Nat. Mater.* **2015**, *14*, 567-576.

(29) Liang, Z.; Sun, J.; Jiang, Y.; Jiang, L.; Chen, X. Plasmonic Enhanced Optoelectronic Devices. *Plasmonics* **2014**, *9*, 859-866.

(30) Link, S.; El-Sayed, M. A. Spectral Properties and Relaxation Dynamics of Surface Plasmon Electronic Oscillations in Gold and Silver Nanodots and Nanorods. *J. Phys. Chem. B* **1999**, *103*, 8410-8426.

(31) Jiang, N.; Zhuo, X.; Wang, J. Active Plasmonics: Principles, Structures, and Applications. *Chem. Rev.* **2018**, *118*, 3054-3099.

(32) Lim, D.-K.; Jeon, K.-S.; Kim, H. M.; Nam, J.-M.; Suh, Y. D. Nanogap-engineerable Raman-active nanodumbbells for single-molecule detection. *Nat. Mater.* **2010**, *9*, 60-67.

(33) Halas, N. J.; Lal, S.; Chang, W.-S.; Link, S.; Nordlander, P. Plasmons in Strongly Coupled Metallic Nanostructures. *Chem. Rev.* **2011**, *111*, 3913-3961.

(34) Jimenez de Aberasturi, D.; Serrano-Montes, A. B.; Langer, J.; Henriksen-Lacey, M.; Parak, W. J.; Liz-Marzán, L. M. Surface Enhanced Raman Scattering Encoded Gold Nanostars for Multiplexed Cell Discrimination. *Chem. Mater.* **2016**, *28*, 6779-6790.

(35) Reguera, J.; Langer, J.; Jiménez de Aberasturi, D.; Liz-Marzán, L. M. Anisotropic metal nanoparticles for surface enhanced Raman scattering. *Chem. Soc. Rev.* **2017**, *46*, 3866-3885.

(36) Anger, P.; Bharadwaj, P.; Novotny, L. Enhancement and Quenching of Single-Molecule Fluorescence. *Phys. Rev. Lett.* **2006**, *96*, 113002.

(37) Kinkhabwala, A.; Yu, Z.; Fan, S.; Avlasevich, Y.; Müllen, K.; Moerner, W. E. Large single-molecule fluorescence enhancements produced by a bowtie nanoantenna. *Nat. Photonics* **2009**, *3*, 654-657.

(38) Giannini, V.; Fernández-Domínguez, A. I.; Heck, S. C.; Maier, S. A. Plasmonic Nanoantennas: Fundamentals and Their Use in Controlling the Radiative Properties of Nanoemitters. *Chem. Rev.* **2011**, *111*, 3888-3912.

(39) Hyun, J. K.; Lauhon, L. J. Spatially Resolved Plasmonically Enhanced Photocurrent from Au Nanoparticles on a Si Nanowire. *Nano Lett.* **2011**, *11*, 2731-2734.

(40) Xiao, Y.; Yang, J. P.; Cheng, P. P.; Zhu, J. J.; Xu, Z. Q.; Deng, Y. H.; Lee, S. T.; Li, Y. Q.; Tang, J. X. Surface plasmon-enhanced electroluminescence in organic light-emitting diodes incorporating Au nanoparticles. *Appl. Phys. Lett.* **2012**, *100*, 013308.

(41) Arvizo, R. R.; Bhattacharyya, S.; Kudgus, R. A.; Giri, K.; Bhattacharya, R.; Mukherjee, P. Intrinsic therapeutic applications of noble metal nanoparticles: past, present and future. *Chem. Soc. Rev.* **2012**, *41*, 2943-2970.

(42) Brown, C. L.; Bushell, G.; Whitehouse, M. W.; Agrawal, D. S.; Tupe, S. G.; Paknikar, K. M.; Tiekink, E. R. T. Nanogoldpharmaceutics. *Gold Bulletin* **2007**, *40*, 245-250.

(43) Freestone, I.; Meeks, N.; Sax, M.; Higgitt, C. The Lycurgus Cup — A Roman nanotechnology. *Gold Bulletin* **2007**, *40*, 270-277.

(44) Faraday, M. X. The Bakerian Lecture. —Experimental relations of gold (and other metals) to light. *Philosophical Transactions of the Royal Society of London* **1857**, *147*, 145-181.

(45) Mie, G. Beiträge zur Optik trüber Medien, speziell kolloidaler Metallösungen. *Annalen der Physik* **1908**, *330*, 377-445.

(46) Turkevich, J.; Stevenson, P. C.; Hillier, J. A study of the nucleation and growth processes in the synthesis of colloidal gold. *Discussions of the Faraday Society* **1951**, *11*, 55-75.

(47) Frens, G. Controlled Nucleation for the Regulation of the Particle Size in Monodisperse Gold Suspensions. *Nature Physical Science* **1973**, *241*, 20-22.

(48) Giersig, M.; Mulvaney, P. Preparation of ordered colloid monolayers by electrophoretic deposition. *Langmuir* **1993**, *9*, 3408-3413.

(49) Brust, M.; Walker, M.; Bethell, D.; Schiffrin, D. J.; Whyman, R. Synthesis of thiol-derivatised gold nanoparticles in a two-phase Liquid–Liquid system. *J. Chem. Soc., Chem. Commun.* **1994**, 801-802.

(50) Brown, K. R.; Walter, D. G.; Natan, M. J. Seeding of Colloidal Au Nanoparticle Solutions. 2. Improved Control of Particle Size and Shape. *Chem. Mater.* **2000**, *12*, 306-313.

(51) Hiramatsu, H.; Osterloh, F. E. A Simple Large-Scale Synthesis of Nearly Monodisperse Gold and Silver Nanoparticles with Adjustable Sizes and with Exchangeable Surfactants. *Chem. Mater.* **2004**, *16*, 2509-2511.

(52) Perrault, S. D.; Chan, W. C. W. Synthesis and Surface Modification of Highly Monodispersed, Spherical Gold Nanoparticles of 50−200 nm. *J. Am. Chem. Soc.* **2009**, *131*, 17042-17043.

(53) Bastús, N. G.; Comenge, J.; Puntes, V. Kinetically Controlled Seeded Growth Synthesis of Citrate-Stabilized Gold Nanoparticles of up to 200 nm: Size Focusing versus Ostwald Ripening. *Langmuir* **2011**, *27*, 11098-11105.

(54) Martin, C. R. Template synthesis of polymeric and metal microtubules. *Adv. Mater.* **1991**, *3*, 457-459.

(55) Yu; Chang, S.-S.; Lee, C.-L.; Wang, C. R. C. Gold Nanorods: Electrochemical Synthesis and Optical Properties. *J. Phys. Chem. B* **1997**, *101*, 6661-6664.

(56) Chen, H.; Shao, L.; Li, Q.; Wang, J. Gold nanorods and their plasmonic properties. *Chem. Soc. Rev.* **2013**, *42*, 2679-2724.

(57) Jana, N. R.; Gearheart, L.; Murphy, C. J. Seed-Mediated Growth Approach for Shape-Controlled Synthesis of Spheroidal and Rod-like Gold Nanoparticles Using a Surfactant Template. *Adv. Mater.* **2001**, *13*, 1389-1393.

(58) Nikoobakht, B.; El-Sayed, M. A. Preparation and Growth Mechanism of Gold Nanorods (NRs) Using Seed-Mediated Growth Method. *Chem. Mater.* **2003**, *15*, 1957-1962.

(59) Liu, M.; Guyot-Sionnest, P. Mechanism of Silver(I)-Assisted Growth of Gold Nanorods and Bipyramids. *J. Phys. Chem. B* **2005**, *109*, 22192-22200.

(60) Gole, A.; Murphy, C. J. Seed-Mediated Synthesis of Gold Nanorods: Role of the Size and Nature of the Seed. *Chem. Mater.* **2004**, *16*, 3633-3640.

(61) Wu, H.-Y.; Chu, H.-C.; Kuo, T.-J.; Kuo, C.-L.; Huang, M. H. Seed-Mediated Synthesis of High Aspect Ratio Gold Nanorods with Nitric Acid. *Chem. Mater.* **2005**, *17*, 6447-6451.

(62) Chen, H. M.; Peng, H.-C.; Liu, R.-S.; Asakura, K.; Lee, C.-L.; Lee, J.-F.; Hu, S.-F. Controlling the Length and Shape of Gold Nanorods. *J. Phys. Chem. B* **2005**, *109*, 19553-19555.

(63) Kou, X.; Zhang, S.; Tsung, C.-K.; Yeung, M. H.; Shi, Q.; Stucky, G. D.; Sun, L.; Wang, J.; Yan, C. Growth of Gold Nanorods and Bipyramids Using CTEAB Surfactant. *J. Phys. Chem. B* **2006**, *110*, 16377-16383.

(64) Wang, S.; Xi, W.; Cai, F.; Zhao, X.; Xu, Z.; Qian, J.; He, S. Three-Photon Luminescence of Gold Nanorods and Its Applications for High Contrast Tissue and Deep In Vivo Brain Imaging. *Theranostics* **2015**, *5*, 251-266.

(65) Kozek, K. A.; Kozek, K. M.; Wu, W.-C.; Mishra, S. R.; Tracy, J. B. Large-Scale Synthesis of Gold Nanorods through Continuous Secondary Growth. *Chem. Mater.* **2013**, *25*, 4537-4544.

(66) Gole, A.; Orendorff, C. J.; Murphy, C. J. Immobilization of Gold Nanorods onto Acid-Terminated Self-Assembled Monolayers via Electrostatic Interactions. *Langmuir* **2004**, *20*, 7117-7122.

(67) Chen, W.; McCarthy, T. J. Layer-by-Layer Deposition: A Tool for Polymer Surface Modification. *Macromolecules* **1997**, *30*, 78-86.

(68) Chirea, M.; Borges, J.; Pereira, C. M.; Silva, A. F. Density-Dependent Electrochemical Properties of Vertically Aligned Gold Nanorods. *J. Phys. Chem. C* **2010**, *114*, 9478-9488.

(69) Ming, T.; Kou, X.; Chen, H.; Wang, T.; Tam, H.-L.; Cheah, K.-W.; Chen, J.-Y.; Wang, J. Ordered Gold Nanostructure Assemblies Formed By Droplet Evaporation. *Angewandte Chemie International Edition* **2008**, *47*, 9685-9690.

(70) Wei, W.; Wang, Y.; Ji, J.; Zuo, S.; Li, W.; Bai, F.; Fan, H. Fabrication of Large-Area Arrays of Vertically Aligned Gold Nanorods. *Nano Lett.* **2018**, *18*, 4467-4472.

(71) van der Zande, B. M. I.; Pagès, L.; Hikmet, R. A. M.; van Blaaderen, A. Optical Properties of Aligned Rod-Shaped Gold Particles Dispersed in Poly(vinyl alcohol) Films. *J. Phys. Chem. B* **1999**, *103*, 5761-5767.

(72) Pérez-Juste, J.; Rodríguez-González, B.; Mulvaney, P.; Liz-Marzán, L. M. Optical Control and Patterning of Gold-Nanorod–Poly(vinyl alcohol) Nanocomposite Films. *Adv. Funct. Mater.* **2005**, *15*, 1065-1071.

(73) Murphy, C. J.; Orendorff, C. J. Alignment of Gold Nanorods in Polymer Composites and on Polymer Surfaces. *Adv. Mater.* **2005**, *17*, 2173-2177.

(74) Umadevi, S.; Feng, X.; Hegmann, T. Large Area Self-Assembly of Nematic Liquid-Crystal-Functionalized Gold Nanorods. *Adv. Funct. Mater.* **2013**, *23*, 1393-1403.

(75) Liu, Q.; Campbell, M. G.; Evans, J. S.; Smalyukh, I. I. Orientationally Ordered Colloidal Co-Dispersions of Gold Nanorods and Cellulose Nanocrystals. *Adv. Mater.* **2014**, *26*, 7178-7184.

(76) Zhang, Y.; Liu, Q.; Mundoor, H.; Yuan, Y.; Smalyukh, I. I. Metal Nanoparticle Dispersion, Alignment, and Assembly in Nematic Liquid Crystals for Applications in Switchable Plasmonic Color Filters and E-Polarizers. *ACS Nano* **2015**, *9*, 3097-3108.

(77) van der Zande, B. M. I.; Koper, G. J. M.; Lekkerkerker, H. N. W. Alignment of Rod-Shaped Gold Particles by Electric Fields. *J. Phys. Chem. B* **1999**, *103*, 5754-5760.

(78) Ahmed, W.; Kooij, E. S.; van Silfhout, A.; Poelsema, B. Quantitative Analysis of Gold Nanorod Alignment after Electric Field-Assisted Deposition. *Nano Lett.* **2009**, *9*, 3786-3794.

(79) Fontana, J.; da Costa, G. K. B.; Pereira, J. M.; Naciri, J.; Ratna, B. R.; Palffy-Muhoray, P.; Carvalho, I. C. S. Electric field induced orientational order of gold nanorods in dilute organic suspensions. *Appl. Phys. Lett.* **2016**, *108*, 081904.

(80) Greybush, N. J.; Charipar, K.; Geldmeier, J. A.; Bauman, S. J.; Johns, P.; Naciri, J.; Charipar, N.; Park, K.; Vaia, R. A.; Fontana, J. Dynamic Plasmonic Pixels. *ACS Nano* **2019**, *13*, 3875-3883.

(81) Wang, M.; Gao, C.; He, L.; Lu, Q.; Zhang, J.; Tang, C.; Zorba, S.; Yin, Y. Magnetic Tuning of Plasmonic Excitation of Gold Nanorods. *J. Am. Chem. Soc.* **2013**, *135*, 15302-15305.

(82) Li, Z.; Jin, J.; Yang, F.; Song, N.; Yin, Y. Coupling magnetic and plasmonic anisotropy in hybrid nanorods for mechanochromic responses. *Nat. Commun.* **2020**, *11*, 2883.

(83) Lu, A.-H.; Salabas, E. L.; Schüth, F. Magnetic Nanoparticles: Synthesis, Protection, Functionalization, and Application. *Angewandte Chemie International Edition* **2007**, *46*, 1222-1244.

(84) Ling, D.; Lee, N.; Hyeon, T. Chemical Synthesis and Assembly of Uniformly Sized Iron Oxide Nanoparticles for Medical Applications. *Acc. Chem. Res.* **2015**, *48*, 1276-1285.

(85) Kim, D.; Lee, N.; Park, M.; Kim, B. H.; An, K.; Hyeon, T. Synthesis of Uniform Ferrimagnetic Magnetite Nanocubes. *J. Am. Chem. Soc.* **2009**, *131*, 454-455.

(86) Kim, B. H.; Lee, N.; Kim, H.; An, K.; Park, Y. I.; Choi, Y.; Shin, K.; Lee, Y.; Kwon, S. G.; Na, H. B.; Park, J.-G.; Ahn, T.-Y.; Kim, Y.-W.; Moon, W. K.; Choi, S. H.; Hyeon, T. Large-Scale Synthesis of Uniform and Extremely Small-Sized Iron Oxide Nanoparticles for High-Resolution T1 Magnetic Resonance Imaging Contrast Agents. *J. Am. Chem. Soc.* **2011**, *133*, 12624-12631.

(87) Frey, N. A.; Peng, S.; Cheng, K.; Sun, S. Magnetic nanoparticles: synthesis, functionalization, and applications in bioimaging and magnetic energy storage. *Chem. Soc. Rev.* **2009**, *38*, 2532-2542.

(88) Sun, S.; Zeng, H. Size-Controlled Synthesis of Magnetite Nanoparticles. *J. Am. Chem. Soc.* **2002**, *124*, 8204-8205.

(89) Sun, S.; Zeng, H.; Robinson, D. B.; Raoux, S.; Rice, P. M.; Wang, S. X.; Li, G. Monodisperse MFe2O4 (M = Fe, Co, Mn) Nanoparticles. *J. Am. Chem. Soc.* **2004**, *126*, 273-279.

(90) Xu, Z.; Shen, C.; Hou, Y.; Gao, H.; Sun, S. Oleylamine as Both Reducing Agent and Stabilizer in a Facile Synthesis of Magnetite Nanoparticles. *Chem. Mater.* **2009**, *21*, 1778-1780.

(91) Jana, N. R.; Chen, Y.; Peng, X. Size- and Shape-Controlled Magnetic (Cr, Mn, Fe, Co, Ni) Oxide Nanocrystals via a Simple and General Approach. *Chem. Mater.* **2004**, *16*, 3931-3935.

(92) Park, J.; An, K.; Hwang, Y.; Park, J.-G.; Noh, H.-J.; Kim, J.-Y.; Park, J.-H.; Hwang, N.-M.; Hyeon, T. Ultra-large-scale syntheses of monodisperse nanocrystals. *Nat. Mater.* **2004**, *3*, 891-895.

(93) Chen, R.; Christiansen, M. G.; Sourakov, A.; Mohr, A.; Matsumoto, Y.; Okada, S.; Jasanoff, A.; Anikeeva, P. High-Performance Ferrite Nanoparticles through Nonaqueous Redox Phase Tuning. *Nano Lett.* **2016**, *16*, 1345-1351.

(94) Ha, M.; Kim, J.-H.; You, M.; Li, Q.; Fan, C.; Nam, J.-M. Multicomponent Plasmonic Nanoparticles: From Heterostructured Nanoparticles to Colloidal Composite Nanostructures. *Chem. Rev.* **2019**, *119*, 12208-12278.

(95) Höller, R. P. M.; Kuttner, C.; Mayer, M.; Wang, R.; Dulle, M.; Contreras-Cáceres, R.; Fery, A.; Liz-Marzán, L. M. Colloidal Superstructures with Triangular Cores: Size Effects on SERS Efficiency. *ACS Photonics* **2020**, *7*, 1839-1848.

(96) Rossner, C.; König, T. A. F.; Fery, A. Plasmonic Properties of Colloidal Assemblies. *Advanced Optical Materials* **2021**, *9*, 2001869.

(97) Nepal, D.; Drummy, L. F.; Biswas, S.; Park, K.; Vaia, R. A. Large Scale Solution Assembly of Quantum Dot–Gold Nanorod Architectures with Plasmon Enhanced Fluorescence. *ACS Nano* **2013**, *7*, 9064-9074.

(98) Huang, L.; Ao, L.; Hu, D.; Wang, W.; Sheng, Z.; Su, W. Magneto-Plasmonic Nanocapsules for Multimodal-Imaging and Magnetically Guided Combination Cancer Therapy. *Chem. Mater.* **2016**, *28*, 5896-5904.

(99) Lee, S.; Sim, K.; Moon, S. Y.; Choi, J.; Jeon, Y.; Nam, J.-M.; Park, S.-J. Controlled Assembly of Plasmonic Nanoparticles: From Static to Dynamic Nanostructures. *Adv. Mater.* **2021**, *33*, 2007668.

(100) Sastry, M.; Rao, M.; Ganesh, K. N. Electrostatic Assembly of Nanoparticles and Biomacromolecules. *Acc. Chem. Res.* **2002**, *35*, 847-855.

(101) Bian, T.; Gardin, A.; Gemen, J.; Houben, L.; Perego, C.; Lee, B.; Elad, N.; Chu, Z.; Pavan, G. M.; Klajn, R. Electrostatic co-assembly of nanoparticles with oppositely charged small molecules into static and dynamic superstructures. *Nature Chemistry* **2021**, *13*, 940-949.

(102) Xiao, Q.; Zheng, X.; Bu, W.; Ge, W.; Zhang, S.; Chen, F.; Xing, H.; Ren, Q.; Fan, W.; Zhao, K.; Hua, Y.; Shi, J. A Core/Satellite Multifunctional Nanotheranostic for in Vivo Imaging and Tumor Eradication by Radiation/Photothermal Synergistic Therapy. *J. Am. Chem. Soc.* **2013**, *135*, 13041-13048.

(103) De Silva Indrasekara, A. S.; Norton, S. J.; Geitner, N. K.; Crawford, B. M.; Wiesner, M. R.; Vo-Dinh, T. Tailoring the Core–Satellite Nanoassembly Architectures by Tuning Internanoparticle Electrostatic Interactions. *Langmuir* **2018**, *34*, 14617-14623.

(104) Kuttner, C.; Höller, R. P. M.; Quintanilla, M.; Schnepf, M. J.; Dulle, M.; Fery, A.; Liz-Marzán, L. M. SERS and plasmonic heating efficiency from anisotropic core/satellite superstructures. *Nanoscale* **2019**, *11*, 17655-17663.

CHAPTER 2. Functionalization of Nanoparticles

In most instances, as-synthesized nanoparticles (NPs) are not useful for applications without further functionalization for integration with other materials.[1] While there are several challenges in tailoring the surface properties of NPs, chemists have developed a well-established set of techniques for surface functionalization. Many strategies have been developed for functionalizing NPs with different moieties, such as hydrocarbon molecules of different lengths, dendrimers, surfactants, polymers and biomolecules, which are discussed in more detail in a review article by Mout *et al*.[2] Chapters 3 and 4 present results for the electrostatic core/satellite assembly of anionic gold nanorods (GNRs) coated with bovine serum albumin (BSA) and cationic Fe_3O_4 NPs coated with polyethyleneimine (PEI). This chapter is focused on introducing protein and polymer functionalization of NPs.

2.1 Nanoparticle Surface and Ligand Chemistry

The high surface-area-to-volume ratio of nanomaterials makes their surfaces the key aspect that determines many of their physicochemical properties and processing. The ligands used for synthesizing NPs have a critical role in determining the size, shape, stability and crystallinity of NPs.[3] In many instances, the native ligands need to be exchanged with other coatings to bring desired functionalities, such as hydrophobicity/hydrophilicity, steric size, biocombability, biofunctionalization, or enhanced catalytic activity.[4] Ligand exchange depends on chemical interactions and coordination of ligands on the surface of a NP. NP surfaces are often not uniform and have crystallographic facets with distinct physical and chemical properties.[3,5] Ligands can be classified in three categories, X-, L-, and Z-type, based on how they interact with facets on the surface of inorganic NPs (Figures 2.1,2.2).[4,5]

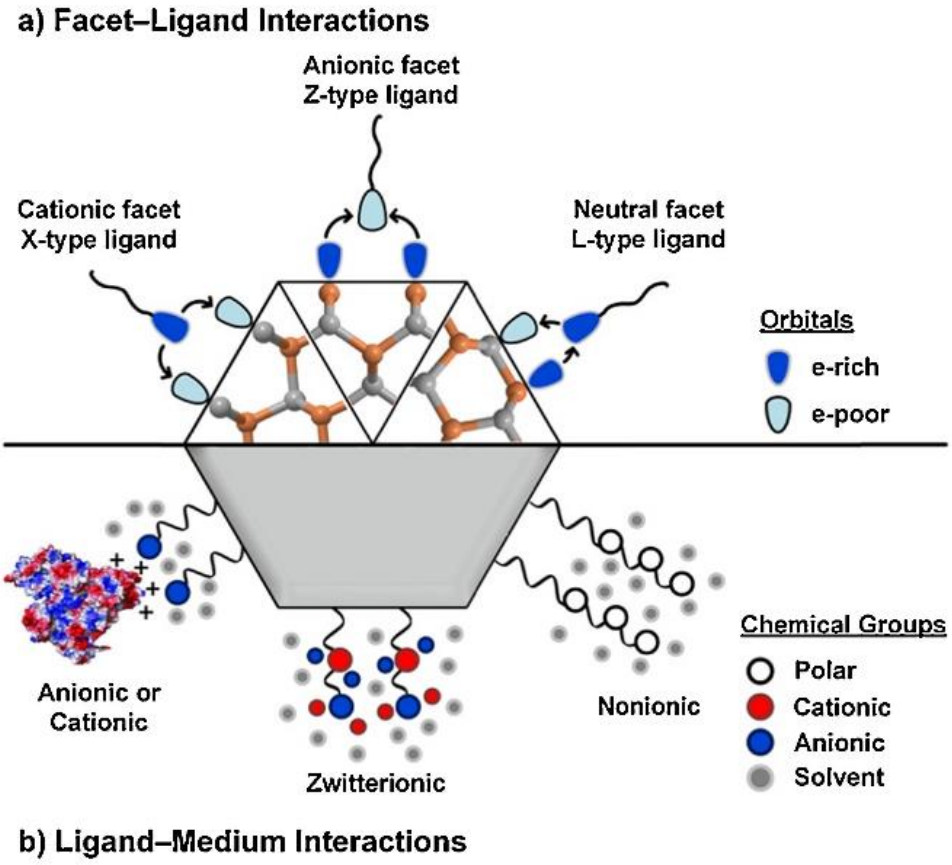

Figure 2.1. Interactions between ligands and the surface of NPs: (a) coordination of ligands with crystal facets and (b) interactions of ligands with the surrounding medium.[5]

Anionic X-type ligands bind with cationic facets and donate valance electrons to the metal-ligand bond and include carboxylates (R-COO−), phosphonates (R-P(OH)OO−), and thiolates (R-S−). R denotes an alkyl chain (Figure 2.2). Neutral L-type ligands form dative bonds with neutral facets and donate a lone pair of electrons to the bond. L-type ligands have lone pairs of electrons or delocalized π-electrons, for example amines (RNH_2), phosphines (R_3P), and phosphine oxides (R_3PO), including PEI and oleylamine. Z-type ligands withdraw two electrons and bind with anionic facets.[3-5] Because of different binding mechanisms and interactions, it is preferred to have ligand exchange between ligands of the same type, for example to prevent a change in the net charge on a NP during ligand exchange.[5,6]

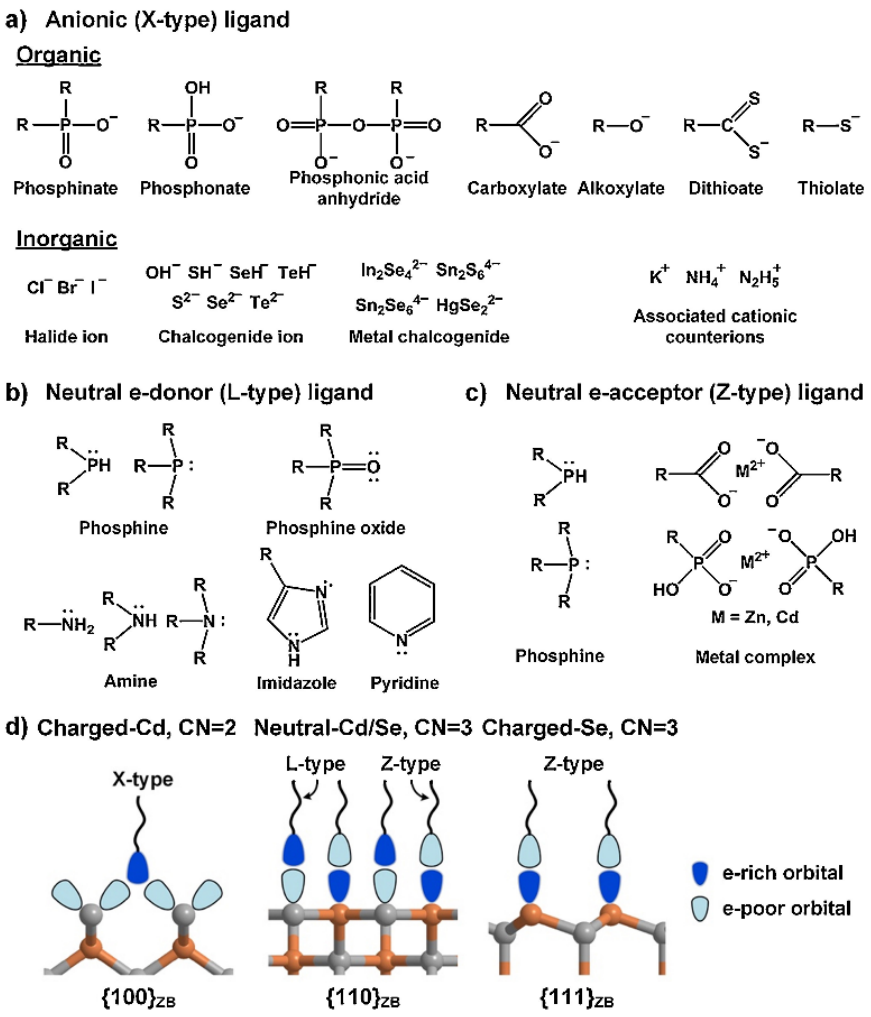

Figure 2.2. Classification of ligands (a) anionic X-type ligands, (b) neutral L-type ligands, (c) neutral Z-type ligands. (d) Examples of attachment of ligands on different crystal facets of a CdSe quantum dot.[5]

2.2 Ligand Stripping

Ligand exchange reactions are performed in two different ways: (i) exchange between native and replacement ligand and (ii) stripping away the native ligand followed by regrafting with the replacement ligand. The second method is often preferred when ligand exchange is not energetically favorable, for example when changing between X- and L- type ligands.[7] In this dissertation research, oleic acid-stabilized Fe_3O_4 NPs were synthesized and further functionalized

with PEI, discussed in Chapters 3,4. While oleic acid (X-type ligand) is useful for the initial synthesis of the NPs, a multistep process is needed for functionalization with PEI. The oleic acid is first stripped away followed by regrafting with oleylamine (L-type ligand), which is then exchanged with PEI (L-type ligand). In the following paragraph, stripping oleic acid from Fe_3O_4 NPs is discussed.

A common approach for removing oleic acid employs absorbates that displace oleic acid and strongly bind to the surface of NP but offer little or no opportunity for re-grafting.[8,9] Reimhult and coworkers demonstrated a technique, in which a nucleophilic anion (F^-) can completely strip away oleic acid from Fe_3O_4 NPs.[10] In this host-guest coordination technique, crown ether strongly coordinates with Na^+ from metal halides such as NaF, leaving naked F^- anions, which are efficient for replacing deprotonated oleate (Figure 2.3). After stripping away the oleic acid, dispersing the NPs in a protic solvent such as water drives desorption of F^-, which allows for regrafting with organic ligands.

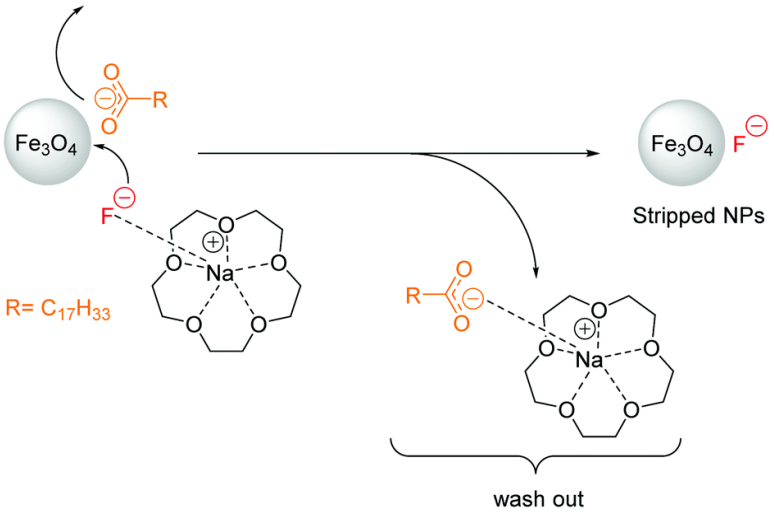

Figure 2.3. Schematic for stripping of carboxylic acid (oleic acid) from Fe_3O_4 NPs using crown ether (15-crown-5) and NaF.[10]

2.3. PEI-Functionalized NPs

PEI is a cationic polymer, also referred to as a polycation, which has a high density of positive charge in its branched structure. Branched PEI primary, secondary, and tertiary amines (Figure 2.4). PEI is available with a wide range of molecular weights, branching, and is biocompatible.[11] PEI has been intensively investigated for gene transfection and drug delivery, because it can bind to biomolecules, such as proteins and DNA, by electrostatic interactions.[11-15]

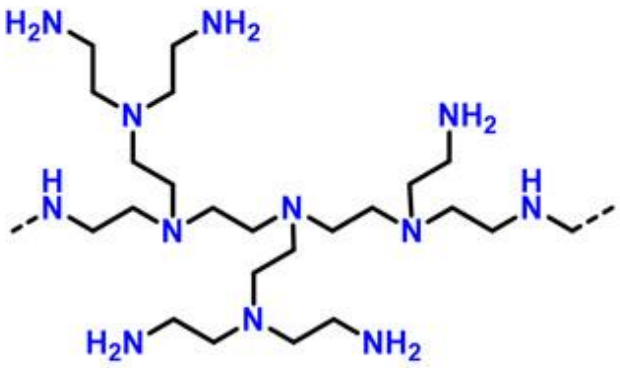

Figure 2.4. Example of the branched structure of PEI.[16]

PEI-functionalized Fe_3O_4 NPs are an excellent candidate for targeted gene delivery applications,[15] but the synthesis of PEI-functionalized Fe_3O_4 NPs remains challenging. Cai *et al*. reported a hydrothermal, one-pot synthesis of PEI-coated Fe_3O_4 NPs for biomedical applications. In that work, $FeCl_2 \cdot 4H_2O$ is reduced by NH_4OH in the presence of PEI in an autoclave at 130 °C to obtain PEI-Fe_3O_4 NPs.[12] The average size of the NPs could be tailored in a range of 11-22 nm by adjusting the concentrations of $FeCl_2$, PEI, and NH_4OH. The size control and uniformity reported in this method is not comparable, however, with the excellent monodispersity achieved through thermal decomposition of organometallic salts in the presence of organic ligands, as discussed in Chapter 1. A recent study reports trisodium citrate-assisted solvothermal synthesis of Fe_3O_4 NPs in aqueous media followed by mixing with PEI at 60 °C overnight for

functionalizing the NPs with PEI.[17] This process also suffers from polydispersity and limited shape control.[17]

In this dissertation, we developed a technique for functionalizing monodisperse oleic acid-stabilized Fe_3O_4 NPs with PEI. The detailed experimental technique is discussed in Chapters 3,4. PEI is a L-type ligand and cannot be directly exchanged with X-type oleic acid bound to Fe_3O_4 NPs. Instead, oleic acid is first stripped away and then regrafted with oleylamine (L-type ligand) before functionalization with PEI. Oleylamine-stabilized Fe_3O_4 NPs are then mixed with excess PEI in chloroform at 40 °C to perform ligand exchange. The PEI-functionalized Fe_3O_4 NPs are hydrophilic and transferred into water. Water is added to the NPs in chloroform and mixed by shaking, which brings hydrophilic PEI-Fe_3O_4 NPs into water (Figure 2.5a). The same mixing process with PEI in chloroform does not work for oleic acid-stabilized Fe_3O_4 NPs, which remain in chloroform (Figure 2.5b).

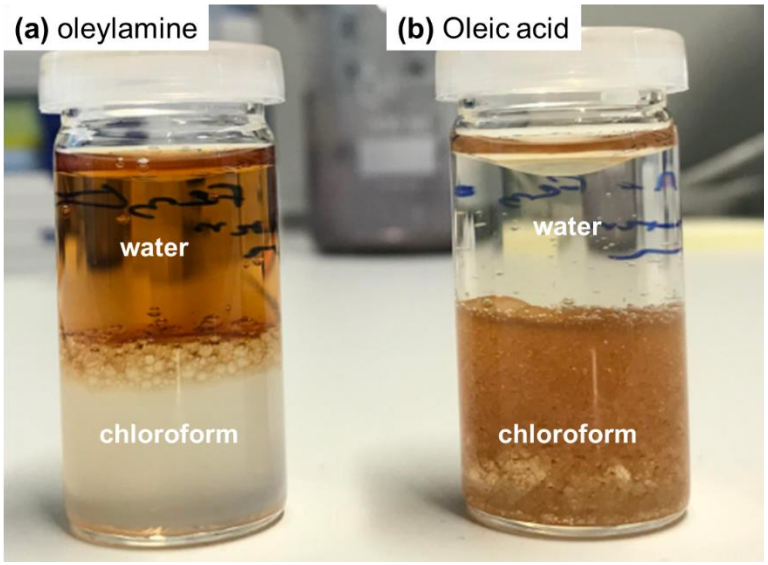

Figure 2.5. PEI functionalization and phase transfer of (a) oleylamine- and (b) oleic acid-stabilized Fe_3O_4 NPs.

PEI functionalization increases the hydrodynamic radius of NPs, which can be measured with dynamic light scattering (DLS). The molecular weight (MW) of PEI also determines the hydrodynamic size of the functionalized NPs. From DLS measurements, a significant increase in hydrodynamic size is observed after functionalization with 25 kDa PEI compared to 10 kDa. The significant increase in size is attributed to agglomeration by bridging multiple NPs with high-MW (25 kDa) PEI. TEM images of PEI-Fe_3O_4 NPs for 10 kDa and 25 kDa PEI show evidence of agglomeration with larger MW (Figure 2.6).

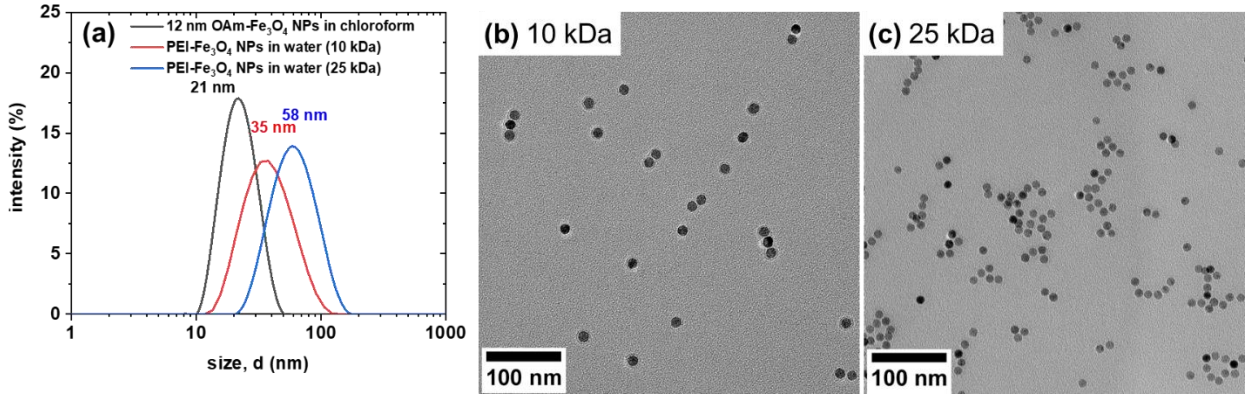

Figure 2.6. (a) Dynamic light scattering (DLS) measurements of oleylamine-stabilized 12 nm Fe_3O_4 NPs and TEM after functionalization with (b) 10 kDa and (c) 25 kDa PEI.

2.4. BSA Coating of Gold Nanorods

Cetyltrimethylammonium bromide (CTAB) is crucial for precise shape control in the synthesis of gold nanorods (GNRs). The tunable longitudinal surface plasmon resonance (LSPR) of GNRs in the near-infrared spectrum is useful for biomedical applications because there is deeper penetration of near-infrared light through tissue than visible light. CTAB, however, exhibits cytotoxicity above a concentration of 1 μM, which restricts biomedical applications with the native CTAB coatings.[18,19] Moreover, an excess of CTAB is required to impart colloidal stability to GNRs.[20] In this context, functionalizing GNRs with proteins can confer both biocompatibility and stability.[19] Since proteins containing a variety of functional groups, including thiols, amines and

carboxylates, they have strong affinity for binding to metal surfaces like Au.[21] Proteins are high-MW polymers with high charge density and provide both steric and electrostatic stabilization of NPs. Furthermore, proteins have protic functional groups that exhibit pH-dependent behaviors. Therefore, it is possible to tune the electrostatic properties of protein-coated NPs by adjusting the pH, which was useful for establishing the assembly technique reported in Chapters 3,4.[21-23]

Tebbe *et al*. reported complete replacement of CTAB with BSA for GNRs with different aspect ratios without affecting colloidal dispersion (Figure 2.7).[19] During ligand exchange, the concentration CTAB is kept low (~0.1 mM), which is around 10× below the critical micelle concentration. At this concentration, the CTAB bilayer stabilizing GNRs is disrupted, and the GNRs will agglomerate if no BSA is added. Addition of highly concentrated BSA (10 mg/mL) ensures binding with GNRs through the disrupted CTAB layer. The mixture of GNRs with low CTAB and high BSA concentrations is sonicated for 30 minutes for the ligand exchange at neutral pH (~7). The mixture is then centrifuged and the supernatant containing CTAB is discarded, followed by adding a solution containing ~1 mg/mL BSA (pH ~12). After allowing this second round of ligand exchange to proceed for at least 24 hours, the replacement of CTAB with BSA is complete. The experimental procedure are results are presented in Chapters 3,4.

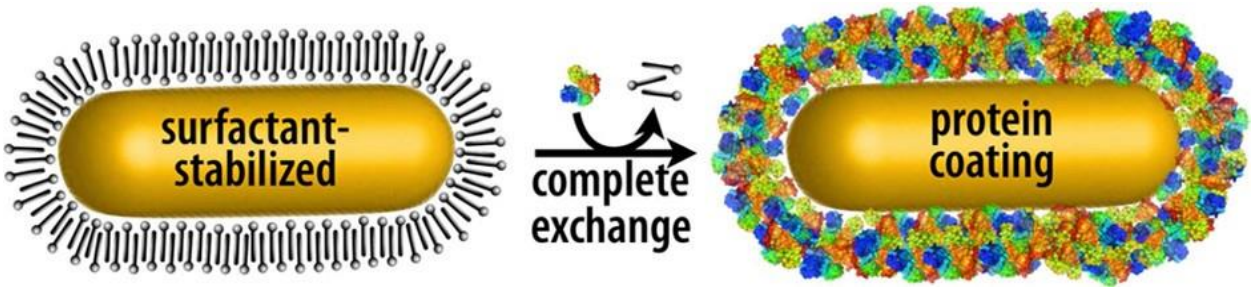

Figure 2.7. Schematic of BSA overcoating of GNRs by ligand exchange between the surfactant (CTAB) and protein (BSA)[19]

2.5. References

(1) Vigderman, L.; Khanal, B. P.; Zubarev, E. R. Functional Gold Nanorods: Synthesis, Self-Assembly, and Sensing Applications. *Adv. Mater.* **2012**, *24*, 4811-4841.

(2) Mout, R.; Moyano, D. F.; Rana, S.; Rotello, V. M. Surface functionalization of nanoparticles for nanomedicine. *Chem. Soc. Rev.* **2012**, *41*, 2539-2544.

(3) Boles, M. A.; Ling, D.; Hyeon, T.; Talapin, D. V. The surface science of nanocrystals. *Nat. Mater.* **2016**, *15*, 141-153.

(4) Heuer-Jungemann, A.; Feliu, N.; Bakaimi, I.; Hamaly, M.; Alkilany, A.; Chakraborty, I.; Masood, A.; Casula, M. F.; Kostopoulou, A.; Oh, E.; Susumu, K.; Stewart, M. H.; Medintz, I. L.; Stratakis, E.; Parak, W. J.; Kanaras, A. G. The Role of Ligands in the Chemical Synthesis and Applications of Inorganic Nanoparticles. *Chem. Rev.* **2019**, *119*, 4819-4880.

(5) Lim, S. J.; Ma, L.; Schleife, A.; Smith, A. M. Quantum dot surface engineering: Toward inert fluorophores with compact size and bright, stable emission. *Coord. Chem. Rev.* **2016**, *320-321*, 216-237.

(6) Anderson, N. C.; Hendricks, M. P.; Choi, J. J.; Owen, J. S. Ligand Exchange and the Stoichiometry of Metal Chalcogenide Nanocrystals: Spectroscopic Observation of Facile Metal-Carboxylate Displacement and Binding. *J. Am. Chem. Soc.* **2013**, *135*, 18536-18548.

(7) Ung, D.; Murphy, I. A.; Cossairt, B. M. Designing nanoparticle interfaces for inner-sphere catalysis. *Dalton Trans.* **2020**, *49*, 4995-5005.

(8) Kovalenko, M. V.; Scheele, M.; Talapin, D. V. Colloidal Nanocrystals with Molecular Metal Chalcogenide Surface Ligands. *Science* **2009**, *324*, 1417-1420.

(9) Korpany, K. V.; Mottillo, C.; Bachelder, J.; Cross, S. N.; Dong, P.; Trudel, S.; Friščić, T.; Blum, A. S. One-step ligand exchange and switching from hydrophobic to water-stable hydrophilic superparamagnetic iron oxide nanoparticles by mechanochemical milling. *Chem. Commun.* **2016**, *52*, 3054-3057.

(10) Shirmardi Shaghasemi, B.; Dehghani, E. S.; Benetti, E. M.; Reimhult, E. Host–guest driven ligand replacement on monodisperse inorganic nanoparticles. *Nanoscale* **2017**, *9*, 8925-8929.

(11) Chen, Z.; Lv, Z.; Sun, Y.; Chi, Z.; Qing, G. Recent advancements in polyethyleneimine-based materials and their biomedical, biotechnology, and biomaterial applications. *Journal of Materials Chemistry B* **2020**, *8*, 2951-2973.

(12) Li, C.; Zhong, D.; Zhang, Y.; Tuo, W.; Li, N.; Wang, Q.; Liu, Z.; Xue, W. The effect of the gene carrier material polyethyleneimine on the structure and function of human red blood cells in vitro. *Journal of Materials Chemistry B* **2013**, *1*, 1885-1893.

(13) Zhong, D.; Jiao, Y.; Zhang, Y.; Zhang, W.; Li, N.; Zuo, Q.; Wang, Q.; Xue, W.; Liu, Z. Effects of the gene carrier polyethyleneimines on structure and function of blood components. *Biomaterials* **2013**, *34*, 294-305.

(14) Didenko, V. V.; Ngo, H.; Baskin, D. S. Polyethyleneimine as a transmembrane carrier of fluorescently labeled proteins and antibodies. *Anal. Biochem.* **2005**, *344*, 168-173.

(15) McBain, S. C.; Yiu, H. H. P.; El Haj, A.; Dobson, J. Polyethyleneimine functionalized iron oxide nanoparticles as agents for DNA delivery and transfection. *J. Mater. Chem.* **2007**, *17*, 2561-2565.

(16) Jain, M.; Seth, J. R.; Hegde, L. R.; Sharma, K. P. Unprecedented Self-Assembly in Dilute Aqueous Solution of Polyethyleneimine: Formation of Fibrillar Network. *Macromolecules* **2020**, *53*, 8974-8981.

(17) Liu, W.; Pei, W.; Moradi, M.; Zhao, D.; Li, Z.; Zhang, M.; Xu, D.; Wang, F. Polyethyleneimine Functionalized Mesoporous Magnetic Nanoparticles with Enhanced Antibacterial and Antibiofilm Activity in an Alternating Magnetic Field. *ACS Appl. Mater. Interfaces* **2022**, *14*, 18794-18805.

(18) Ray, P. C.; Yu, H.; Fu, P. P. Toxicity and Environmental Risks of Nanomaterials: Challenges and Future Needs. *Journal of Environmental Science and Health, Part C* **2009**, *27*, 1-35.

(19) Tebbe, M.; Kuttner, C.; Männel, M.; Fery, A.; Chanana, M. Colloidally Stable and Surfactant-Free Protein-Coated Gold Nanorods in Biological Media. *ACS Appl. Mater. Interfaces* **2015**, *7*, 5984-5991.

(20) Iqbal, M.; Tae, G. Unstable Reshaping of Gold Nanorods Prepared by a Wet Chemical Method in the Presence of Silver Nitrate. *J. Nanosci. Nanotechnol.* **2006**, *6*, 3355-3359.

(21) Chanana, M.; Correa-Duarte, M. A.; Liz-Marzán, L. M. Insulin-Coated Gold Nanoparticles: A Plasmonic Device for Studying Metal–Protein Interactions. *Small* **2011**, *7*, 2650-2660.

(22) Strozyk, M. S.; Chanana, M.; Pastoriza-Santos, I.; Pérez-Juste, J.; Liz-Marzán, L. M. Protein/Polymer-Based Dual-Responsive Gold Nanoparticles with pH-Dependent Thermal Sensitivity. *Adv. Funct. Mater.* **2012**, *22*, 1436-1444.

(23) Chanana, M.; Rivera_Gil, P.; Correa-Duarte, M. A.; Liz-Marzán, L. M.; Parak, W. J. Physicochemical Properties of Protein-Coated Gold Nanoparticles in Biological Fluids

and Cells before and after Proteolytic Digestion. *Angewandte Chemie International Edition* **2013**, *52*, 4179-4183.

CHAPTER 3. Electrostatic Self-Assembly of Magnetic and Plasmonic Nanoparticles on Gold Nanorods

The following Manuscript "Electrostatic Self-Assembly of Magnetic and Plasmonic Nanoparticles on Gold Nanorods" by Mehedi H. Rizvi, Ruosong Wang, Jonas Schubert, Christian Rossner, Andreas Fery and Joseph B. Tracy is under preparation. The manuscript reports electrostatic self-assembly of core/satellite nanostructures.

Electrostatic Self-Assembly of Magnetic and Plasmonic Nanoparticles on Gold Nanorods

Mehedi H. Rizvi,[1] *Ruosong Wang,*[2] *Jonas Schubert,* [2] *Christian Rossner,* [2,3] *Andreas Fery,* [2,4] *Joseph B. Tracy**[1]

[1]*Department of Materials Science and Engineering, North Carolina State University, Raleigh, North Carolina 27695, United States*

[2]*Leibniz-Institut für Polymerforschung Dresden e.V., Institute for Physical Chemistry and Polymer Physics, 01069 Dresden, Germany*

[3]*Dresden Center for Intelligent Materials (DCIM), Technische Universität Dresden, 01069 Dresden, Germany*

[4]*Chair for Physical Chemistry of Polymeric Materials, Technische Universität Dresden, 01062 Dresden, Germany*

Corresponding E-mail: jbtracy@ncsu.edu

Keywords: Core/satellite assembly, plasmon shift, gold nanorods, iron oxide nanoparticles, multilayer nanoparticle composite

Abstract

Overcoating gold nanorods (GNRs) with plasmonic or magnetic satellite nanoparticles (NPs) can modify the longitudinal and transverse surface plasmon resonances (LSPR and TSPR) through coupling with the satellite NPs. We report use of electrostatic interactions to reversibly assemble different types and amounts of satellite NPs on GNR cores, which allows coupling with and manipulation of the LSPR and TSPR of the GNR core. Cationic Fe_3O_4 NPs and spherical gold NPs (GNPs) functionalized with polyethylenimine (PEI) assemble on the surface of anionic GNRs functionalized with bovine serum albumin (BSA). The distinct extinction spectra of Fe_3O_4 NPs and GNRs make possible quantification of the loading of satellite NPs from optical extinction spectra. pH is a useful lever for controlling assembly and disassembly processes because the electrostatic properties of PEI- and BSA-functionalized NPs strongly depend on pH. Stable assemblies are obtained at pH between the isoelectric points (pH_I) of BSA (pH_I ~5) and PEI (pH_I ~11), because the core and satellite NPs have opposite charges within this window. At lower or higher pH, the core and satellite NPs have like charges, which inhibits assembly. Moreover, disassembly is possible by adjusting the pH to values outside of this range.

3.1. Introduction

There has been longstanding interest in multifunctional or hybrid nanoparticles (NPs), but challenges in synthesizing them have impeded progress from fundamental studies to widespread applications.[1-4] Multifunctionality includes combining multiple, independent functions within a single structure or having coupled properties, from which new behaviors can emerge. Core/satellite NPs (CSNPs) with several satellite NPs surrounding a single core NP, which is often larger than the satellites, is a common configuration. There are several physical and chemical methods for synthesizing or assembling CSNPs, which also have different extents of reversibility. As an

example of a multifunctional CSNP, combining superparamagnetic iron oxide NPs and plasmonic NPs yields magnetically responsive plasmonic NPs that have potential applications in drug delivery and theranostics, combining multimodal imaging and photothermal therapy.[5-11] As an example of coupled properties, integration of plasmonic NPs can yield plasmon-plasmon coupling, which alters photon absorption and has emerging applications in biosensing, photovoltaics and lasing.

Common strategies for preparing CSNPs include seeded growth of satellite NPs,[5,12,13] heteroaggregation,[14] chemisorption,[15] and use of DNA,[16-20] peptides,[21,22] proteins,[23] or other crosslinking molecules.[24-30] In seeded growth, heterogenous nucleation and growth of satellite NPs on a core NP is sensitive to the composition and crystal structure of the core.[5,31,32] Seeded growth can be challenging, because many methods for synthesizing NPs have been optimized for homogeneous nucleation and growth.[33,34] Use of crosslinker molecules is subject to constraints imposed by surface chemistry on the core and satellite NPs and can require fine optimization of several parameters, including properties of the solvent, to inhibit undesired aggregation.[25] Electrostatic assembly of oppositely charged core and satellite NPs is another approach that has been investigated extensively.[35-45] Electrostatic assembly is scalable and does not require maintaining strict reaction conditions. Here, we report the electrostatic assembly of well dispersed CSNPs by mixing cationic satellite NPs functionalized with PEI and anionic GNRs coated with bovine serum albumin (BSA). The positive ζ-potential of the CSNP products keeps them well dispersed in water.

The use of external triggers to alter the chemical properties and interactions of NPs allows dynamic tuning of their multifunctional properties. Dynamic assembly has been reported for single-component NPs triggered by light,[46] temperature,[47] solvent polarity,[48] and pH.[49] Reversible

assembly of multicomponent CSNPs remains challenging, however. Reversible assembly of CSNPs has been reported using light and temperature,[50,51] but to the best of our knowledge, pH control of multicomponent CSNPs has not been reported. Furthermore, tuning pH allows control over the loading of satellite NPs.

3.2. Results and Discussion

Tunable self-assembly of two different types of satellite NPs, Fe_3O_4 NPs and plasmonic GNPs, with GNR cores in water was investigated. The CSNP products with Fe_3O_4 NPs and GNPs are referred to as MagGNRs and AuGNRs respectively. pH during the assembly process was adjusted to achieve CSNPs with different relative amounts of satellite NPs. Adjusting the pH above or below certain limits drives dissociation of the CSNPs.

Satellite NPs, 13.4 nm Fe_3O_4 NPs and 8 nm GNPs, were synthesized by thermal decomposition of metal salts in the presence of oleic acid and oleylamine, respectively. Ligand exchange was performed to prepare PEI-functionalized NPs (Supporting Information, Figure 3.6). The nature of the initial ligand present during NP synthesis is important for determining ligand exchange kinetics. Classification of different types of ligands is helpful for planning ligand exchange reactions. Both oleylamine and PEI containing $-NH_2$ headgroups are L-type (neutral electron donor) ligands, which makes exchange between them favorable and fast.[52,53] Oleic acid is an X-type (anionic) ligand, which is difficult to exchange with cationic PEI. Therefore, functionalization of Fe_3O_4 NPs with PEI required stripping away oleic acid and regrafting with oleylamine. Crown ethers coordinate with metal ions and form complexes upon mixing with NaF, generating highly active F^- anion, which is efficient in displacing oleic acid from the surface of Fe_3O_4 NPs.[54] Functionalization with a cationic polyelectrolyte like PEI imparts positive ζ-potential and good dispersion in water spanning low pH to mildly basic water. We call the product of

functionalizing Fe_3O_4 NPs with PEI, PEI-Fe_3O_4 NPs. A seed-mediated technique was employed to prepare CTAB-stabilized GNRs. The positively charged CTAB bilayer was completely replaced with the anionic protein, BSA. Different functional groups, such thiols, amines, and carboxylates present in the protein combined with use of a CTAB concentration below the critical micelle concentration drive overcoating GNRs with BSA, which we call BSA-GNRs.[55] Unless otherwise mentioned, BSA-GNRs of core size of 76 nm × 26 nm were used to synthesize MagGNRs (Supporting Information, Figure 3.7).

Upon mixing of core and satellite NPs, the electrostatic attractive interaction between negatively charged BSA-GNRs and positively charged PEI-Fe_3O_4 NPs drives self-assembly to MagGNRs. Excess PEI-Fe_3O_4 NPs were then separated by centrifugation several times, discarding the supernatant and dispersing the pellet in deionized water. Excess PEI-Fe_3O_4 NPs are required to achieve fully overcoated MagGNRs with minimal bridging or agglomeration (Supporting Information, Figure 3.8). The extinction spectra of purified MagGNRs are similar to BSA-GNRs with two distinctions (Figure 3.1a). MagGNRs show a red shift in the longitudinal surface plasmon resonance (LSPR), which is attributed to the increased dielectric constant of the GNR surface. The presence of Fe_3O_4 NPs also contributes prominently to the spectra of MagGNRs in the blue, which is most prominent below 600 nm. The loading of PEI-Fe_3O_4 NPs in the MagGNRs depends on the pH during the assembly. With increasing loading of PEI-Fe_3O_4 NPs, the LSPR of MagGNRs is red shifted, which is expected when the material coating the GNRs has an increased dielectric constant (Figure 3.1a,b). Previous studies have shown that a dense or porous dielectric shell around GNRs has little effect on absorbance cross-section of GNRs except the redshift.[56]

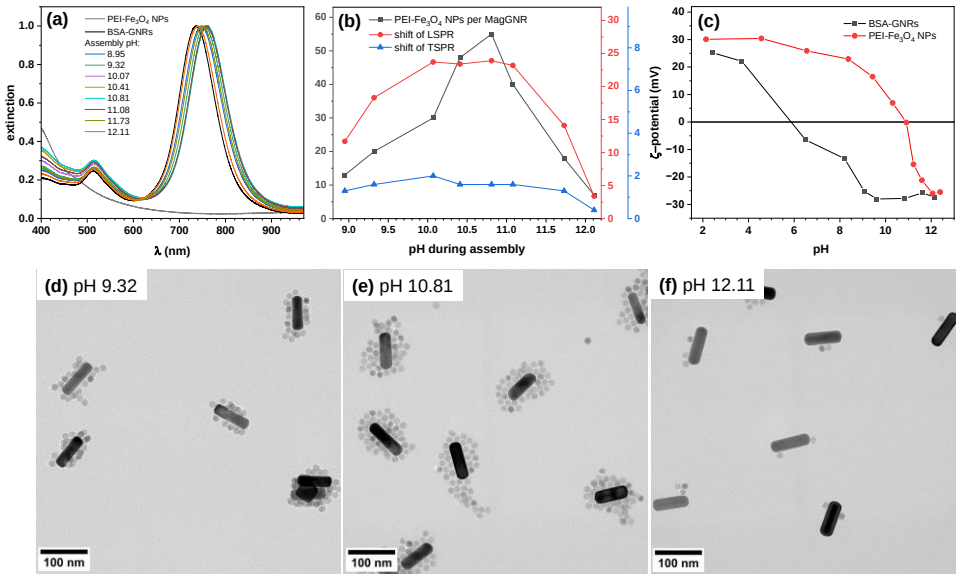

Figure 3.1. pH-dependent assembly of MagGNRs: (a) Extinction spectra of PEI-Fe_3O_4 NPs, BSA-GNRs and purified MagGNRs. (b) Number of PEI-Fe_3O_4 NPs attached to each BSA-GNR and shift of LSPR and TSPR in MagGNRs. (c) ζ-potential of PEI-Fe_3O_4 NPs and BSA-GNRs as a function of pH. (d-f) TEM images of MagGNRs assembled at pH of 9.32, 10.81, and 12.11.

The distinct extinction spectra of Fe_3O_4 NPs and the LSPR of GNRs are the basis for developing a technique to estimate the loading of Fe_3O_4 NPs in MagGNRs at different pH (Figure 1b). We can assume that the extinction spectrum of MagGNRs is a linear combination of the spectra for BSA-GNRs and PEI-Fe_3O_4 NPs, $A_{CSNPs}(\lambda) = \alpha A_{BSA-GNRs}(\lambda) + \beta A_{PEI-Fe3O4}(\lambda)$, where A, λ, α, and β are the extinction, wavelength, and the relative contribution of BSA-GNRs and PEI-Fe_3O_4 NPs in the spectra of MagGNRs, respectively. With α and β from the above equation and extinction coefficients for BSA-GNRs and PEI-Fe_3O_4 NPs, one can estimate the relative amounts of the constituent NPs in MagGNRs (Supporting Information, Figure 3.9).

The loading of PEI-Fe_3O_4 NPs increases with increasing pH up to 10.81 and then drops, which could be explained by the pH-dependence of the ζ-potential of the reactant NPs (Figure 1b and c). The isoelectric point (pH_I) of BSA is 4.7,[57,58] which agrees with our measurements of ζ-

potential of BSA-GNRs at different pH. As the pH increases, the negative ζ-potential of the deprotonated BSA-GNRs reaches a constant value of ~-26 mV and remains unchanged with further increase of pH. Conversely, the positive ζ-potential of protonated PEI-Fe_3O_4 NPs decreases with increasing pH up to the pH_I of ~10.9. In the pH range of 8-11, the core and satellite NPs undergo spontaneous self-assembly upon mixing because they are oppositely charged. The increased loading of PEI-Fe_3O_4 NPs in the MagGNRs with increasing pH is due to the decreasing surface charge of PEI-Fe_3O_4 NPs, which we explain as follows. More PEI-Fe_3O_4 NPs are required to neutralize the negative charge of the core BSA-GNRs as the ζ-potential of PEI-Fe_3O_4 NPs decreases. Reduced repulsion between the satellite NPs also allows higher loading as the ζ-potential of PEI-Fe_3O_4 NPs decreases. Therefore, the maximum loading is achieved near the pH_I of PEI-Fe_3O_4 NPs, where they still have small, positive surface charge. The shift of LSPR saturates before the loading of PEI-Fe_3O_4 NPs is maximized. A maximum red shift of ~24 nm was observed when BSA-GNRs were entirely covered with a single layer of PEI-Fe_3O_4 NPs. No significant shift in the transverse surface plasmon resonance (TSPR) was observed for MagGNRs.

Further increasing the pH for assembly decreases the loading of PEI-Fe_3O_4 NPs when the PEI-Fe_3O_4 NPs become negatively charged. At pH ~12, PEI-Fe_3O_4 NPs become nearly completely deprotonated with high negative charge and minimal assembly. TEM images of MagGNRs reaffirm that the satellite PEI-Fe_3O_4 NPs loading increases with pH and then decreases (Figure 1d-f). At pH 9.32, the CSNPs are not fully covered with a layer of PEI-Fe_3O_4 NPs, whereas at pH 10.81, the coating consists of a multilayer of PEI-Fe_3O_4 NPs. Assembly at pH of 12.11 gives minimal loading of satellite PEI-Fe_3O_4 NPs.

MagGNRs are stable in deionized water for at least several months, where both core and satellite NPs are oppositely charged. However, dissociation of CSNPs can be triggered by

increasing (decreasing) the pH of the environment above 12 (below 3), where both core and satellite NPs are fully deprotonated (protonated) with high positive (negative) surface charge. Repulsive core-satellite and satellite-satellite interactions drive quick dissociation of the MagGNRs into BSA-GNRs and PEI-Fe_3O_4 NPs (Figure 3.2). 1 M NaOH (1 M HCl) was added in the MagGNRs dispersion with a micropipette to increase (lower) the pH to 12.4 (2.1), which drives immediate dissociation. The extinction spectra show a corresponding blue shift (Figure 3.2a,b). The dissociated product was purified by centrifugation and then discarding the supernatant and redispersing in deionized water. Extinction spectra of the purified dissociated samples closely resemble BSA-GNRs with a slight shift in the LSPR corresponding to small portion of undissociated PEI-Fe_3O_4 NPs. TEM images of the purified samples also confirm nearly complete dissociation of the MagGNRs (Figure 3.2c,d).

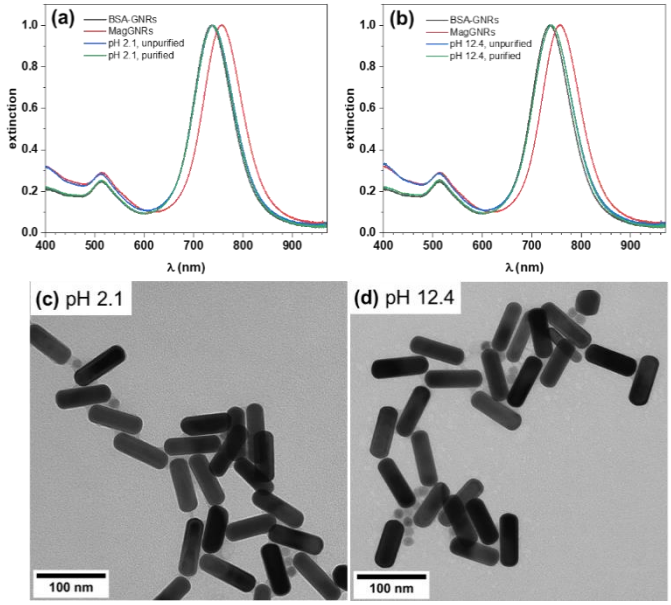

Figure 3.2. pH-triggered disassembly of MagGNRs: (a,b) extinction spectra of BSA-GNRs and MagGNRs before adjusting the pH to 2.1 or 12.4, and disassembled MagGNRs after adjusting the pH, with spectra acquired before and after purification. (c,d) TEM images of MagGNRs disassembled at pH of 2.1 and 12.4 and purified.

MagGNRs with larger cores can align in magnetic fields, resulting in anisotropic optical properties in magnetic fields and when illuminated with polarized light. The extinction of large MagGNRs strongly depends on the angle between the magnetic field and light polarization directions.[59] The anisotropic polarized extinction results in dichroism between crossed polarizers. MagGNRs were prepared with BSA-GNR core dimensions of 153 nm × 46 nm (Supporting Information, Figure 3.7). The MagGNR solution in a cuvette is placed between crossed polarizers within the gap of an electromagnet, depicted in schematically in Figure 3.3a. The magnetic field is in the plane of polarizers and at an angle of 45° with respect to the polarization direction of each polarizer. Light from an array of small LEDs first passes through a polarizer, then the cuvette, followed by the second, crossed polarizer, then enters the camera. When the electromagnet remains turned off, the MagGNRs are randomly oriented, and the cross-polarizer blocks most of the light coming from LED panel to the camera (Figure 3.3b). Switching the electromagnet on orients the MagGNRs at 45° with respect to both polarization direction, which allows a portion of the light to pass through the cuvette to the camera, and thus the LED panel appears bright (Figure 3.3c). Upon adding a drop of 1 M HCl while keeping the electromagnet on (Figure 3.3d), the color begins to fade, because the acid drives dissociation of the MagGNRs, making them unable to align with the magnetic field and eliminating their dichroic effect. Driving mixing with the pipette completes

dissociation, and the brightness of the LED completely disappears (Figure 3.3e). Switching off the electromagnet has no further effect on the dissociated MagGNRs (Figure 3.3f).

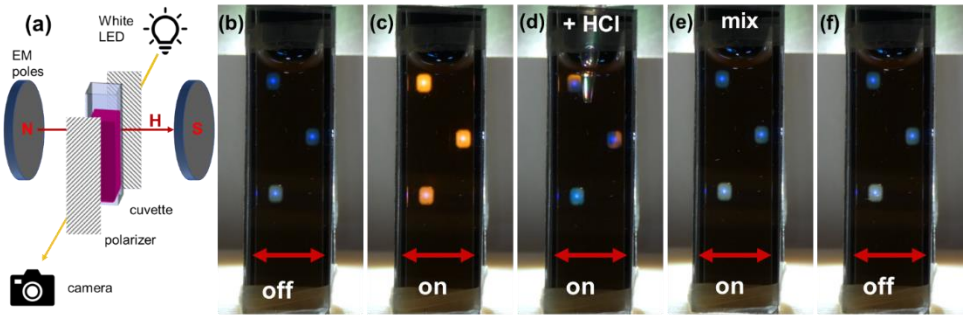

Figure 3.3. (a) Schematic of the setup for dichroism experiments. (b-f) Photographs of a cuvette with 1-cm path length containing a solution of large MagGNRs placed between crossed polarizers and in the gap of the electromagnet: (b) magnetic field off, (c) field (2 kOe) on, (d) field on immediately after adding a drop of 1 M HCl to drive dissociation of the MagGNRs, (e) after mixing, and (f) after turning the field off.

As a test of the generality of electrostatic assembly of PEI-functionalized satellite NPs on BSA-GNRs, PEI-GNPs were assembled with BSA-GNRs, yielding AuGNRs. In both MagGNRs and AuGNRs, the pH determines the ζ-potential, loading of satellite NPs, and can control disassembly (Figure 3.4). The loading of PEI-GNPs in AuGNRs initially increases with pH and then gradually decreases (Figure 3.4a). The maximum loading of PEI-GNPs is obtained at pH 10.78, which is close to the pH_I of PEI-GNPs (Figure 3.4b). TEM images of the AuGNRs confirm pH-dependent loading of PEI-GNPs, in agreement with the extinction spectra (Figure 4c-g). Near-field coupling of the core-to-satellite and satellite-to-satellite NPs yields a red-shift in LSPR and TSPR of AuGNRs.[23] Unlike MagGNRs, in AuGNRs, the extent of coupling and magnitude of the red shift do not saturate as the loading of PEI-GNPs increases (Figure 3.4a,b). For AuGNRs, the redshift of the LSPR is well replicated in the TSPR for all loadings of PEI-GNPs, which is a different behavior than MagGNRs. These distinct behaviors for the redshifts in MagGNRs and

AuGNRs are not surprising given the different underlying mechanisms. The disassembly behavior of AuGNRs is similar to that of the MagGNRs (Supporting Information, Figure 3.10). At pH 2.12 and 12.38, the AuGNRs are nearly completely dissociated.

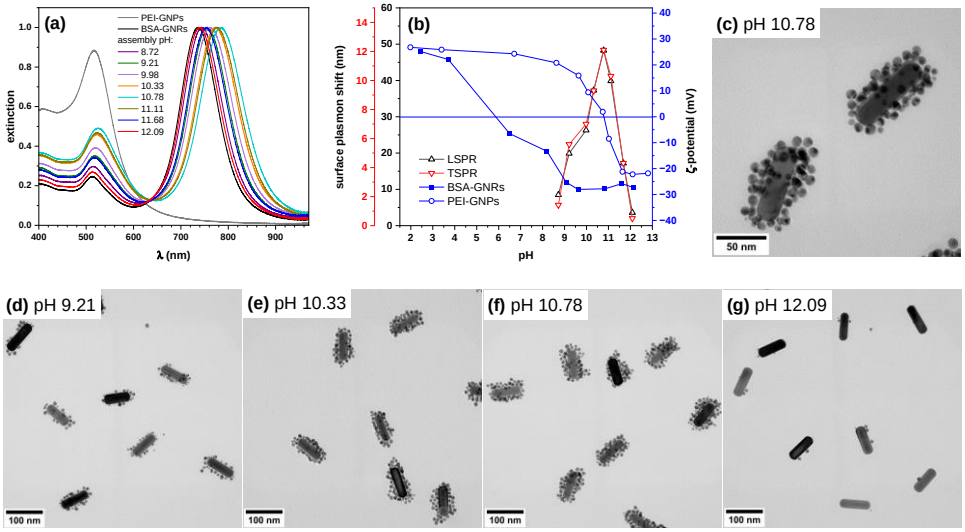

Figure 3.4. pH-dependent assembly of AuGNRs: (a) Extinction spectra of PEI-GNPs, BSA-GNRs and purified AuGNRs. (b) Red shift of LSPR and TSPR maximum overlapped with ζ-potential of BSA-GNRs and PEI-GNPs at different pH. (c) Magnified TEM image of AuGNRs assembled at pH 10.78. (d-g) TEM images of AuGNRs assembled at pH 9.21, 10.33, 10.78, and 12.09.

Combining multiple types of satellite NPs in CSNPs can further expand or tailor the multifunctional properties of CSNPs. As an example of such assembly, BSA-GNRs are sequentially coated with PEI-GNPs and then PEI-Fe_3O_4 NPs. AuGNRs were mixed with PEI-Fe_3O_4 NPs, and the pH was adjusted to 10.98 to deposit an additional layer of PEI-Fe_3O_4 NPs on the AuGNRs. The composite Fe_3O_4-AuGNRs were then centrifuged to remove excess PEI-Fe_3O_4 NPs and redispersed in deionized water. The extinction spectrum of Fe_3O_4-AuGNRs shows a shoulder in the blue from the loading of PEI-Fe_3O_4 NPs (Figure 3.5a). The PEI-Fe_3O_4 NPs cause a 10 nm redshift in the LSPR in addition to the 48 nm redshift from the PEI-GNP coating. We attribute this additional 10 nm red shift to the altered dielectric environment surrounding the

AuGNRs. The TSPR also exhibits an additional 4 nm redshift due to the additional layer of PEI-Fe_3O_4 NPs. TEM images confirm that PEI-GNPs remain bound to BSA-GNRs after sequential loading of PEI-Fe_3O_4 NPs, and the satellite NPs do not mix within the coating (Figure 3.5b,c)

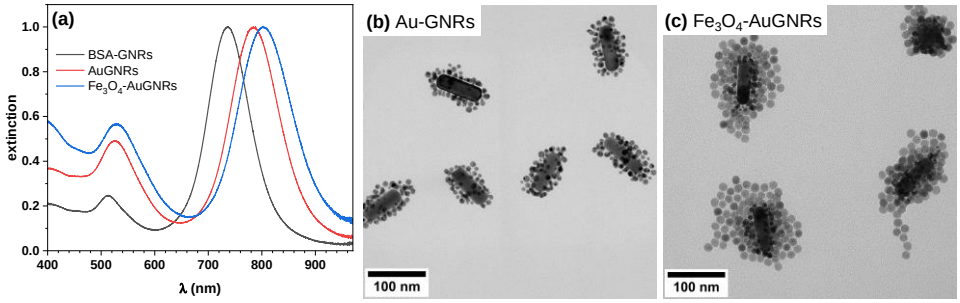

Figure 3.5. (a) Extinction spectra of BSA-GNRs, AuGNRs, and Fe_3O_4-AuGNRs. (b) TEM image of AuGNRs before adding PEI-Fe_3O_4 NPs. (c) TEM image of composite Fe_3O_4-AuGNRs with an inner layer of GNPs and an outer layer of PEI-Fe_3O_4 NPs.

3.3. Conclusions

BSA-functionalized anionic core and PEI-functionalized cationic satellite NPs allow controlled assembly and disassembly of CSNPs. The resulting positive surface charge imparts good colloidal stability to the CSNPs. The electrostatic assembly technique developed in this work allows tuning the structure and composition of CSNPs to modulate their multifunctionality. This highly general approach could be applied for developing many types of CSNPs with novel, multifunctional properties. Furthermore, pH-controlled assembly and disassembly could be applied in colorimetric pH sensing applications.

3.4. Experimental Section

Chemicals. Cetyltrimethylammonium bromide (CTAB, Amresco, high purity), $HAuCl_4 \cdot xH_2O$ (Alfa Aesar, 99.999%, where x was estimated as 3), KBr (Alfa Aesar, ACS, 99% min), $AgNO_3$ (Alfa Aesar, 99.9995%), deionized water (Ricca, ACS Reagent grade, ASTM Type I, ASTM Type II), ascorbic acid (AA, J.T. Baker, 99.5%), hydroquinone (Acros Organics, 99.5%),

$NaBH_4$ (Sigma-Aldrich, 99%, 213462), NaOH (Sigma-Aldrich, 98%), BSA (Sigma-Aldrich, A7906, 98%), Na-citrate dihydrate (Mallinckrodt, 99% min), $FeCl_3$ (Alfa Aesar, anhydrous, 98%), Fe(III) acetylacetonate (Strem, 99%), Na oleate (TCI America, 97% min), oleic acid (Sigma-Aldrich, 90%), 1-octadecene (Sigma-Aldrich, 90%), benzyl ether (Acros Organics, 99%), oleylamine (Sigma Aldrich), hexanes (Macron, 95%), ethanol (Koptec, absolute, anhydrous), isopropanol (Macron, 99.5%), chloroform (OmniSolv, 99.9%), 15-crown-5 ether (Ambeed, 98%), NaF (Alfa Aesar, 99.99%), and PEI (Alfa Aesar, branched, MW 10000, 99%) were used as received.

Synthesis of CTAB-Stabilized GNRs. CTAB-GNRs with LSPR of 736 nm and dimensions of 74 nm × 26 nm were synthesized in a three-step growth process. In the first step, 19 mg of CTAB-GNRs were synthesized with a LSPR of 760 nm by prolonging the duration of injection of ascorbic acid during secondary growth to 260 min.[60] 20 mL of the CTAB-GNRs were then mixed with 10 mL of tertiary growth solution containing 91 mM CTAB, 0.93 mM $HAuCl_4$, 9.1 mM KBr, and 0.992 mM ascorbic acid and aged for 2 hours to achieve the final dimensions and LSPR wavelength. The GNR solution has CTAB concentration of 91 mM and required purification by centrifugation to achieve a CTAB concentration of ~1 mM and final volume of 10 mL for further BSA-overcoating.[59] Larger BSA-GNRs with dimensions of 153 nm × 46 nm were prepared following a recently published overgrowth procedure.[59]

BSA Overcoating of GNRs. 20 mg of BSA was dissolved in 20 mL of deionized water containing 0.02 wt% Na citrate under sonication. 10 mL of deionized water was added to the previously prepared 10 mL solution of CTAB-GNRs with its CTAB concentration of ~1mM, and this 20-mL GNR solution was quickly added to the 20-mL BSA solution under sonication. The mixture was sonicated for 30 minutes, and ice was added to the sonication bath intermittently to

avoid heating above 35 °C. The GNR solution was then centrifuged (Thermo Scientific Sorvall Legend X1R with Fiberlite F15-6x100y rotor) at 9000 rpm (8875 *g*) for 20 min to remove most of the supernatant. The GNR pellet was then redispersed in 20 mL of 0.1 mg/mL BSA solution with pH adjusted to ~10 and aged overnight. This solution was purified four times to separate excess BSA from the BSA-GNRs. In each of the purification steps, 20 mL of the solution was centrifuged at 9000 rpm (8875 *g*) for 20 min, then most of the supernatant was discarded using a micropipette, and the pellet was redispersed in 20 mL of water that had been adjusted to pH ~10. After the fourth round of purification, the BSA-GNRs were redispersed in 20 mL of pH-adjusted water and stored in a refrigerator for future use in assembly.

Synthesis of Fe_3O_4 NPs and Functionalization with PEI. Oleic acid-stabilized 13.4 nm Fe_3O_4 NPs were synthesized by thermal decomposition of iron salt in organic solvents with high boiling points.[61,62] The precursor iron oleate was prepared by dissolving 18.27 g of Na oleate and 3.244 g of anhydrous $FeCl_3$ in a solvent mixture of 40 mL of ethanol, 70 mL of hexanes and 30 mL water. The mixture was kept refluxing at 70 °C for 4 hours with magnetic stirring to complete the reaction. The organic layer containing iron oleate was then washed three times with water to remove unreacted sodium oleate and then dried in a fume hood for two days to remove hexanes. For synthesizing Fe_3O_4 NPs, 2.5 g of this Fe oleate and 1.26 g of oleic acid were dissolved in 5.55 mL of 1-octadecene and 2.77 mL of benzyl ether in a round-bottomed flask connected to a Schlenk line. The mixture of reactants was degassed under vacuum at 60 °C for 30 min, followed by heating to 325 °C for 30 min under N_2 blanket at a rate of 3.3 °C/min. After cooling to room temperature, 2 mL of the reaction product was added to premixed hexanes (2 mL) and ethanol (6 mL) and centrifuged to isolate the NPs, followed by redispersion in 20 mL hexanes.

The oleic acid ligands on Fe_3O_4 NPs were stripped away and regrafted with oleylamine to facilitate PEI functionalization. 14 mL of isopropyl alcohol was added to the 20 mL of Fe_3O_4 NPs in hexanes, followed by adding a solution containing 2 mL of water, 100 mg of NaF, and 0.45 mL of 15-crown-5 ether. The mixture was sonicated for 5 min and aged for two hours to complete ligand stripping. The ligand-stripped NPs were successively washed with hexanes, isopropanol, water, and then ethanol. Washing was performed twice in each solvent, where the NPs were sonicated for 10 minutes, centrifuged at 5000-8000 rpm (2739-7012 *g*), and then redispersed in the next solvent after discarding the supernatant. After the final washing step with ethanol, 9.98 mL of chloroform was added to the sedimented Fe_3O_4 NPs, followed by adding 20 μL of oleylamine. The NPs are quickly regrafted with oleylamine, which turns the turbid suspension into a brown-red transparent solution of dispersed NPs. This stock solution has a concentration of 1.48 mg/mL of Fe_3O_4 based on measurements by inductively coupled optical emission spectroscopy (ICP-OES).

100 mg of PEI was dissolved in 30 mL of chloroform for functionalizing the Fe_3O_4 NPs. 9 mL of chloroform was added to 1 mL of oleylamine-stabilized Fe_3O_4 NP stock solution followed by mixing with the 30 mL PEI solution under vigorous stirring. The mixture was then sonicated for two hours followed by stirring for 2 hours at 40 °C. After cooling to room temperature, 5 mL of deionized water was added, followed by shaking by hand for 2 min. PEI-functionalized Fe_3O_4 NPs separate into the aqueous phase. The aqueous Fe_3O_4 NPs were then extracted and washed 5 times to remove excess PEI. In each washing cycle, centrifugation was performed with a centrifuge membrane filter (Amicon Ultra, 100 kDa) at 3500 rpm (1342 *g*) for 30 min. Excess PEI molecules pass through the filter, while the PEI-Fe_3O_4 NPs are collected on the filter. For the next washing

cycle, 5 mL of water was first added to redisperse the PEI-Fe_3O_4 NPs. Finally, the purified NPs were redispersed in 2.5 mL of deionized water.

Synthesis and PEI Functionalization of GNPs. Oleylamine-stabilized GNPs with an average diameter of 8 nm were synthesized by a hot-injection method.[63] 4 mL of oleylamine was degassed at room temperature for 30 min and then heated to 150 °C under nitrogen. 2 mL of oleylamine containing 150 mg of $HAuCl_4 \cdot xH_2O$ was injected into the hot stirring oleylamine solvent and allowed to react for 7 min. Followed by rapid cooling to room temperature, 5 mL of hexanes and then 15 mL of ethanol was added to flocculate the GNPs, which were isolated by centrifugation at 1000 rpm. After discarding the supernatant, the product was redispersed in 5 mL of chloroform.

PEI functionalization was performed in a similar fashion to Fe_3O_4 NPs. 0.2 mL of the GNP stock solution was diluted in 10 mL of chloroform and added to 30 mL of chloroform containing 25 mg of PEI under vigorous stirring followed by sonication for 30 min and stirring for 2 hours at 40 °C. The PEI-GNRs were then purified with centrifuge membrane filters and redispersed in 2 mL of deionized water.

Assembly and Disassembly of CSNPs. A series of BSA-GNRs dispersed in water with different basicity were prepared by taking 0.5 mL of the purified BSA-GNRs, centrifuging (Eppendorf 5415C) them at 5000 rpm (2152 *g*) for 10 min and replacing the supernatant with 0.5 mL of basic water containing 0.01-20 mM of NaOH. Each sample in the series of BSA-GNR solutions was then mixed with 0.5 mL of PEI-Fe_3O_4 NPs or PEI-GNPs in deionized water, and the and pH was registered after mixing but before purification. After stirring each mixture of core and satellite NPs for 2 hours, 4 cycles of centrifugation at 5000 rpm (2152 *g*) for 10 min were performed to separate CSNPs from excess PEI-Fe_3O_4 or PEI-GNPs satellite NPs. After the final

purification cycle, the product was dispersed in 1 mL of deionized water for further characterization.

Quantification of Loading of Satellite NPs. Values of α and β were chosen to achieve maximum overlap between αBSA-GNRs + βPEI-Fe_3O_4 and MagGNRs. The concentrations of core and satellite NPs can be calculated from α, β, and the extinction coefficients of BSA-GNRs and PEI-Fe_3O_4 NPs, from which the ratio *R* can be calculated, the average number of satellite PEI-Fe_3O_4 NPs in a MagGNR. The concentration of PEI-Fe_3O_4 NPs is calculated to be 0.98 mg/mL based on ICP-OES measurement, and the solution has an extinction of 20 (calculated from quantitative dilution) at 400 nm. Assuming the diameter of spherical Fe_3O_4 NPs is 13.4 nm and using the bulk density of 5.17 g/cm^3, the concentration of NPs corresponding to each extinction value can be estimated. Similarly, for GNRs, the extinction of 1.2 at 400 nm corresponds to a concentration of 0.0985 mg/mL, which is 0.50 mM of Au atoms.[64]

Assembly of Fe_3O_4-AuGNRs. For preparing multilayer Fe_3O_4-AuGNRs, 0.5 mL of purified AuGNRs dispersed in deionized water was added to a stirring solution of 0.5 mL PEI-Fe_3O_4 NPs. A few μL of 0.05 M NaOH was added to the stirring mixture incrementally, until a pH of 11 was achieved. The solution was kept stirring for two hours. The excess PEI-Fe_3O_4 NPs were removed by centrifugation at 3500 rpm (1342 *g*) for 20 minutes for four times, followed by discarding the supernatant and redispersing the sedimented Fe_3O_4-AuGNRs in deionized water after each cycle of centrifugation.

Characterization. Transmission electron microscopy (TEM) was performed using a FEI Talos F200X G2 at an operating voltage of 200 kV. Samples were prepared by drop casting followed by drying onto a carbon-coated Cu TEM grid. Optical extinction spectroscopy was performed using an Ocean Optics Red Tide USB650 spectrometer with a glass cuvette having a 1

cm path length. For the experiment showing dichroism, large MagGNRs were prepared by mixing 0.75 mL of PEI-Fe_3O_4 NPs dispersed in deionized water with 0.75 mL of BSA-GNRs dispersed in basic water. The mixture was kept stirring for 30 min, and a pH of 10.6 was recorded. The solution was then transferred into a cuvette and diluted with 1.5 mL of deionized water. The cuvette was sandwiched between crossed polarizers and placed between the poles of an electromagnet (GMW 3472-70 electromagnet) as shown in Figure 3.3.

3.5. References

(1) Zeng, H.; Sun, S. Syntheses, Properties, and Potential Applications of Multicomponent Magnetic Nanoparticles. *Adv. Funct. Mater.* **2008**, *18*, 391-400.

(2) Guo, J.; Tardy, B. L.; Christofferson, A. J.; Dai, Y.; Richardson, J. J.; Zhu, W.; Hu, M.; Ju, Y.; Cui, J.; Dagastine, R. R.; Yarovsky, I.; Caruso, F. Modular assembly of superstructures from polyphenol-functionalized building blocks. *Nat. Nanotechnol.* **2016**, *11*, 1105-1111.

(3) Jin, R.; Liu, Z.; Bai, Y.; Zhou, Y.; Gooding, J. J.; Chen, X. Core–Satellite Mesoporous Silica–Gold Nanotheranostics for Biological Stimuli Triggered Multimodal Cancer Therapy. *Adv. Funct. Mater.* **2018**, *28*, 1801961.

(4) Rossner, C.; Fery, A. Planet–satellite nanostructures from inorganic nanoparticles: from synthesis to emerging applications. *MRS Communications* **2019**, *10*, 112-122.

(5) Huang, L.; Ao, L.; Hu, D.; Wang, W.; Sheng, Z.; Su, W. Magneto-Plasmonic Nanocapsules for Multimodal-Imaging and Magnetically Guided Combination Cancer Therapy. *Chem. Mater.* **2016**, *28*, 5896-5904.

(6) Kim, J.; Piao, Y.; Hyeon, T. Multifunctional nanostructured materials for multimodal imaging, and simultaneous imaging and therapy. *Chem. Soc. Rev.* **2009**, *38*, 372-390.

(7) Xu, C.; Xie, J.; Ho, D.; Wang, C.; Kohler, N.; Walsh, E. G.; Morgan, J. R.; Chin, Y. E.; Sun, S. Au–Fe3O4 Dumbbell Nanoparticles as Dual-Functional Probes. *Angewandte Chemie International Edition* **2008**, *47*, 173-176.

(8) Li, Z.; Yin, S.; Cheng, L.; Yang, K.; Li, Y.; Liu, Z. Magnetic Targeting Enhanced Theranostic Strategy Based on Multimodal Imaging for Selective Ablation of Cancer. *Adv. Funct. Mater.* **2014**, *24*, 2312-2321.

(9) Efremova, M. V.; Naumenko, V. A.; Spasova, M.; Garanina, A. S.; Abakumov, M. A.; Blokhina, A. D.; Melnikov, P. A.; Prelovskaya, A. O.; Heidelmann, M.; Li, Z.-A.; Ma, Z.; Shchetinin, I. V.; Golovin, Y. I.; Kireev, I. I.; Savchenko, A. G.; Chekhonin, V. P.; Klyachko, N. L.; Farle, M.; Majouga, A. G.; Wiedwald, U. Magnetite-Gold nanohybrids as ideal all-in-one platforms for theranostics. *Scientific Reports* **2018**, *8*, 11295.

(10) Abed, Z.; Beik, J.; Laurent, S.; Eslahi, N.; Khani, T.; Davani, E. S.; Ghaznavi, H.; Shakeri-Zadeh, A. Iron oxide–gold core–shell nano-theranostic for magnetically targeted photothermal therapy under magnetic resonance imaging guidance. *Journal of Cancer Research and Clinical Oncology* **2019**, *145*, 1213-1219.

(11) Chen, H.; Hu, H.; Tao, C.; Clauson, R. M.; Moncion, I.; Luan, X.; Hwang, S.; Sough, A.; Sansanaphongpricha, K.; Liao, J.; Paholak, H. J.; Stevers, N. O.; Wang, G.; Liu, B.; Sun, D. Self-Assembled Au@Fe Core/Satellite Magnetic Nanoparticles for Versatile Biomolecule Functionalization. *ACS Appl. Mater. Interfaces* **2019**, *11*, 23858-23869.

(12) Gole, A.; Stone, J. W.; Gemmill, W. R.; zur Loye, H.-C.; Murphy, C. J. Iron Oxide Coated Gold Nanorods: Synthesis, Characterization, and Magnetic Manipulation. *Langmuir* **2008**, *24*, 6232-6237.

(13) Tzounis, L.; Doña, M.; Lopez-Romero, J. M.; Fery, A.; Contreras-Caceres, R. Temperature-Controlled Catalysis by Core–Shell–Satellite AuAg@pNIPAM@Ag Hybrid Microgels: A Highly Efficient Catalytic Thermoresponsive Nanoreactor. *ACS Appl. Mater. Interfaces* **2019**, *11*, 29360-29372.

(14) Chapman, B. S.; Wu, W.-C.; Li, Q.; Holten-Andersen, N.; Tracy, J. B. Heteroaggregation Approach for Depositing Magnetite Nanoparticles onto Silica-Overcoated Gold Nanorods. *Chem. Mater.* **2017**, *29*, 10362-10368.

(15) Truby, R. L.; Emelianov, S. Y.; Homan, K. A. Ligand-Mediated Self-Assembly of Hybrid Plasmonic and Superparamagnetic Nanostructures. *Langmuir* **2013**, *29*, 2465-2470.

(16) Sun, M.; Xu, L.; Ma, W.; Wu, X.; Kuang, H.; Wang, L.; Xu, C. Hierarchical Plasmonic Nanorods and Upconversion Core–Satellite Nanoassemblies for Multimodal Imaging-Guided Combination Phototherapy. *Adv. Mater.* **2016**, *28*, 898-904.

(17) Zheng, Y.; Thai, T.; Reineck, P.; Qiu, L.; Guo, Y.; Bach, U. DNA-Directed Self-Assembly of Core-Satellite Plasmonic Nanostructures: A Highly Sensitive and Reproducible Near-IR SERS Sensor. *Adv. Funct. Mater.* **2013**, *23*, 1519-1526.

(18) Li, N.; Tittl, A.; Yue, S.; Giessen, H.; Song, C.; Ding, B.; Liu, N. DNA-assembled bimetallic plasmonic nanosensors. *Light Sci. Appl.* **2014**, *3*, e226-e226.

(19) Raeesi, V.; Chou, L. Y. T.; Chan, W. C. W. Tuning the Drug Loading and Release of DNA-Assembled Gold-Nanorod Superstructures. *Adv. Mater.* **2016**, *28*, 8511-8518.

(20) Sun, D.; Tian, Y.; Zhang, Y.; Xu, Z.; Sfeir, M. Y.; Cotlet, M.; Gang, O. Light-Harvesting Nanoparticle Core–Shell Clusters with Controllable Optical Output. *ACS Nano* **2015**, *9*, 5657-5665.

(21) Waldeisen, J. R.; Wang, T.; Ross, B. M.; Lee, L. P. Disassembly of a Core–Satellite Nanoassembled Substrate for Colorimetric Biomolecular Detection. *ACS Nano* **2011**, *5*, 5383-5389.

(22) Ma, W.; Yin, H.; Xu, L.; Wu, X.; Kuang, H.; Wang, L.; Xu, C. Ultrasensitive aptamer-based SERS detection of PSAs by heterogeneous satellite nanoassemblies. *Chem. Commun.* **2014**, *50*, 9737-9740.

(23) Höller, R. P. M.; Dulle, M.; Thomä, S.; Mayer, M.; Steiner, A. M.; Förster, S.; Fery, A.; Kuttner, C.; Chanana, M. Protein-Assisted Assembly of Modular 3D Plasmonic

Raspberry-like Core/Satellite Nanoclusters: Correlation of Structure and Optical Properties. *ACS Nano* **2016**, *10*, 5740-5750.

(24) Wang, C.; Chen, J.; Talavage, T.; Irudayaraj, J. Gold Nanorod/Fe3O4 Nanoparticle "Nano-Pearl-Necklaces" for Simultaneous Targeting, Dual-Mode Imaging, and Photothermal Ablation of Cancer Cells. *Angew. Chem., Int. Ed.* **2009**, *48*, 2759-2763.

(25) Gandra, N.; Abbas, A.; Tian, L.; Singamaneni, S. Plasmonic Planet–Satellite Analogues: Hierarchical Self-Assembly of Gold Nanostructures. *Nano Lett.* **2012**, *12*, 2645-2651.

(26) Feng, J.; Wu, X.; Ma, W.; Kuang, H.; Xu, L.; Xu, C. A SERS active bimetallic core–satellite nanostructure for the ultrasensitive detection of Mucin-1. *Chem. Commun.* **2015**, *51*, 14761-14763.

(27) Ge, J.; Zhang, Q.; Zhang, T.; Yin, Y. Core–Satellite Nanocomposite Catalysts Protected by a Porous Silica Shell: Controllable Reactivity, High Stability, and Magnetic Recyclability. *Angewandte Chemie International Edition* **2008**, *47*, 8924-8928.

(28) Yang, Y.; Zhu, J.; Zhao, J.; Weng, G.-J.; Li, J.-J.; Zhao, J.-W. Growth of Spherical Gold Satellites on the Surface of Au@Ag@SiO2 Core–Shell Nanostructures Used for an Ultrasensitive SERS Immunoassay of Alpha-Fetoprotein. *ACS Appl. Mater. Interfaces* **2019**, *11*, 3617-3626.

(29) Dey, P.; Tabish, T. A.; Mosca, S.; Palombo, F.; Matousek, P.; Stone, N. Plasmonic Nanoassemblies: Tentacles Beat Satellites for Boosting Broadband NIR Plasmon Coupling Providing a Novel Candidate for SERS and Photothermal Therapy. *Small* **2020**, *16*, 1906780.

(30) Han, F.; Armstrong, T.; Andres-Arroyo, A.; Bennett, D.; Soeriyadi, A.; Alinezhad Chamazketi, A.; Bakthavathsalam, P.; Tilley, R. D.; Gooding, J. J.; Reece, P. J. Optical

tweezers-based characterisation of gold core–satellite plasmonic nano-assemblies incorporating thermo-responsive polymers. *Nanoscale* **2020**, *12*, 1680-1687.

(31) Zhang, M.; He, X.; Chen, L.; Zhang, Y. Preparation of IDA-Cu functionalized core–satellite Fe3O4/polydopamine/Au magnetic nanocomposites and their application for depletion of abundant protein in bovine blood. *J. Mater. Chem.* **2010**, *20*, 10696-10704.

(32) Zhao, J.; Long, L.; Weng, G.; Li, J.; Zhu, J.; Zhao, J.-W. Multi-branch Au/Ag bimetallic core–shell–satellite nanoparticles as a versatile SERS substrate: the effect of Au branches in a mesoporous silica interlayer. *Journal of Materials Chemistry C* **2017**, *5*, 12678-12687.

(33) Carbone, L.; Cozzoli, P. D. Colloidal heterostructured nanocrystals: Synthesis and growth mechanisms. *Nano Today* **2010**, *5*, 449-493.

(34) Ge, J.; Huynh, T.; Hu, Y.; Yin, Y. Hierarchical Magnetite/Silica Nanoassemblies as Magnetically Recoverable Catalyst–Supports. *Nano Lett.* **2008**, *8*, 931-934.

(35) Kuttner, C.; Höller, R. P. M.; Quintanilla, M.; Schnepf, M. J.; Dulle, M.; Fery, A.; Liz-Marzán, L. M. SERS and plasmonic heating efficiency from anisotropic core/satellite superstructures. *Nanoscale* **2019**, *11*, 17655-17663.

(36) Pazos-Perez, N.; Fitzgerald, J. M.; Giannini, V.; Guerrini, L.; Alvarez-Puebla, R. A. Modular assembly of plasmonic core–satellite structures as highly brilliant SERS-encoded nanoparticles. *Nanoscale Advances* **2019**, *1*, 122-131.

(37) Chen, X.; Liang, M.-M.; Xu, J.; Sun, H.-L.; Wang, C.; Wei, J.; Zhang, H.; Yang, W.-M.; Yang, Z.-L.; Sun, J.-J.; Tian, Z.-Q.; Li, J.-F. Unveiling the size effect of Pt-on-Au nanostructures on CO and methanol electrooxidation by in situ electrochemical SERS. *Nanoscale* **2020**, *12*, 5341-5346.

(38) Xiao, Q.; Zheng, X.; Bu, W.; Ge, W.; Zhang, S.; Chen, F.; Xing, H.; Ren, Q.; Fan, W.; Zhao, K.; Hua, Y.; Shi, J. A Core/Satellite Multifunctional Nanotheranostic for in Vivo Imaging and Tumor Eradication by Radiation/Photothermal Synergistic Therapy. *J. Am. Chem. Soc.* **2013**, *135*, 13041-13048.

(39) De Silva Indrasekara, A. S.; Norton, S. J.; Geitner, N. K.; Crawford, B. M.; Wiesner, M. R.; Vo-Dinh, T. Tailoring the Core–Satellite Nanoassembly Architectures by Tuning Internanoparticle Electrostatic Interactions. *Langmuir* **2018**, *34*, 14617-14623.

(40) He, R.; Cheng, Y.; Jin, T.; Jiang, M.; Chen, C.; Xu, G. Plasmonic Core/Satellite Heterostructure with Hierarchical Nanogaps for Raman Spectroscopy Enhanced by Shell-Isolated Nanoparticles. *Advanced Optical Materials* **2014**, *2*, 788-793.

(41) Maas, M.; Silvério, C. C.; Laube, J.; Rezwan, K. Electrostatic assembly of zwitterionic and amphiphilic supraparticles. *J. Colloid Interface Sci.* **2017**, *501*, 256-266.

(42) Schütz, M.; Schlücker, S. Molecularly linked 3D plasmonic nanoparticle core/satellite assemblies: SERS nanotags with single-particle Raman sensitivity. *Phys. Chem. Chem. Phys.* **2015**, *17*, 24356-24360.

(43) Goel, S.; Ferreira, C. A.; Chen, F.; Ellison, P. A.; Siamof, C. M.; Barnhart, T. E.; Cai, W. Activatable Hybrid Nanotheranostics for Tetramodal Imaging and Synergistic Photothermal/Photodynamic Therapy. *Adv. Mater.* **2018**, *30*, 1704367.

(44) Zheng, Y.; Rosa, L.; Thai, T.; Ng, S. H.; Juodkazis, S.; Bach, U. Phase controlled SERS enhancement. *Scientific Reports* **2019**, *9*, 744.

(45) Gu, D. H.; Lee, J.; Ban, H. W.; Lee, G.; Song, M.; Choi, W.; Baek, S.; Jeong, H.; Lee, S. Y.; Choi, Y.; Park, J.; Park, Y. I.; Son, J. S. Colloidal Suprastructures Self-Organized from Oppositely Charged All-Inorganic Nanoparticles. *Chem. Mater.* **2020**, *32*, 8662-8671.

(46) Chen, Y.; Wang, Z.; He, Y.; Yoon Young, J.; Jung, J.; Zhang, G.; Lin, Z. Light-enabled reversible self-assembly and tunable optical properties of stable hairy nanoparticles. *Proceedings of the National Academy of Sciences* **2018**, *115*, E1391-E1400.

(47) Liu, Y.; Han, X.; He, L.; Yin, Y. Thermoresponsive Assembly of Charged Gold Nanoparticles and Their Reversible Tuning of Plasmon Coupling. *Angewandte Chemie International Edition* **2012**, *51*, 6373-6377.

(48) Nie, Z.; Fava, D.; Kumacheva, E.; Zou, S.; Walker, G. C.; Rubinstein, M. Self-assembly of metal–polymer analogues of amphiphilic triblock copolymers. *Nat. Mater.* **2007**, *6*, 609-614.

(49) Strozyk, M. S.; Chanana, M.; Pastoriza-Santos, I.; Pérez-Juste, J.; Liz-Marzán, L. M. Protein/Polymer-Based Dual-Responsive Gold Nanoparticles with pH-Dependent Thermal Sensitivity. *Adv. Funct. Mater.* **2012**, *22*, 1436-1444.

(50) Chovnik, O.; Balgley, R.; Goldman, J. R.; Klajn, R. Dynamically Self-Assembling Carriers Enable Guiding of Diamagnetic Particles by Weak Magnets. *J. Am. Chem. Soc.* **2012**, *134*, 19564-19567.

(51) Schütz, M. B.; Lê, K.; Ilyas, S.; Mathur, S. Reversible Covalent Assembly of Nanoparticles through On-Surface Diels–Alder Reaction. *Langmuir* **2020**, *36*, 1552-1558.

(52) Lim, S. J.; Ma, L.; Schleife, A.; Smith, A. M. Quantum dot surface engineering: Toward inert fluorophores with compact size and bright, stable emission. *Coord. Chem. Rev.* **2016**, *320-321*, 216-237.

(53) Boles, M. A.; Ling, D.; Hyeon, T.; Talapin, D. V. The surface science of nanocrystals. *Nat. Mater.* **2016**, *15*, 141-153.

(54) Shirmardi Shaghasemi, B.; Dehghani, E. S.; Benetti, E. M.; Reimhult, E. Host–guest driven ligand replacement on monodisperse inorganic nanoparticles. *Nanoscale* **2017**, *9*, 8925-8929.

(55) Tebbe, M.; Kuttner, C.; Männel, M.; Fery, A.; Chanana, M. Colloidally Stable and Surfactant-Free Protein-Coated Gold Nanorods in Biological Media. *ACS Appl. Mater. Interfaces* **2015**, *7*, 5984-5991.

(56) Chen, Y.-S.; Frey, W.; Kim, S.; Kruizinga, P.; Homan, K.; Emelianov, S. Silica-Coated Gold Nanorods as Photoacoustic Signal Nanoamplifiers. *Nano Lett.* **2011**, *11*, 348-354.

(57) Carter, D. C.; Ho, J. X. Structure of Serum Albumin. In *Adv. Protein Chem.*, Anfinsen, C. B.; Edsall, J. T.; Richards, F. M.; Eisenberg, D. S., Eds. Academic Press: 1994; Vol. 45, pp 153-203.

(58) Benavidez, T. E.; Garcia, C. D. Potential-Assisted Adsorption of Bovine Serum Albumin onto Optically Transparent Carbon Electrodes. *Langmuir* **2013**, *29*, 14154-14162.

(59) Rizvi, M. H.; Wang, R.; Schubert, J.; Crumpler, W. D.; Rossner, C.; Oldenburg, A. L.; Fery, A.; Tracy, J. B. Magnetic Alignment for Plasmonic Control of Gold Nanorods Coated with Iron Oxide Nanoparticles. *Adv. Mater.* **2022**, *n/a*, 2203366.

(60) Kozek, K. A.; Kozek, K. M.; Wu, W.-C.; Mishra, S. R.; Tracy, J. B. Large-Scale Synthesis of Gold Nanorods through Continuous Secondary Growth. *Chem. Mater.* **2013**, *25*, 4537-4544.

(61) Park, J.; An, K.; Hwang, Y.; Park, J.-G.; Noh, H.-J.; Kim, J.-Y.; Park, J.-H.; Hwang, N.-M.; Hyeon, T. Ultra-large-scale syntheses of monodisperse nanocrystals. *Nat. Mater.* **2004**, *3*, 891-895.

(62) Chen, R.; Christiansen, M. G.; Sourakov, A.; Mohr, A.; Matsumoto, Y.; Okada, S.; Jasanoff, A.; Anikeeva, P. High-Performance Ferrite Nanoparticles through Nonaqueous Redox Phase Tuning. *Nano Lett.* **2016**, *16*, 1345-1351.

(63) Liu, S.; Chen, G.; Prasad, P. N.; Swihart, M. T. Synthesis of Monodisperse Au, Ag, and Au–Ag Alloy Nanoparticles with Tunable Size and Surface Plasmon Resonance Frequency. *Chem. Mater.* **2011**, *23*, 4098-4101.

(64) Scarabelli, L.; Sánchez-Iglesias, A.; Pérez-Juste, J.; Liz-Marzán, L. M. A "Tips and Tricks" Practical Guide to the Synthesis of Gold Nanorods. *The Journal of Physical Chemistry Letters* **2015**, *6*, 4270-4279.

3.6. Supporting Information

Electrostatic Self-Assembly of Magnetic and Plasmonic Nanoparticles on Gold Nanorods

Mehedi H. Rizvi,[1] *Ruosong Wang,*[2] *Jonas Schubert,* [2] *Christian Rossner,* [2,3] *Andreas Fery,* [2,4] *Joseph B. Tracy**[1]

[1]*Department of Materials Science and Engineering, North Carolina State University, Raleigh, North Carolina 27695, United States*

[2]*Leibniz-Institut für Polymerforschung Dresden e.V., Institute for Physical Chemistry and Polymer Physics, 01069 Dresden, Germany*

[3]*Dresden Center for Intelligent Materials (DCIM), Technische Universität Dresden, 01069 Dresden, Germany*

[4]*Chair for Physical Chemistry of Polymeric Materials, Technische Universität Dresden, 01062 Dresden, Germany*

Corresponding E-mail: jbtracy@ncsu.edu

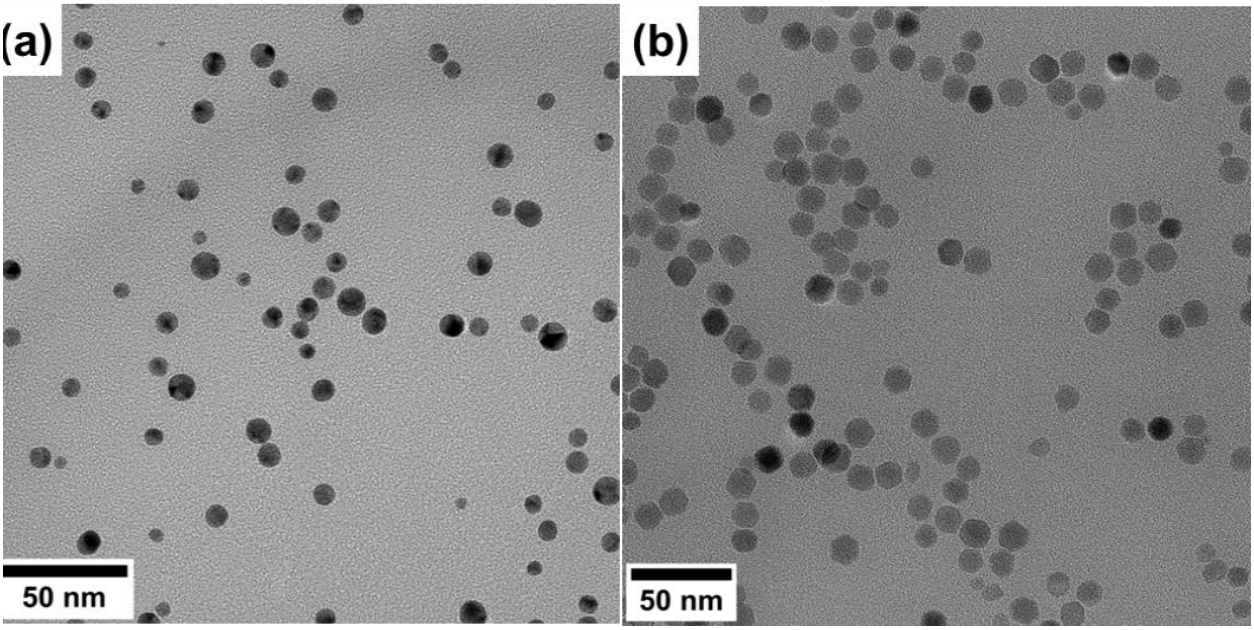

Figure 3.6. TEM images of (a) PEI-GNPs and (b) PEI-Fe_3O_4 NPs.

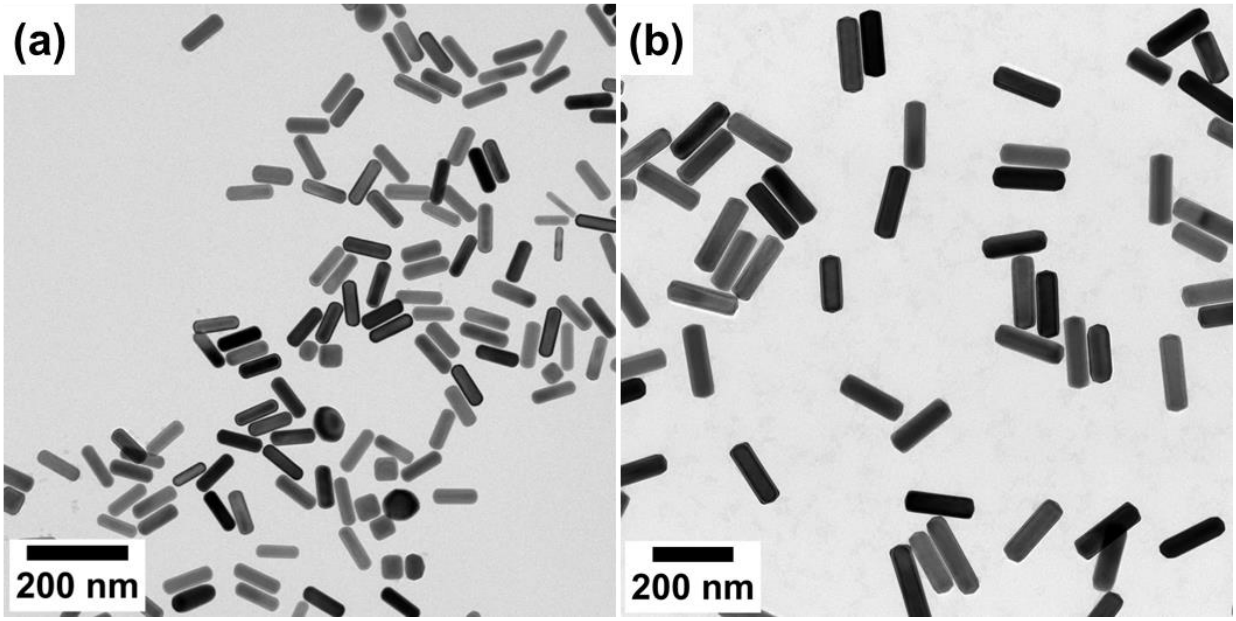

Figure 3.7. TEM images of BSA-GNRs of two different sizes (a) 76 nm × 26 nm and (b) 153 nm × 46 nm.

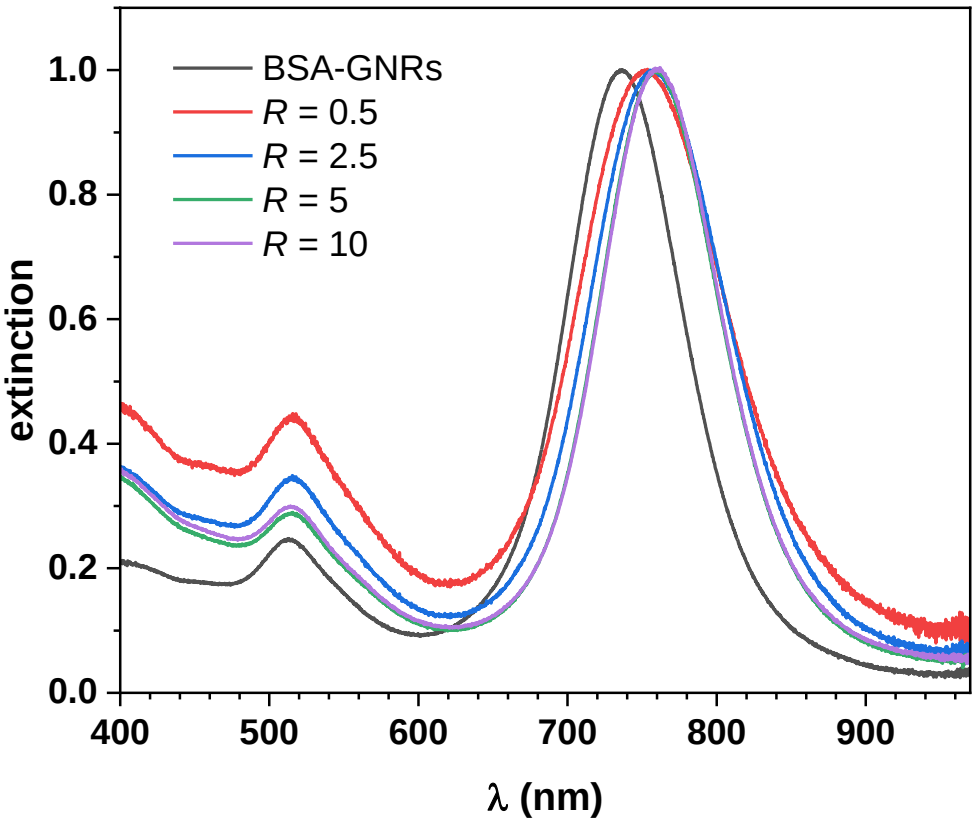

Figure 3.8. Extinction spectra of purified MagGNRs after conducting assembly at four different concentrations of satellite PEI-Fe_3O_4 NPs. The extinction ratio (R) of PEI-Fe_3O_4 NPs and BSA-GNRs (at 400 nm) was maintained at R = 0.5, 2.5, 5 and 10, which corresponds to 34, 174, 348 and 696 PEI-Fe_3O_4 NPs available for assembly per BSA-GNR. A sufficiently high excess of satellite NPs is required to avoid bridging of MagGNRs and broadening of the extinction spectra. Increasing the satellite NPs from 348 to 696 did not further alter extinction spectra. Based on this result, a concentration of satellite NPs near 350 PEI-Fe_3O_4 NPs per BSA-GNR core was chosen for all other experiments.

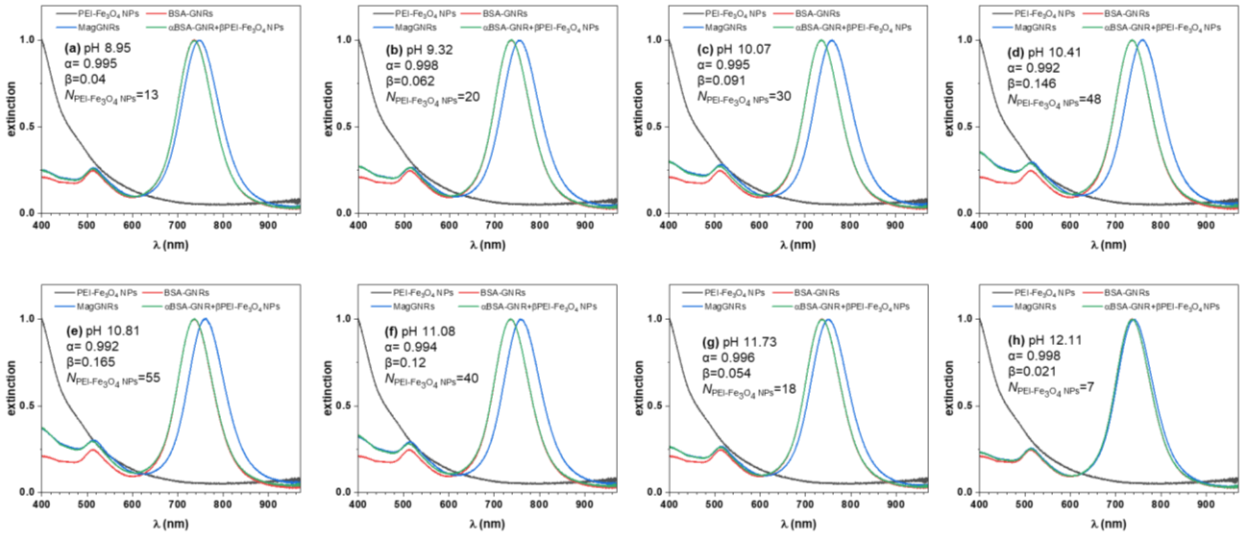

Figure 3.9. Plots of αBSA-GNRs + βPEI-Fe_3O_4 NPs and comparison with extinction spectra for MagGNRs, BSA-GNRs and PEI-Fe_3O_4 NPs. The coefficients α and β are used to calculate $N_{PEI\text{-}Fe3O4\ NPs}$, the average number of PEI-Fe_3O_4 NPs per MagGNR, reported in Figure 1b.

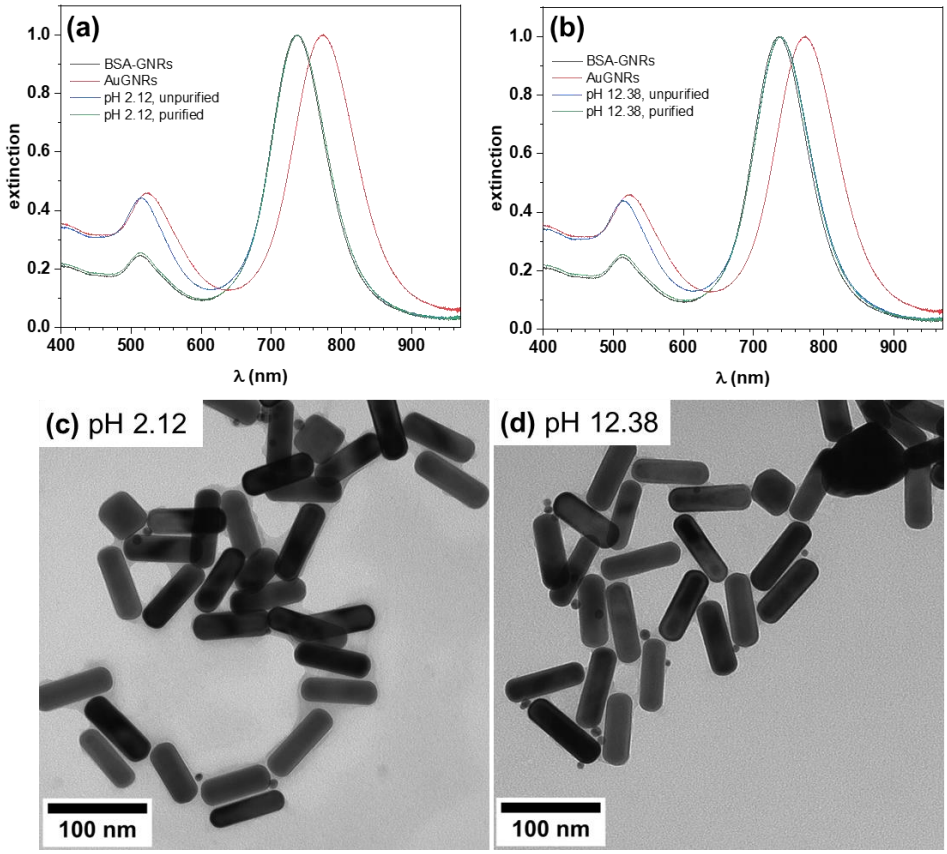

Figure 3.10. Extinction spectra of BSA-GNRs, AuGNRs, and AuGNRs after adjusting the pH to (a) 2.12 and (b) 12.38 to drive disassembly, with spectra acquired both before and after purification. TEM images of disassembled AuGNRs after purification at pH (c) 2.12 and (d) 12.38.

CHAPTER 4. Magnetic Alignment for Plasmonic Control of Gold Nanorods Coated with Iron Oxide Nanoparticles

This chapter in includes a manuscript reprint "Magnetic Alignment for Plasmonic Control of Gold Nanorods Coated with Iron Oxide Nanoparticles" authored by Mehedi H. Rizvi, Ruosong Wang, Jonas Schubert, William D. Crumpler, Christian Rossner, Amy L. Oldenburg, Andreas Fery, and Joseph B. Tracy. The manuscript has been accepted for publication in Advanced Materials. My contribution includes doing experiments, analyzing data, and writing the manuscript. Dr. Rossner performed and analyzed small angle X-ray scattering measurement. Dr. Oldenburg developed the mathematical modelling based on the experimental data we provided.

Magnetic Alignment for Plasmonic Control of Gold Nanorods Coated with Iron Oxide Nanoparticles

*Mehedi H. Rizvi, Ruosong Wang, Jonas Schubert, William D. Crumpler, Christian Rossner, Amy L. Oldenburg, Andreas Fery, and Joseph B. Tracy**

M. H. Rizvi, W. D. Crumpler, Prof. J. B. Tracy
Department of Materials Science and Engineering, North Carolina State University, Raleigh, North Carolina 27695, United States
E-mail: jbtracy@ncsu.edu

R. Wang, Dr. J. Schubert, Dr. C. Rossner, Prof. A. Fery
Leibniz-Institut für Polymerforschung Dresden e.V, Institute for Physical Chemistry and Polymer Physics, 01069 Dresden, Germany

Dr. C. Rossner
Dresden Center for Intelligent Materials (DCIM), Technische Universität Dresden, 01069 Dresden, Germany

Prof. A. Fery
Chair for Physical Chemistry of Polymeric Materials, Technische Universität Dresden, 01062 Dresden, Germany

Prof. A. L. Oldenburg
Department of Physics & Astronomy, University of North Carolina, Chapel Hill, North Carolina 27599, United States

Keywords: gold nanorods, iron oxide, surface plasmon resonance, magneto-optical effect, dipolar interactions

Plasmonic nanoparticles that can be manipulated with magnetic fields are of interest for advanced optical applications, diagnostics, imaging, and therapy. Alignment of gold nanorods yields strong polarization-dependent extinction, and use of magnetic fields is appealing because they act through space and can be quickly switched. In this work, cationic polyethyleneimine-functionalized superparamagnetic Fe_3O_4 nanoparticles (NPs) are deposited on the surface of anionic gold nanorods coated with bovine serum albumin. The magnetic gold nanorods (MagGNRs) obtained through mixing maintain the distinct optical properties of plasmonic gold nanorods that are minimally perturbed by the magnetic overcoating. Magnetic alignment of MagGNRs arising from magnetic dipolar interactions on the anisotropic gold nanorod core is comprehensively characterized, including structural characterization and enhancement (suppression) of the longitudinal surface plasmon resonance and suppression (enhancement) of the transverse surface plasmon resonance for light polarized parallel (orthogonal) to the magnetic field. MagGNRs can also be driven in rotating magnetic fields to rotate at frequencies of at least 17 Hz. For suitably large gold nanorods (148 nm long) and Fe_3O_4 NPs (13.4 nm diameter), significant alignment is possible even in modest (<500 Oe) magnetic fields. An analytical model provides a unified understanding of the magnetic alignment of MagGNRs.

4.1. Introduction

The anisotropic shape of gold nanorods (GNRs) endows them with unique wavelength-tunable and polarization-dependent optical properties that find potential applications in photothermal therapy, colorimetric sensing, bioimaging and optoelectronics.[1-8] Building on the refinement of methods for synthesizing GNRs over the last two decades,[9,10] numerous techniques have been developed for aligning and assembling GNRs, yielding novel optical properties.[11] GNRs have longitudinal and transverse surface plasmon resonances (LSPR and TSPR) that are excited

when the electric field of light is oriented along the length and diameter, respectively. The LSPR is more intense than the TSPR, and the wavelength of the LSPR depends on the aspect ratio of the nanorod, which allows tuning into the near-infrared spectrum. Alignment of GNRs allows for selective excitation of the LSPR or TSPR and has been achieved through stretching polymer films,[12-14] electrospinning polymer fibers,[15,16] controlled evaporation-mediated deposition,[17,18] deposition on templates,[19-23] wrinkle-assisted assembly,[24] mechanical brushing[25] and dispersion with liquid crystals.[26-31] Although some of these techniques for alignment can provide a high degree of ordering, the ability to dynamically align GNRs dispersed in liquids using applied magnetic or electric fields is appealing for its speed and reversibility. Aligning GNRs using electric fields, however, requires high field strengths and small, sub-mm electrode separation.[32-36] Optical torque has also been employed to align single GNRs in solution but generally requires intense, highly focused light, and is thus restricted to small sample volumes.[37] Applying magnetic fields, in contrast, does not require direct contact of a solution with electrodes and can be performed over large sample volumes.[38,39] While colloidal synthesis of GNRs with precisely engineered optical properties has become commonplace, we are not aware of previous reports of the deposition of magnetic materials onto GNRs together with a demonstration of alignment using magnetic fields, likely due to challenges achieving sufficiently large magnetic anisotropy for magnetic alignment.

Magnetic alignment of GNRs has thus far involved synthesis approaches that impair the optical properties of GNRs, as compared with well-established methods for synthesizing non-magnetic GNRs coated with cetyltrimethylammonium bromide (CTAB). Specifically, magnetically alignable GNRs thus far have high background extinction, broad LSPRs, and low ratios of LSPR to TSPR extinction. To provide an overview of the state of the field, it is important to briefly review these previous reports. Segmented nanorods have been prepared by

electrodepositing alternating layers of Au and Ni rods in porous anodic aluminum oxide templates.[40,41] The segmented nanorods could be aligned and rotated in a rotating magnetic field.[42-45] In approaches pioneered by Yadong Yin and coworkers, the magnetic shape anisotropy energy of iron oxide rods was utilized to align GNRs. Large (~200 nm) hematite nanorods were overcoated with Au shells[46] or decorated with GNRs on their surface with approximate (due to the curvature of the hematite nanorods) coalignment of their long axes.[47] In another method, elongated voids within silica nanorods with embedded magnetite (Fe_3O_4) nanorods were filled with gold, resulting in embedded GNRs with their long axes coaligned with the magnetite nanorods.[48] While these studies showed that magnetic alignment of GNRs is possible, introduced important concepts, and demonstrated applications of these materials, the shortcomings in their optical properties are significant. In this work, we address these issues and report magnetic GNRs, in which the narrow and intense LSPR of the GNR core and low background extinction are preserved during assembly of Fe_3O_4 nanoparticles (NPs) on their surface. The NPs do not dramatically alter the optical properties of the GNR cores. GNRs with magnetic overcoatings have potential biomedical applications, for example multimodal imaging and photothermal therapy which are further supported by the biocompatibility of Au and Fe_3O_4.[49,50] Magnetic alignment and manipulation of GNRs and related anisotropic structures have been applied in magnetochromic sensors,[46,51] photothermal actuators,[52] gyromagnetic imaging,[53] and nanoelectromechanical systems like nanomotors for controlled biochemical drug release.[43]

Magnetic alignment of anisotropic micro- and nanostructures has been demonstrated by depositing spherical magnetic NPs on their surfaces, including Al_2O_3 microplatelets,[54] cellulose microcrystals,[55] high aspect-ratio $CaSO_4$ nanorods,[54] polymer microrods,[56] SiC whiskers,[57,58] Te nanorods,[59] Ag nanowires,[60] and carbon nanotubes.[61] Hybrid nanorods composed of spherical

magnetic and plasmonic NPs formed using templates can also be aligned in magnetic fields.[62] In general, assembly methods using well-optimized methods for homogeneous nucleation and growth of NPs is attractive, because seeded-growth involving a change in composition between the seed and material deposited can be challenging and strongly depends on the specific system. The mechanism of alignment of anisotropic non-magnetic particles using coatings of magnetic NPs is based on coupling of their magnetic dipoles. For a pair of magnetic NPs that are close enough to have interacting magnetic dipoles, magnetostatics favors alignment of the dimer parallel to an applied magnetic field, giving head-to-tail alignment (negative energy) instead of side-by-side alignment (positive energy). When decorating magnetic NPs on the surface of a larger prolate nanostructure (i.e., nanorod in this work), alignment parallel to the field direction is the state with the lowest magnetostatic energy because the numbers of head-to-tail and side-by-side interactions between adjacent pairs of NPs are maximized and minimized, respectively. Conversely, alignment perpendicular to the long axis exhibits the highest magnetostatic energy by maximizing and minimizing the numbers of side-by-side and head-to-tail interactions, respectively. As a result, these dipolar interactions can impart uniaxial magnetic anisotropy to the nanorod, causing it to align with the field, if the energy barrier U_{barrier} between configurations for parallel and perpendicular alignment is high enough to overcome the contributions of thermal energy to the Brownian motion of the nanorod within a solvent. The magnetostatic origins of the torque that can align anisotropic nanostructures coated with magnetic NPs are closely related to torques that align chains of magnetic particles with applied magnetic fields.[63,64]

Despite several reports of overcoating GNRs with spherical iron oxide NPs,[49,50,65] to the best of our knowledge, alignment of these structures in magnetic fields has not been reported. Alignment of GNRs with low aspect ratios, giving LSPRs of ~800-1000 nm, is expected to be

challenging because $U_{barrier}$ decreases with decreasing aspect ratio, yet there is great interest in GNRs with these aspect ratios for many applications, including imaging and therapy.[2,4,66] If the loading of magnetic NPs is too low or their sizes too small, that reduces $U_{barrier}$ and limits magnetic alignment. The nanostructures that have been aligned using coatings of spherical magnetic NPs are generally both large, with at least one dimension exceeding 300 nm,[59] and have high aspect ratios, which both contribute to a higher $U_{barrier}$. For all magnetic alignment approaches, an additional consideration is avoiding undesired agglomeration of structures coated with magnetic NPs, which occurs if the magnetic moments interact too strongly, for example if the magnetic moments of the magnetic NPs are too large, or if they are ferromagnetic. Use of superparamagnetic NPs is helpful for providing large magnetic moments, while avoiding strong long-range interactions.[67]

In this work, we demonstrate and characterize the magnetic alignment of GNRs with overcoatings of superparamagnetic NPs. Mixing GNRs functionalized with anionic bovine serum albumin (BSA-GNRs) and Fe_3O_4 NPs functionalized with cationic polyethyleneimine (PEI-Fe_3O_4 NPs) under optimized conditions yields MagGNRs, consisting of BSA-GNR cores with dense shells of PEI-Fe_3O_4 NPs. Magnetic dipolar interactions among neighboring Fe_3O_4 NPs decorating the GNR core give rise to magnetic anisotropy, which causes the MagGNRs to align parallel to applied magnetic fields, enabling non-contact, magnetic manipulation of the LSPR and TSPR. Two sizes of GNR cores and Fe_3O_4 satellite NPs are investigated, revealing that both large GNR cores and large Fe_3O_4 NPs are necessary for obtaining significant alignment in magnetic fields. Alignment is observed even in low magnetic fields and begins to saturate at a field of 500 Oe, which is readily obtained using permanent magnets. Multiple methods are employed to comprehensively characterize the magnetic alignment of MagGNRs: transmission electron

microscopy (TEM) to directly observe alignment in 2D after drying on substrates, small angle X-ray scattering (SAXS) to directly measure the distribution of MagGNR orientations in colloidal dispersion, confirm a model for 3D angular distributions, and predict $U_{barrier}$, and polarized optical extinction spectroscopy to characterize magnetically modulated optical properties and independently validate $U_{barrier}$ under the same model.

4.2. Results and Discussion

Two different sizes of MagGNRs were synthesized and characterized with a host of methods to probe their structure, chemistry, and optical and magnetic properties, including their organization and response to applied magnetic fields. The discussion focuses chiefly on the large MagGNRs, because they exhibit better alignment in magnetic fields than small MagGNRs do. For this reason, some of the characterization was performed only on the large MagGNRs. In addition to reporting the alignment of MagGNRs and their novel magneto-optical properties, a major theme in this work is quantifying their alignment and extracting $U_{barrier}$ from this analysis. An analytical model is proposed for the angular orientation distribution of MagGNRs given $U_{barrier}$, which is numerically integrated to predict 2D and 3D order parameters. The model makes possible estimation of $U_{barrier}$ from characterization by TEM, SAXS, and optical extinction spectroscopy.

4.2.1. Synthesis and Assembly of MagGNRs

Small and large GNRs stabilized by cetyltrimethylammonium bromide (CTAB) were synthesized with average dimensions of 78 nm × 21 nm and 148 nm × 47 nm, respectively.[68-70] CTAB was displaced by bovine serum albumin (BSA) protein (Supporting Information, Figure S1), which made the BSA-coated GNRs negatively charged.[71] Spherical oleic acid-stabilized Fe_3O_4 NPs with an average diameter of 13.4 nm were prepared,[72] and the oleic acid was successively replaced with oleylamine[73] and then polyethylenimine (PEI), yielding cationically

charged PEI-Fe_3O_4 NPs that dispersed in water (Supporting Information, Figure S2). At the pH of 10.6 at which assembly occurs, typical zeta potentials of small and large BSA-GNRs and PEI-Fe_3O_4 NPs are -29 mV, -27 mV and +3 mV, respectively.

Mixing of BSA-GNRs and PEI-Fe_3O_4 NPs at room temperature initiated electrostatic self-assembly of coatings of the PEI-Fe_3O_4 NPs on the BSA-GNR cores, yielding MagGNRs. Excess PEI-Fe_3O_4 NPs are then removed via centrifugation. The MagGNRs disperse well in water, which is confirmed by lack of broadening of the LSPR and the good dispersion shown in TEM images. Good dispersion of MagGNRs is important for alignment in applied magnetic fields, since agglomerates could have multiple and disordered anisotropy axes and different alignment behaviors than individual MagGNRs. MagGNRs have good stability for at least several months when stored in the refrigerator.

4.2.2. Model for Quantifying Magnetic Alignment and Estimating $U_{\mathbf{barrier}}$

Before discussing experimental TEM, extinction spectroscopy, and SAXS measurements, we introduce a unified model for quantifying alignment of MagGNRs from these measurements. We first consider the dipole-dipole interaction between two identical NPs on the surface of a MagGNR, each with magnetic dipole moment **m** induced from an externally applied magnetic field **H**. As we show later, the NPs are superparamagnetic, for which **m** and **H** are co-aligned. If we define γ_{ij} as the angle between **m** and the displacement vector between the NPs, $\mathbf{r}_{ij}$, the magnetic potential energy can be written as (see Supporting Information):

$$U_{ij}\left(\gamma_{ij}\right) = \frac{\mu_0 \left|\mathbf{m}\right|^2}{4\pi \left|\mathbf{r}_{ij}\right|^3}\left(1-3\cos^2\gamma_{ij}\right), \qquad (1)$$

where μ_0 is the permeability of free space. To model the total potential energy of an assembled MagGNR, U_{MagGNR}, we consider it as the sum of the potential energies U_{ij} arising from

each pair of NPs decorating the GNR core. In this study, we are primarily interested in the θ-dependence of U_{MagGNR}, where θ is defined as the angle between **H** and the long axis of the GNR (Figure 4.1). After performing this summation, the θ-dependence may be written as:

$$U_{MagGNR}(\theta) = -nk_BT\cos^2\theta\,, \qquad (2)$$

where n is a dimensionless number that depends upon **m** and the number and positions of the NPs decorating the MagGNR. We further note that U_{MagGNR} has a common functional form observed in related systems. The energy of a single-domain magnetic NP by the Stoner-Wohlfarth model with its magnetization in the same direction as **H**[74] and the potential energy in optical trapping experiments of GNRs both have a $-\cos^2\theta$ dependence.[37] Importantly, n quantifies the magnetic trap depth as a multiple of the thermal energy, k_BT. This can be seen by writing the trap depth as the difference in potential energy between a MagGNR oriented perpendicular (high energy) versus parallel (low energy) to the magnetic field direction:

$$U_{barrier} = U_{MagGNR}(90°) - U_{MagGNR}(0°) = nk_BT\,, \qquad (3)$$

which corresponds to $n \times 25.9$ meV at room temperature. We expect that n should be $\gtrsim 1$ for significant magnetic alignment.

To characterize the magnetic alignment for a given trap depth, we model the angular distribution function f_θ of an ensemble of MagGNRs in thermal equilibrium according to the canonical ensemble:[75]

$$f_\theta = \frac{e^{-U_{MagGNR}(\theta)/k_BT}}{\int_0^{2\pi}\int_0^{\pi} e^{-U_{MagGNR}(\theta')/k_BT}\sin\theta' d\theta' d\phi'}, \qquad (4)$$

where ϕ is the projected angle of the GNR into the plane perpendicular to the magnetic trap according to Figure 4.1. Because U_{MagGNR} is independent of ϕ, the distribution simplifies to:

$$f_\theta(n) = \frac{e^{n\cos^2\theta}}{2\pi \int_{-\pi/2}^{\pi/2} e^{n\cos^2\theta'} \left|\sin\theta'\right| d\theta'} = \frac{e^{n\cos^2\theta}}{Z(n)}, \qquad (5)$$

where the denominator (partition function *Z*) depends only on the trap depth *n*. The limits of integration have been modified such that f_θ is centered at $\theta = 0$, which is more physically relevant for considering deviations in the orientation of MagGNRs from **H**. Interestingly, Equation 5 is the well-known Maier-Saupe distribution,[76,77] which has been used extensively for modelling nematic ordering including magnetic rod alignment.[78] The distribution is normalized such that

$$2\pi \int_{-\pi/2}^{\pi/2} f_{\theta'} \left|\sin\theta'\right| d\theta' = 1, \qquad (6)$$

and the angular probability density is thus $2\pi f_\theta \sin\theta$. This provides a means for predicting metrics, such as the root-mean-squared angle θ_{RMS} (and others in the Supporting Information), which can be obtained by numerically integrating over the distribution as follows:

$$\theta_{RMS} = \sqrt{\langle \theta^2 \rangle} = \sqrt{2\pi \int_{-\pi/2}^{\pi/2} \theta'^2 f_{\theta'}(n) \left|\sin\theta'\right| d\theta'}\,. \qquad (7)$$

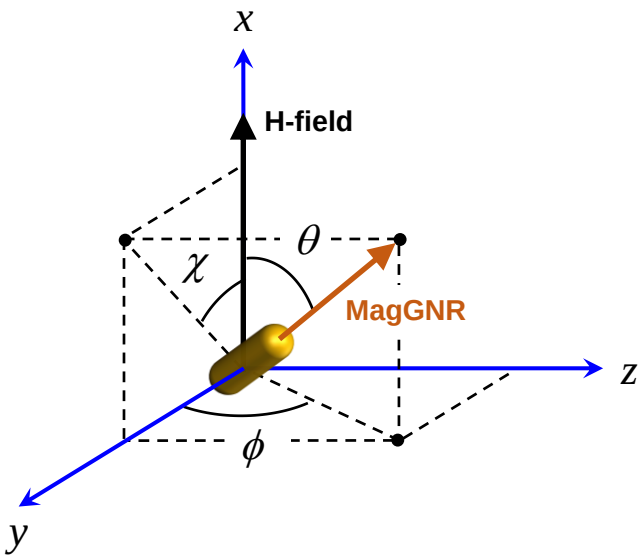

Figure 4.1. Angles used to describe the orientation of a MagGNR within a magnetic field directed along the x-axis. θ is the angle from the x-axis (**H**-field direction), ϕ is the projected angle in the yz-plane (perpendicular to **H**), and χ is the projected angle in the xy-plane (plane parallel to **H**).

We apply this model below to estimate *n* from measurements of the MagGNR orientation distributions under different conditions and with different experimental techniques. Knowing *n*, we then predict θ_{RMS}, and the 2D and 3D order parameters, S_{2D} and S_{3D} (additional derivations by ensemble averaging in the Supporting Information, Equation S24), and make a comprehensive comparison with experimental results.

4.2.3. Magnetic Alignment and Transmission Electron Microscopy

MagGNRs align parallel to applied magnetic fields. Dispersions of MagGNRs were dried onto TEM grids under uniform, in-plane 10 kOe magnetic fields by placing the grid between two poles of an electromagnet. Compared to the small MagGNRs, the large MagGNRs have more Fe_3O_4 NPs on their surface, resulting in more magnetic interactions and a larger expected value of $U_{barrier}$. This is consistent with our observation that large MagGNRs show a much higher extent of

alignment in magnetic fields than do small MagGNRs, as seen qualitatively by comparing Figure 4.2a,b with Figure 4.2c,d.

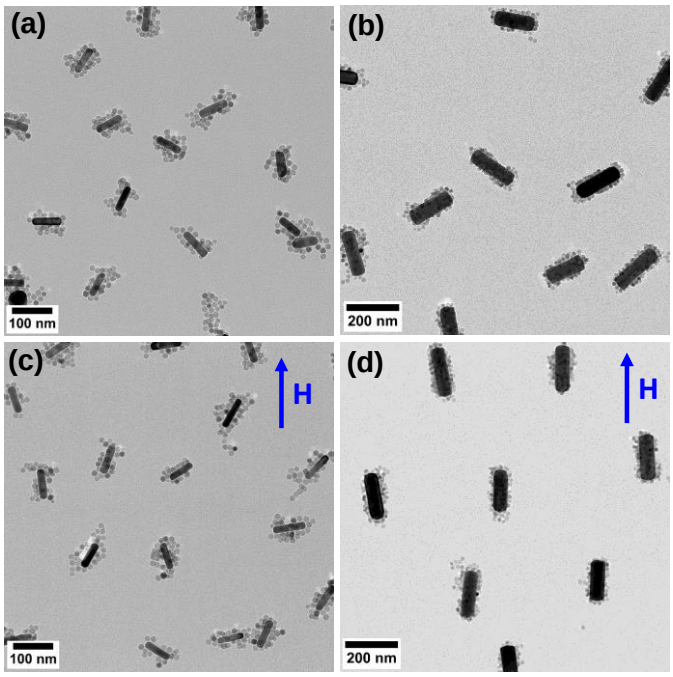

Figure 4.2. TEM images of MagGNRs dried on TEM grids with or without a 10 kOe magnetic field parallel to the grid and in the vertical direction in the images. (a) Small and (b) large MagGNRs without field and (c) small and (d) large MagGNRs dried in the magnetic field.

To quantify the extent of alignment, we performed an analysis consistent with three-dimensional (3D) characterization while dispersed in water, although subject to the limitations of the two-dimensional (2D) nature of TEM images and potential artifacts during drying. The 2D order parameter $S_{2D} = 2\langle\cos^2\chi\rangle$-1 was calculated from the angular distribution of 200 large MagGNRs dried in applied magnetic fields (Supporting Information, Figure S3).[26,33,79] S_{2D} of 0.70 was obtained for large MagGNRs, which is comparable to reported results for assembly with electric fields and capillary forces.[33,80] For small MagGNRs, S_{2D} is 0.21. For relating these 2D measurements to a 3D system, we can treat the observed orientation distribution on the TEM grid as the projection of the 3D orientation. If the plane of the TEM grid would be in the *xy*-plane in

Figure 4.1, then χ represents the angle between the long axis of the MagGNR and **H** that is measured in 2D TEM images. The polar angle θ, which has projected angle χ in the plane of the TEM grid, is used to define the 3D orientation distribution f_θ. We find $S_{2D} = 2\langle\cos^2\chi\rangle - 1 = 2\langle\cos\theta\rangle - 1$ (see Supporting Information). The trap depth parameter, n, can be extracted by interpolating a curve of predicted S_{2D} with n via numerical integration over the distribution f_θ. Values of n of 1.2 and 4.7 were obtained for small and large MagGNRs, respectively.

In the TEM images from drying in a magnetic field, while the large MagGNRs are well aligned parallel to **H**, the side-by-side distance (orthogonal to **H**) between the sides of neighboring MagGNRs is longer than the end-to-end distance (parallel to **H**) for MagGNRs arranged along the same line (Supporting Information, Figure S3). We attribute this to MagGNR-MagGNR (interparticle) magnetostatic (dipolar) interactions of coaligned magnetic domains, where side-by-side interactions are repulsive, and head-to-tail interactions are attractive. While the focus of this work is on well dispersed MagGNRs, such that these interparticle interactions are negligible, increasing the concentration during drying might increase these interparticle interactions and cause chaining.[81-83] In a control experiment, a TEM sample of MagGNRs prepared outside of the electromagnet was imaged and shown to have random orientation (Figure S4a,b), confirming the role of the magnetic field for driving alignment of the MagGNRs.

4.2.4. Optical Extinction Spectroscopy

Extinction spectra of the MagGNRs closely resemble those of BSA-GNRs, with two notable differences (Figure 4.3a,b). The LSPR of the MagGNRs is redshifted because the coating of Fe_3O_4 NPs modifies the dielectric environment on the surface of the BSA-GNRs, which is a well-known effect.[49,65] The spectra of the MagGNRs also have a shoulder that is most prominent below ~500 nm caused by the extinction of the Fe_3O_4 NPs in the blue. Most importantly, except

for the redshift, there is no significant decrease in the intensity of the LSPR and minimal broadening, which we have directly confirmed in an additional mixing experiment (Supporting Information, Figure S5). The lack of significant extinction of the Fe_3O_4 NPs at the LSPR of the GNRs underscores the optical compatibility of these materials.

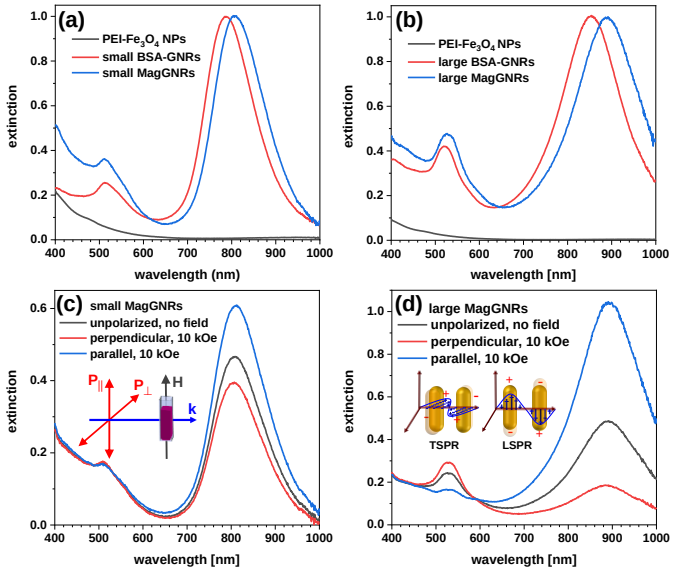

Figure 4.3. Optical extinction spectra of PEI-Fe_3O_4, BSA-GNRs and MagGNRs for (a) small and (b) large GNR cores normalized at LSPR intensity of 1. The extinction of PEI-Fe_3O_4 was normalized to the difference in the extinction of MagGNRs and BSA-GNRs at 400 nm. Unpolarized and polarized extinction spectra of MagGNRs in an electromagnet under zero field or uniform 10 kOe magnetic field for (c) smaller MagGNRs, and (d) larger MagGNRs without normalization. Both polarization directions **P** for light parallel or perpendicular to the magnetic field were measured.

Extinction spectra in applied uniform magnetic fields were acquired by placing a compact spectrophotometer into the gap of an electromagnet (Supporting Information, Figure S6). For polarized measurements, incident light with propagation direction **k** was transmitted normally through a polarizer film and then through the cuvette, where **H** was fixed in the plane of the

polarizer film. The polarization direction **P** could be oriented parallel or perpendicular to **H** (inset of Figure 4.3c). In an applied magnetic field of 10 kOe, the LSPR is enhanced (suppressed) and the TSPR is suppressed (enhanced) for light polarized parallel (perpendicular) to the direction of the applied magnetic field (Figure 4.3c,d). For large MagGNRs, there is an apparent isosbestic point at ~590 nm. In the limiting case of perfect alignment of GNRs, light polarized parallel (perpendicular) to the long axis of the GNRs can be approximated as exciting solely the LSPR (TSPR). As such, the more prominent polarization dependence of the LSPR and TSPR observed for the large MagGNRs is consistent with more complete alignment than for the small MagGNRs. The same experiments have been conducted using smaller PEI-Fe_3O_4 NPs with a diameter of 6.6 nm (compared to 13.4 nm) on large GNR cores (Supporting Information, Figure S7). There is no obvious alignment of these MagGNRs by TEM, though evidence of minor alignment is observed in the polarized extinction spectra. The size of the Fe_3O_4 NPs is therefore an important parameter for obtaining alignment, where larger Fe_3O_4 NPs are needed for stronger dipolar coupling and substantially increasing $U_{barrier}$ above thermal energy. For all other experiments reported here, the larger Fe_3O_4 NPs with a diameter of 13.4 nm were used.

The extent of alignment, as characterized by the Maier-Saupe model of Equation 5 and trap depth parameter *n*, can be quantified from experimental polarized extinction spectra in applied magnetic fields. Specifically, measurements of the $\log_{10}$-based extinction, $A_{\parallel}$ and $A_{\perp}$, at the LSPR wavelength (810 nm and 891 nm for small and large MagGNRs, respectively) within a ±10 nm wavelength band were averaged to suppress noise for parallel and perpendicular configurations, respectively, under a field of 10 kOe. The values at each wavelength were treated as independent measurements and analyzed in two ways. First, the anisotropy ratio was computed, which can be related to the MagGNR angular distribution as follows (see Supporting Information):

$$\frac{A_{\parallel}}{A_{\perp}} = \frac{\left\langle \cos^2\theta \right\rangle}{\left\langle \sin^2\theta \cos^2\phi \right\rangle} = 2\frac{\left\langle \cos^2\theta \right\rangle}{\left\langle \sin^2\theta \right\rangle}. \quad (8)$$

Corresponding values of *n* were extracted by interpolating a curve of predicted anisotropy ratio versus *n* according to Equation 8 via numerical integration over the distribution of Equation 5. The resulting values were *n* = 1.1 and 4.5 for small and large MagGNRs, respectively. This highlights the dramatic increase in U_{barrier}, when the core GNR size is increased.

Second, a more common, 3D order parameter was computed:

$$S_{3D,optical} = \frac{A_{\parallel} - A_{\perp}}{A_{\parallel} + 2A_{\perp}} = \frac{3\left\langle \cos^2\theta \right\rangle - 1}{2}, \quad (9)$$

which is related to the underlying angular distribution (see Supporting Information) and has been used extensively in other works.[26,29-31,84-86] S_{3D} has values between -0.5 and 1, where -0.5 indicates alignment perpendicular to the director, 0 indicates random alignment, and 1 indicates perfect alignment along the director. The measured $S_{3D,optical}$ for small and large MagGNRs in a 10 kOe magnetic field is 0.16 and 0.61, respectively. The latter is comparable to values for aligning dispersed GNRs with liquid crystals.[26,27,29]

Optical property measurements are also useful characterizing how the alignment of MagGNRs depends on the strength of the applied magnetic field. Polarized extinction spectra were acquired as a function of the applied magnetic field strength (Figure 4.4a,b), from which $S_{3D,optical}$ was calculated. There are only minor changes in the extinction for both polarization directions at fields above 500 Oe. The field dependence of $S_{3D,optical}$ was plotted (Figure 4.4c) to visualize this effect. At 4 kOe, $S_{3D,optical}$ is already saturated, and even at a much lower field of 250 Oe, $S_{3D,optical}$ is 91% of its maximum value at 10 kOe. In a control experiment, extinction spectra of BSA-GNRs without coatings of Fe_3O_4 NPs show no polarization dependence, confirming that they do not align in magnetic fields without the magnetic coatings (Supporting Information, Figure S4c). While

others have demonstrated minor alignment (S < 0.1) of GNRs in extremely high magnetic fields (~300 kOe), the extent of alignment at 10 kOe without magnetic overcoatings is negligibly small.[87]

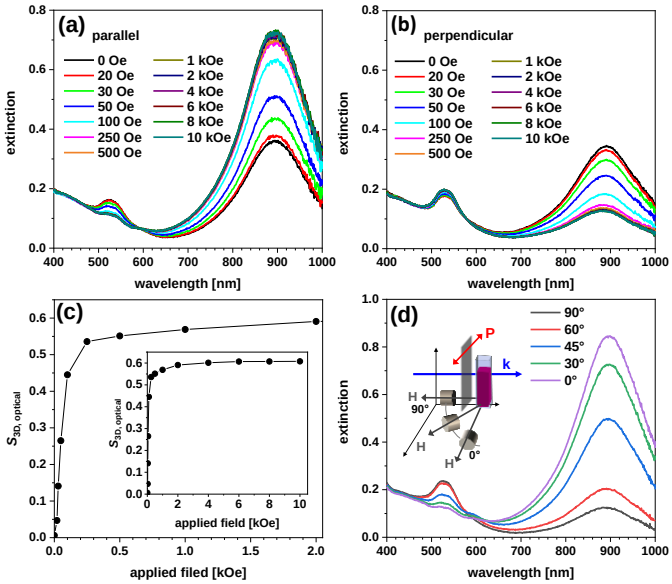

Figure 4.4. Polarized extinction spectra of large MagGNRs at different field strengths for light polarized (a) parallel, and (b) perpendicular to the magnetic field using an electromagnet (same geometry as in Figure 4.3c). (c) $S_{3D,\ optical}$ calculated from the polarized extinction at the LSPR as a function of applied field up to 2 kOe with inset showing up to 10 kOe. (d) Polarized extinction spectra acquired with a cylindrical magnet placed at different angles with respect to the light polarization direction.

H greater than 500 Oe can be easily obtained with permanent magnets, which give similar magnetic alignment to uniform magnetic fields without requiring an electromagnet. We observed that the intensities of the LSPR and TSPR can be modulated by moving the magnet to vary the angle of the magnetic field relative to a fixed polarization direction from 0° (parallel) to 90° (perpendicular) without substantially changing the field strength (Figure 4.4d). Light from the source propagates along **k** and through the polarizer film, sample, and detector, where the polarization direction **P** is orthogonal to **k** (inset of Figure 4.4d). A cylindrical magnet (1" diameter

and 1” length) is placed with one pole facing the sample and with separation of 1” between the face of the magnet and the side of the cuvette. When **H** makes an angle of 90° (0°) with **P**, the TSPR (LSPR) is enhanced and LSPR (TSPR) is diminished.

4.2.5. Visualizing and Tracking Magnetic Fields

Evidence of the alignment of large MagGNRs in magnetic fields can be observed by eye using permanent magnets and polarizer films (Figure 4.5). For example, a large cube (1” edge) magnet oriented vertically generates vertical field lines on the top face but approximately horizontal field lines outside the edge of the top face, which is verified in a simulation of the magnetic field distribution (Supporting Information, Figure S8). Unpolarized photos of cuvettes placed in both the vertical and horizonal field regions do not show significant difference for the regions of different field orientation (Figure 4.5a), whereas the colors change to magenta and pale brown in polarized light (Figure 4.5b,c, Supporting Information Video S1). For polarization parallel (perpendicular) to the magnetic field, the longitudinal (transverse) mode is preferentially excited and thus appears pale brown (magenta). The pale brown color is caused by damping of the TSPR, but excitation of the LSPR is not apparent, because the LSPR peak is outside of the visible spectrum. A similar demonstration was performed using a circular Halbach array, which generates a more uniform magnetic field compared to single permanent magnet (Supporting Information, Figure S9, Video S2).

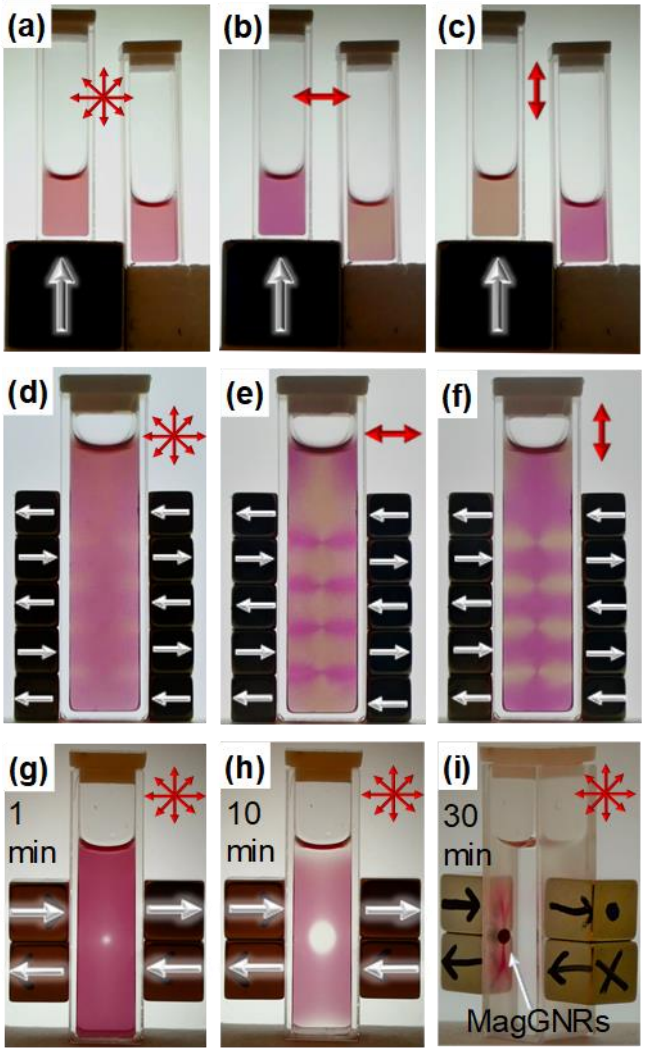

Figure 4.5. Photos of identical cuvettes with large MagGNRs placed on top of and next to the top face of a 1” cube magnet (a) unpolarized, (b) with horizontal polarizer, and (c) with vertical polarizer. Cuvette with large MagGNRs placed between arrays of 6 mm cube magnets (d) unpolarized polarizer, (e) with horizontal polarizer, and (f) with vertical polarizer. Nonuniform magnetic separation with four 10 mm cube magnets where a central bright spot appears in unpolarized photos taken after (g) 1 min, (h) 10 min, and (i) 30 min. The magnetic field and polarizer directions are indicated by single-headed and double-headed arrows, respectively.

Using arrays of permanent magnets allows programming of the magnetic field throughout the volume of the solution, resulting in patterns of color based on alignment of the MagGNRs and the polarization state of the light. Patterns of both colors are observed under polarized light when the cuvette is placed between two parallel arrays of 0.25" cube magnets (Figure 4.5d-f, Supporting Information, Figure S10, Video S3). The number and orientation of the magnets can further tune the color pattern as the magnetic field distribution changes (Supporting Information, Figures S11-13, Videos S4-S6). Magnetic separation is also noteworthy and can occur in a few minutes, when the magnets generate large magnetic field gradients. Soon after placing the cuvette between four 10-mm cube magnets, a central bright spot corresponding to a region depleted in MagGNRs grows as the MagGNRs are pulled toward the magnets (Figure 4.5g,h, Supporting Information, Video S7). The separated MagGNRs collected on the wall of the cuvette show the region of high field gradient at the interface between permanent magnets (Figure 4.5i). The MagGNRs readily redisperse after removing the magnets with shaking or mild sonication.

The appearance in polarized and unpolarized light can be understood in greater detail based on the number of longitudinal and transverse modes excited for a given combination of orientations of **k**, **P** (which is always orthogonal to **k** in this work), and **H**. For randomly oriented GNRs in unpolarized light, there is 1 LSPR associated with the long axis and 2 TSPRs associated with the two transverse axes. Aligning MagGNRs in the plane of the polarizer film and orthogonal to **k** removes the TSPR for alignment parallel to **k** and shifts the extinction to 1 LSPR and 1 TSPR for unpolarized light. Either mode can then be selectively excited with the polarizer, as in Figures 4.3c,d, 4a-c and Supporting Information, Figures S10a, S11a,b, S12a,b, S13a,b. In comparison, aligning the MagGNRs parallel to **k** (90° orientation in Figure 4.4d and Supporting Information, Figures S10b, S11c, S12c, S13c) suppresses the LSPR and excites 2 TSPRs for unpolarized light

or only 1 TSPR for polarized light, irrespective of the direction of **P**. Therefore, effects of magnetically aligning MagGNRs are also expected for unpolarized light but can be subtle and are enhanced with the polarizer. As already mentioned, the different colors observed in photographs and videos in this work arise predominantly from changes in the TSPR, because the LSPR is outside of the visible spectrum. It is important to note that we refer to unpolarized as ambient light that has not been purposefully polarized, but there can still be some unintended polarization from the light source and optical elements in the camera.

Dynamic magnetic alignment of the large MagGNRs can also be demonstrated by placing the cuvette on a magnetic stir plate, which generates a horizontal rotating magnetic field (Supporting Information, Figure S14, Video S8). The speed of oscillation of the colors tracks with the speed of the stir plate, even up to the maximum speed of 1000 rpm (16.7 Hz) (Supporting Information, Figure S15, Video S9). The rate of alignment and reorientation of MagGNRs could likely be increased by switching the magnetic field at higher frequency. For example, switching of GNRs with electric fields has been demonstrated at ~kHz frequencies,[35,43] which implies that for low-viscosity solvents, hydrodynamics do not restrict faster switching than demonstrated here.

4.2.6. Small Angle X-ray Scattering

SAXS measurements of dispersions of MagGNRs in magnetic fields of ~2 kOe generated in the gap between permanent magnets provide another, direct structural measure of the alignment of MagGNRs dispersed in water. Large MagGNRs show isotropic 2D scattering patterns without external magnetic fields, which become anisotropic when the MagGNRs align with the applied field direction (Figure 4.6a,b). The following directions and angles are depicted in Figure 4.1. The magnetic field creates an anisotropic scattering pattern that is more concentrated toward smaller $|q|$ values in the direction of **H**. The nanorod orientation is characterized by the polar angle θ

between the long axis of the nanorod main axis **H**, which points along the *x*-axis. χ is the angle of the projection of the long axis of the nanorod in the viewing plane (*xy*-plane). Our analysis of the results closely follows recent work of Rosén *et al.*[88] Initially, the right half of two-dimensional SAXS patterns, the half without the beam stop, was integrated into azimuthal distributions Ψ_χ by integrating over a range of q reflecting the characteristic sizes of the GNRs, i.e., in an interval $2\pi/L \leq |q| \leq 2\pi/d$,[88] where L and d are the length and diameter of the GNR core (excluding the Fe_3O_4 satellite NPs) obtained from TEM. After removing the background, Ψ_χ (Figure 4.6c,d) provides an estimate for the distribution of χ, the projected angle, which can be compared to the 2D distribution and analysis of TEM images (Supporting Information, Figure S3).

The distribution of the polar angle Ψ_θ can be calculated by fitting Ψ_χ with a linear combination of the first (3 and 5 for small and large GNRs, respectively, according to the criteria defined in [88]) even Legendre polynomials. Assuming that Ψ_χ is axisymmetric about **H** (i.e., the *x*-axis), Ψ_θ can be reconstructed from fitting Ψ_χ (Figure 4.6c,d) according to the previous work of Rosén *et al.*[88] To account for finite-size effects in the length of the nanorods and isotropic background, a Maier-Saupe distribution $f_\theta(n)$ (Equation 5) was then fit to the reconstructed Ψ_θ distribution but with a free baseline,[89] because such behavior has been reported for other magnetically aligned nanorods.[78] The experimental data match well with $f_\theta(n)$ for the small and large MagGNRs with respective trap depth parameter n of 0.8 and 3.8 (Figure 4.6e,f). $f_\theta \sin\theta$ is also plotted and describes the probability of finding a MagGNR oriented at angle θ in the dispersion. From the fitted parameter n, which describes the width of the distribution, the order parameter $S_{3D,SAXS}$ can be obtained by combining Equations 5, 6, 9:

$$S_{3D,SAXS} = \frac{\int_{-\pi/2}^{\pi/2} \left(\frac{3\cos^2\theta' - 1}{2} \right) e^{n\cos^2\theta'} \left|\sin\theta'\right| d\theta'}{\int_{-\pi/2}^{\pi/2} e^{n\cos^2\theta'} \left|\sin\theta'\right| d\theta'}. \quad (10)$$

The order parameter $S_{3D,SAXS}$ for large MagGNRs is 0.54, which is much higher than 0.11 for smaller MagGNRs.

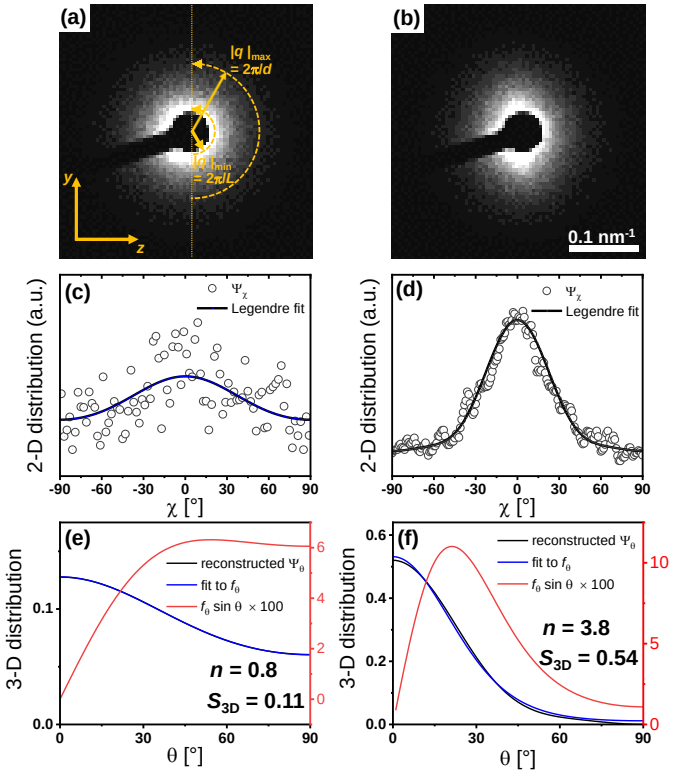

Figure 4.6. 2D SAXS patterns for large MagGNRs (a) without external magnetic field, and (b) with ~2 kOe magnetic field. The azimuthal profiles under magnetic field of the projected angle χ and fit to a linear combination of Legendre polynomials for (c) small, and (d) large MagGNRs. Reconstructed Ψ_θ and fit to f_θ , as well as the probability $f_\theta \sin\theta$, for (e) small and (f) large MagGNRs.

4.2.7. Summary of Analysis of Alignment of MagGNRs

As already discussed, each characterization method provides different primary data that allow for direct calculation of certain quantities – S_{2D} from TEM, S_{3D} from polarized extinction spectroscopy, and n from SAXS. Using the experimentally derived orientation distributions and the Maier-Saupe distribution as a model for magnetic alignment (Equation 5), we extracted n for each method. From knowledge of n, we then computed S_{2D}, S_{3D}, and θ_{RMS} under this model (Equation S24 and Equation 7), which are summarized in Figure 4.7. The estimates of $U_{barrier}$ based on n are largely consistent among all three characterization methods and for the larger MagGNRs are approximately 4 times that of the small MagGNRs. The effect of this increase is apparent in the inset figure of the angular distributions, showing how small MagGNRs only exhibit partial alignment against the randomizing effects of Brownian motion, while large MagGNRs exhibit a narrowed distribution centered around the magnetic field direction at $\theta = 0$. As expected from the similar n, values of S_{2D}, S_{3D}, and θ_{RMS} are also largely consistent among all three methods. It is important to consider that $U_{barrier}$ depends on the magnetization of the Fe_3O_4 NPs. This might explain the slightly lower ordering observed by SAXS, where the weaker magnetic field nearly saturates the NPs, than for TEM and extinction spectroscopy measurements, in which stronger magnetic fields fully saturate the NPs.

These results also compare favorably with previous reports of the magnetic alignment of GNRs.[44-48] In those studies, the high polarization-independent background would reduce the optical anisotropy (Equation 8) and $S_{3D,optical}$ (Equation 9), even if the GNRs are physically well aligned. Deviations in the shape of the Au nanostructures from rods or high magnetic loading could contribute to increased background and broadening that might cause reduced ordering, as assessed optically instead of by TEM or SAXS measurements. Therefore, agreement in quantification from

different characterization methods in this work suggests that there are minimal plasmonic shape impurities that could otherwise cause deviation.

It is also interesting to consider the 2D data collected as a function of the projected angle χ in the SAXS and TEM measurements. The distributions of χ obtained from TEM and SAXS analysis agree quite well for large MagGNRs (Supporting Information, Figure S3). However, χ for small MagGNRs from TEM images does not match as well with the SAXS distribution. Since U_{barrier} for small MagGNRs is smaller than for large MagGNRs, small MagGNRs might be more susceptible to drying effects when preparing substrates for TEM. Finally, the RMS polar angle, θ_{RMS}, displayed the same trend obtained by all three techniques.

		n		S_{3D}		S_{2D}		θ_{RMS}	
	H	*small*	*large*	*small*	*large*	*small*	*large*	*small*	*large*
TEM	10 kOe	1.2	4.7	0.17	0.63	0.21	0.70	54°	33°
SAXS	2 kOe	0.8	3.8	0.11	0.54	0.14	0.61	57°	37°
Optical	10 kOe	1.1	4.5	0.15	0.61	0.19	0.68	55°	34°

$$n = U_{barrier} / k_B T \qquad S_{3D,SAXS} = \frac{3\langle \cos^2 \theta \rangle - 1}{2} \qquad S_{2D,TEM} = 2\langle \cos^2 \chi \rangle - 1$$

$$f_\theta(n) \sim e^{n \cos^2(\theta)} \qquad S_{3D,Opt} = \frac{A_{\parallel} - A_{\perp}}{A_{\parallel} + 2A_{\perp}} \qquad \left.\begin{matrix} S_{2D,SAXS} \\ S_{2D,Opt} \end{matrix}\right\} = 2\langle \cos\theta \rangle - 1 \qquad \theta_{RMS} = \sqrt{\langle \theta^2 \rangle}$$

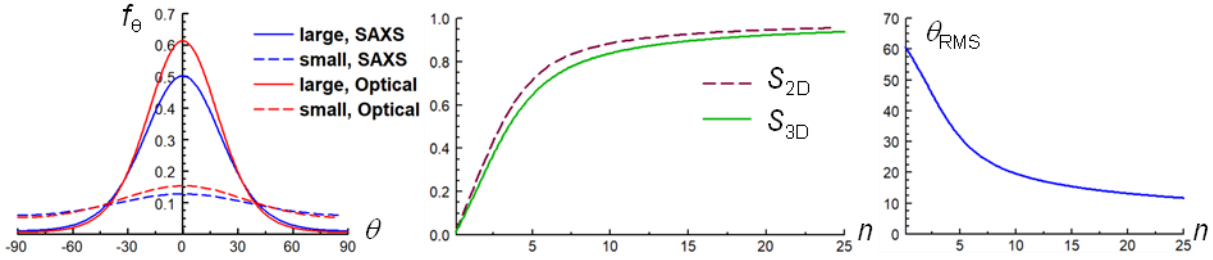

Figure 4.7. Top: n, S_{2D}, S_{3D}, and θ_{RMS} extracted from TEM, SAXS, and optical extinction measurements for small and large MagGNRs under magnetic fields of strengths indicated. Middle: Associated expressions used for calculations. Bottom: plots of (left) angular distribution functions and (middle and right) dependence of S_{2D}, S_{3D}, and θ_{RMS} on n.

4.2.8. Magnetic Property Measurements

Field- and temperature-dependent magnetometry measurements were performed on PEI-Fe_3O_4 NPs and large MagGNRs to investigate dipolar interactions within MagGNRs. Both samples were dispersed in poly(vinyl alcohol) (PVA) films to provide good dispersions. As expected, PEI-Fe_3O_4 NPs and MagGNRs are superparamagnetic at room temperature, based on the lack of magnetic hysteresis (Figure 4.8a). It is interesting to note that saturation of $S_{3D,optical}$ occurred at lower fields than magnetic saturation of the MagGNRs (Supplementary Information, Figure S16). This different field-dependent behavior is rooted in the field-dependence of $U_{barrier}$ for interacting superparamagnetic NPs, which is non-trivial to model and is beyond the scope of this work but is of interest for future studies.

Temperature-dependent measurements show the effects of dipolar interactions among Fe_3O_4 NPs on the surface of MagGNRs (Figure 4.8b,c). In temperature-dependent measurements, the sample is heated from 5 K to 300 K in a measuring field of 10 Oe after cooling in a 10 Oe field (FC) or cooling in zero field (ZFC). The temperature at the maximum of ZFC curve is defined as the superparamagnetic blocking temperature T_B, which is remarkably different for PEI-Fe_3O_4 NPs (109 K) and MagGNRs (177 K). The significant enhancement of T_B is consistent with an energetically stabilizing effect of dipolar coupling among Fe_3O_4 NPs on the surface of MagGNRs.[90,91] The flat shape of the FC curve for MagGNRs until reaching T_B further confirms strong coupling among the Fe_3O_4 NPs.[91] In contrast, in the FC curve of dispersed PEI-Fe_3O_4 NPs, the magnetization has significantly decreased before reaching T_B. [87] In summary, magnetometry measurements support the proposed mechanism of magnetic alignment, where dipolar interactions among Fe_3O_4 NPs on the surface of the large MagGNRs result in $U_{barrier}$ large enough to give significant alignment.

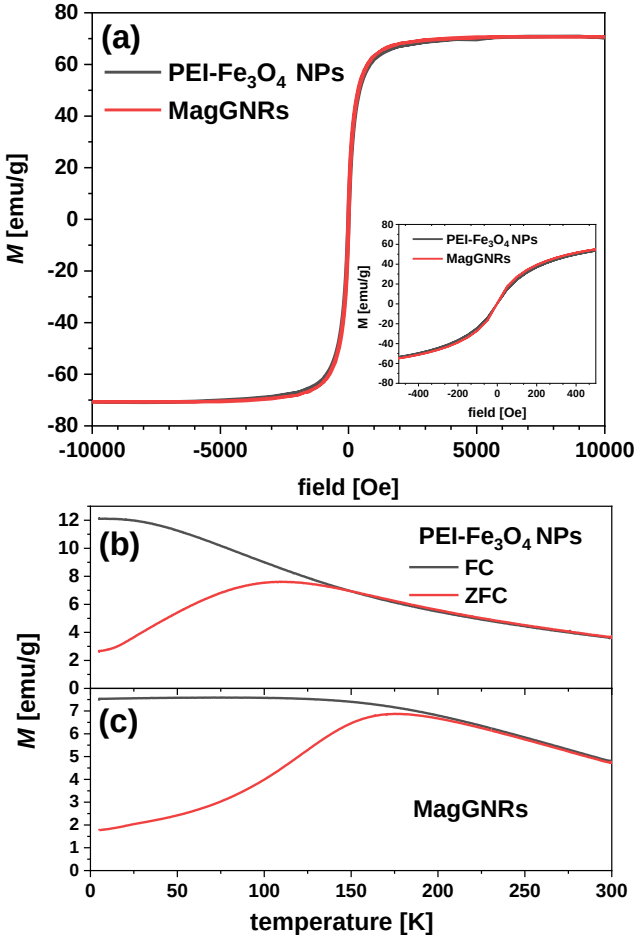

Figure 4.8. Magnetic characterization of PEI-Fe_3O_4 NPs and large MagGNRs in a PVA film. (a) M vs. H of PEI-Fe_3O_4 NPs and large MagGNRs at 300 K with inset showing the same plots magnified near the origin. Field cooled (FC) and zero field cooled (ZFC) measurements with a 10 Oe field of (b) PEI-Fe_3O_4 NPs and (c) large MagGNRs.

4.3. Conclusions

For the magnetic alignment of nanostructures coated with magnetic satellite NPs, what is the smallest size that can still sufficiently overcome Brownian motion and align? While the size and aspect ratio of the core nanorod and the size and composition of the magnetic satellite NPs collectively determine this limit, we have experimentally demonstrated a new lower limit by aligning MagGNRs with low aspect ratios. These findings have implications for the magnetic

alignment of all kinds of anisotropic nanostructures with magnetic satellite NPs. Large MagGNRs align well, while the small MagGNRs only give partial alignment. The underlying optical properties of the GNR cores are well preserved; GNRs that align in magnetic fields can be realized without degrading their optical properties. The multifunctionality of MagGNRs will be useful for several applications, including multimodal imaging and therapy, advanced (magneto-)optical materials based on the anisotropy and polarization effects of the plasmon, and magnetically modulated photothermal heating. Moreover, because the optical properties of the GNR cores are largely unchanged by the magnetic overcoating, MagGNRs will enable the further development of applications based on non-magnetic GNRs that take advantage of the additional capability to manipulate MagGNRs with magnetic fields.

The performance of MagGNRs is promising for further investigation and applications. MagGNRs respond to low magnetic fields; anisotropy in the optical properties is already evident at 20 Oe, and nearly the maximum alignment is already obtained in fields of 500 Oe. MagGNRs can track dynamic fields of at least 17 Hz in water. This work introduces a comprehensive framework for analyzing the alignment of MagGNRs from their polarized optical properties and structural characterization, which yields the energy barrier that allows MagGNRs to overcome Brownian motion and align with the field. The model can further aid the design and analysis of the alignment of other small anisotropic nanostructures in magnetic fields or other fields or matrices that impart alignment.

4.4. Experimental Section

Chemicals: $HAuCl_4 \cdot xH_2O$ (Alfa Aesar, 99.999%, where x was estimated as 3), cetyltrimethylammonium bromide (CTAB, Amresco, high purity), KBr (Alfa Aesar, ACS, 99% min), $AgNO_3$ (Alfa Aesar, 99.9995%), deionized water (Ricca, ACS Reagent grade, ASTM Type

I, ASTM Type II), ascorbic acid (AA, J.T. Baker, 99.5%), hydroquinone (Acros Organics, 99.5%), $NaBH_4$ (Sigma-Aldrich, 99%, 213462), NaOH (Sigma-Aldrich, 98%), BSA (Sigma-Aldrich, A7906, 98%), Na-citrate dihydrate (Mallinckrodt, 99% min), Fe(III) acetylacetonate (Strem, 99%), $FeCl_3$ (Alfa Aesar, anhydrous, 98%), Na oleate (TCI America, 97% min), oleic acid (Sigma-Aldrich, 90%), 1-octadecene (Sigma-Aldrich, 90%), benzyl ether (Acros Organics, 99%), oleylamine (Sigma Aldrich), hexanes (Macron, 95%), ethanol (Koptec, absolute, anhydrous), isopropanol (Macron, 99.5%), chloroform (OmniSolv, 99.9%), NaF (Alfa Aesar, 99.99%), 15-crown-5 ether (Ambeed, 98%), PEI (Alfa Aesar, branched, MW 10000, 99%), PVA (Alfa Aesar, 98-99% hydrolyzed, high molecular weight).

Permanent Magnets: 1" cube magnet (Diymag, N52), 10 mm cube magnets (Apex magnets, M10mmCU, N48), ¼" cube magnets (Bunting Magnetics, NEB38P252525, N38), circular Halbach array (Supermagnetman, HB0060, field strength ~1.8 kOe, N48).

Synthesis and Purification of CTAB-Stabilized GNRs: CTAB-GNRs were synthesized following a previously published seed-mediated approach.[68] A typical 1-L synthesis yields ~190 mg of CTAB-GNRs. The average dimensions of the GNR cores were 78 nm × 21 nm (aspect ratio of 3.7) with the longitudinal surface plasmon resonance (LSPR) peak extinction at 790 nm. Large CTAB-GNRs with average dimensions of 148 nm × 47 nm and peak LSPR extinction at 860 nm were also synthesized in two-step growth technique developed for this project. First, high-aspect ratio CTAB-GNRs with dimensions of 117 nm × 21 nm were synthesized using another method,[69] in which 6 mL of seed solution was added to 250 mL of growth solution (0.5 mM $HAuCl_4$, 100 mM M CTAB, 0.4 mM $AgNO_3$, and 5 mM hydroquinone) under gentle shaking and then aged for overnight. The seed solution was prepared by quickly injecting 0.6 mL of 10 mM $NaBH_4$ solution into 9.4 mL of 0.5 mM $HAuCl_4$ and 100 mM CTAB that was rapidly stirring and already

equilibrated in a water bath at 35 °C. Stirring was turned off 30 seconds after the injection, followed by aging for 25 min at 35 °C. For further growth into large CTAB-GNRs, 5 mL of the solution of as-prepared CTAB-GNRs was added to 20 mL of growth solution containing 91 mM CTAB, 0.93 mM $HAuCl_4$, 9.1 mM KBr, and 0.992 mM ascorbic acid. 1.1 mL of 15.76 mM ascorbic acid was injected into this mixture over a period of 18 hours with magnetic stirring at 35 °C. (As described, large excesses of small GNRs and of intermediate 117 nm × 21 nm CTAB-GNRs were synthesized, which allowed testing of multiple overgrowth reactions. In principle, these amounts could be scaled down.)

For both the small and large CTAB-GNRs, the concentration of CTAB before purification was ~100 mM. From each of the small and large CTAB-GNRs, a volume of 25 mL was purified in a single centrifuge tube. Both samples were purified in the same manner, three cycles of centrifugation (Thermo Scientific Sorvall Legend X1R with Fiberlite F15-6x100y rotor) at 10000 rpm (10956 *g*) for 20 min, which brought the final concentration of CTAB to ~1 mM. Between cycles of centrifugation, as much of the supernatant was carefully removed by pipette as possible, while avoiding perturbing the pellet of CTAB-GNRs. Water (after the first round of centrifugation) or 1 mM CTAB (after the second and third rounds of centrifugation) was added to redisperse the pellet and bring the total volume to 25 mL after the first and second rounds and 10 mL after the third round of centrifugation.

Functionalization with BSA: BSA-coated GNRs (BSA-GNRs) were obtained from both small and large CTAB-GNRs by complete replacement of CTAB with BSA according to a previously reported method.[71] 20 mL of concentrated BSA solution (10 mg/mL) was prepared by mixing BSA with deionized water containing 0.02 wt% Na citrate. The mixture was sonicated for 10 min. 10 mL of deionized water was then quickly added (without mixing) to 10 mL of the

purified CTAB-GNRs, which was then immediately transferred to the 20 mL BSA solution under sonication. Addition of the deionized water destabilizes the CTAB-GNRs and facilitates replacement of CTAB with BSA. The resulting 40 mL solution was sonicated for 30 min and then centrifuged at 9000 rpm (8875 *g*) for 20 min. To ensure good BSA functionalization, the product was functionalized with BSA again, using a solution of BSA that was pH adjusted to ~10, measured with a pH meter, as follows. 40 mg of BSA were dissolved in a mixture of 400 μL of 0.1 M NaOH and 39.6 mL of deionized water with 0.02 wt% Na citrate. The colorless supernatant was replaced with 40 mL of this 1 mg/mL BSA solution. The mixture was then sonicated for 5 min and kept at rest without stirring for 24 hours before purification. The product was purified by 4 cycles of centrifugation, where the supernatant was replaced each time with 24.5 mL of basic water (pH ~10.8, measured with a pH meter) that had been prepared by mixing 6 mL of 0.1 M NaOH in 194 mL deionized water. After purification, the BSA-GNRs were redispersed in 25 mL of the basic water.

Synthesis and Functionalization of Fe_3O_4 NPs with PEI: Oleylamine-stabilized magnetite (Fe_3O_4) NPs with an average diameter of 13.4 nm were synthesized in two steps. First, iron oleate precursor was prepared and thermally decomposed, yielding oleic acid-stabilized NPs by following established methods.[72,92] In the second step, the oleic acid shell was replaced with oleylamine. Iron oleate was prepared by dissolving 3.244 g of anhydrous $FeCl_3$ with 18.27 g of Na oleate in a mixture of 30 mL of water, 40 mL of ethanol and 70 mL of hexanes. The reaction was carried out by refluxing at 70 °C for 4 hours with magnetic stirring. After completing the reaction, the top organic layer containing Fe oleate was separated from the aqueous layer and washed 3 times with water. The Fe oleate product was then dried in a fume hood for two days, during which the hexanes evaporated. For synthesizing Fe_3O_4 NPs, 2.5 g of Fe oleate and 1.26 g of oleic acid

were dissolved in a mixture of 2.77 mL of benzyl ether and 5.55 mL of 1-octadecene in a three-necked round-bottomed flask and connected to a Schlenk line. The mixture was heated under vacuum to 60 °C for 30 min, followed by backfilling with nitrogen, then heating to 325 °C at a rate of 3.3 °C/minute, and refluxing for 30 min to complete the reaction. After cooling to room temperature, 2 mL of the product was washed by adding a mixture of 2 mL of hexanes and 6 mL of ethanol, followed by centrifugation. After discarding the supernatant, the pellet was redispersed in 2 mL of hexanes, followed by addition of 6 mL of ethanol and centrifugation. After repeating this step once, the final pellet was dispersed in 20 mL hexanes.

A host-guest-driven technique was followed to replace the oleic acid with oleylamine,[73] as follows. 14 mL of isopropanol was added to the 20 mL of the Fe_3O_4 NPs in hexanes, followed by adding 2 mL of deionized water, into which 100 mg of NaF and 0.45 mL of 15-crown-5 ether had been dissolved. The mixture was sonicated for 5 min and then kept at rest for two hours. As the oleic acid is stripped away, the Fe_3O_4 NPs agglomerate over time. The supernatant was discarded, and the product was successively washed with hexanes, isopropanol, water, and then ethanol. Each washing step was performed twice in ~10 mL of each solvent before proceeding to the next solvent. The NPs were sonicated in each new solvent for 10 min, centrifuged at 5000-8000 rpm (2739-7012 *g*) for 20 min, redispersed in the same solvent again, sonicated for 10 min, centrifuged, and then redispersed in the next solvent. After the final washing step in ethanol, 9.98 mL of chloroform was added to the sedimented Fe_3O_4 NPs, followed by adding 20 μL of oleylamine and sonicating for 2 min. Oleylamine quickly regrafts onto the Fe_3O_4 NPs and causes them to disperse well. This solution was used as a stock solution and had a concentration of 1.48 mg/mL of Fe_3O_4 NPs, measured by inductively coupled optical emission spectroscopy (ICP-OES).

For functionalization with PEI, 1 mL of the stock solution of oleylamine-stabilized Fe_3O_4 NPs was diluted with 9 mL of chloroform. 100 mg of PEI was dissolved in 30 mL of chloroform and added to the diluted Fe_3O_4 NPs under vigorous stirring. The mixture was then sonicated for 30 min, followed by stirring at 40 °C for 2 hours to complete PEI functionalization. The PEI-functionalized Fe_3O_4 (PEI-Fe_3O_4) NPs were there then transferred into water by adding 5 mL of water and shaking by hand for ~1 min, until the brown color of the PEI-Fe_3O_4 NPs is visible in the top aqueous layer. The aqueous layer was then extracted and washed 5 times with deionized water to remove excess PEI molecules. In each washing cycle, PEI-Fe_3O_4 NPs were purified using a centrifuge filter (Amicon Ultra, 100 kDa) at 3500 rpm (1342 *g*) for 30 min. The purified PEI-Fe_3O_4 NPs were dispersed in 2.5 mL of deionized water.

Assembly of MagGNRs: 0.5 mL of BSA-GNRs (~0.19 mg/mL, based on the extinction at 400 nm of 0.38 after 6× dilution) was added quickly to 0.5 mL of the purified PEI-Fe_3O_4 NPs (~0.6 mg/mL, based on effective 2.5× dilution of the above stock solution) under vigorous stirring (800 rpm) for 5 min. The mixture has pH of ~10.6. The stirring rate was then decreased to 100 rpm for 2 hours to complete the assembly MagGNRs. Three cycles of centrifugation (Eppendorf 5415C Centrifuge, 5000 rpm (2152 *g*) for smaller MagGNRs and 2000 rpm (344 *g*) for larger MagGNRs) for 10 min were performed to separate MagGNRs from excess PEI-Fe_3O_4 NPs, where as much supernatant was removed as possible, and the product was redispersed in 1 mL of deionized water at the end of each cycle.

Transmission Electron Microscopy (TEM): TEM images were acquired on a FEI Talos F200X G2 at an operating voltage of 200 kV. Samples were prepared by drop casting onto a carbon-coated Cu TEM grid. For investigating magnetic alignment of MagGNRs, the TEM grid was placed between the poles (10 cm diameter) of a GMW 3472-70 electromagnet, and drying

occurred in a magnetic field of 10 kOe. Analysis of 200 MagGNRs provided their average sizes and angular orientation distribution.

Optical Extinction Spectroscopy: Optical extinction spectra were acquired using an Ocean Optics Red Tide USB650 spectrometer with a glass cuvette having a 1 cm path length. Polarized extinction was measured by placing piece of a polarizer film (Thorlabs, LPNIRE2X2) in the beam path before the sample. For polarized extinction spectroscopy in applied magnetic fields, the spectrophotometer was placed between the poles of the electromagnet (Supporting Information, Figure S5), and polarizer films were inserted with their polarization axis either parallel (0°) or perpendicular (90°) to the magnetic field direction. To observe the effects of intermediate polarization angles between 0° and 90°, a single polarizer film was inserted next to the cuvette, and a permanent magnet was held at different angles with respect to the polarization direction (Figure 4.4d).

Small Angle X-ray Scattering: SAXS measurements were performed on a Ganesha 300 XL+ (SAXSLAB) instrument with a focused X-ray beam from a Cu K_α source, giving λ = 0.154 nm. Scattered X-rays were recorded using a pixel detector (PILATUS 300 K) at a sample-detector distance of 1510 mm, enabling measurements down to q_{min} = ~0.035 nm^{-1}. A glass capillary containing an aqueous dispersion of MagGNRs with extinction of ~1 at the LSPR peak was oriented vertically along the *y*-direction was sandwiched between two permanent magnets creating a quasi-homogeneous magnetic field oriented along the *x*-direction. A field of ~2 kOe was generated by two cylindrical permanent NdFeB magnets (Supermagnete S-13-02-N, N45) with a diameter of 13 mm and a height of 2 mm, separated by a gap of 5 mm using a polytetrafluoroethylene ring as a spacer. The orientation of MagGNRs can be defined with the polar angle θ between the long axis of the nanorod and the magnetic field direction (*x*-axis), and

the projected angle χ in the *xy*-plane (Figure 4.1). The X-ray beam propagated in *z*-direction, and the detector is in the *xy*-plane. Measurements were carried out in aqueous dispersions for 10 min. The solvent background was subtracted from the scattering patterns.

Magnetometry: PEI-Fe_3O_4 NPs and MagGNRs were dispersed in PVA films for magnetic characterization using a Quantum Design MPMS 3 superconducting quantum interference device vibrating sample magnetometer. Samples were prepared by dissolving 200 mg of PVA in 1 mL of water, followed by adding 0.01 mL of aqueous PEI-Fe_3O_4 NPs or MagGNRs, casting in a polytetrafluoroethylene mold, and allowing the water to evaporate overnight at 50 °C.

Statistical Analysis: TEM images are presented without contrast or brightness adjustment. Measurements of the dimensions and angular distributions of GNRs in TEM images were performed using ImageJ and were averaged over 200 GNRs. Optical extinction spectra are presented without smoothing. Statistical methods for analysis of SAXS measurements are described in the Results and Discussion. The SAXS data were processed using Matlab R2017b.

4.5. Acknowledgements

We acknowledge Michael Göbel for performing the SAXS measurements and Benjamin A. Evans and O. Thompson Mefford for helpful discussions. This research was supported by the National Science Foundation (CMMI-1763025 and CBET-1803830), Alexander von Humboldt Foundation, Deutsche Forschungsgemeinschaft (DFG, German Research Foundation) - GRK 2767 - Projektnummer 451785257, and by the Fonds der Chemischen Industrie (Liebig fellowship to C.R.). We acknowledge the Free State of Saxony and TU Dresden for financial support of the Dresden Center for Intelligent Materials (DCIM). This work was performed in part at the Analytical Instrumentation Facility (AIF) at North Carolina State University, which is supported by the State of North Carolina and the National Science Foundation (ECCS-2025064). The AIF is

a member of the North Carolina Research Triangle Nanotechnology Network (RTNN), a site in the National Nanotechnology Coordinated Infrastructure (NNCI).

4.6. References

(1) Liz-Marzán, L. M. Tailoring Surface Plasmons through the Morphology and Assembly of Metal Nanoparticles. *Langmuir* **2006**, *22*, 32-41.

(2) Huang, X.; El-Sayed, I. H.; Qian, W.; El-Sayed, M. A. Cancer Cell Imaging and Photothermal Therapy in the Near-Infrared Region by Using Gold Nanorods. *J. Am. Chem. Soc.* **2006**, *128*, 2115-2120.

(3) Tong, L.; Wei, Q.; Wei, A.; Cheng, J.-X. Gold Nanorods as Contrast Agents for Biological Imaging: Optical Properties, Surface Conjugation and Photothermal Effects†. *Photochem. Photobiol.* **2009**, *85*, 21-32.

(4) Chhetri, R. K.; Blackmon, R. L.; Wu, W.-C.; Hill, D. B.; Button, B.; Casbas-Hernandez, P.; Troester, M. A.; Tracy, J. B.; Oldenburg, A. L. Probing biological nanotopology via diffusion of weakly constrained plasmonic nanorods with optical coherence tomography. *Proc. Natl. Acad. Sci. U. S. A.* **2014**, *111*, E4289-E4297.

(5) Ali, M. R. K.; Wu, Y.; Han, T.; Zang, X.; Xiao, H.; Tang, Y.; Wu, R.; Fernández, F. M.; El-Sayed, M. A. Simultaneous Time-Dependent Surface-Enhanced Raman Spectroscopy, Metabolomics, and Proteomics Reveal Cancer Cell Death Mechanisms Associated with Gold Nanorod Photothermal Therapy. *J. Am. Chem. Soc.* **2016**, *138*, 15434-15442.

(6) Pastoriza-Santos, I.; Kinnear, C.; Pérez-Juste, J.; Mulvaney, P.; Liz-Marzán, L. M. Plasmonic polymer nanocomposites. *Nat. Rev. Mater.* **2018**, *3*, 375-391.

(7) Zeng, J.; Zhang, Y.; Zeng, T.; Aleisa, R.; Qiu, Z.; Chen, Y.; Huang, J.; Wang, D.; Yan, Z.; Yin, Y. Anisotropic plasmonic nanostructures for colorimetric sensing. *Nano Today* **2020**, *32*, 100855.

(8) Lu, J.; Xue, Y.; Bernardino, K.; Zhang, N.-N.; Gomes, W. R.; Ramesar, N. S.; Liu, S.; Hu, Z.; Sun, T.; Moura, A. F. d.; Kotov, N. A.; Liu, K. Enhanced optical asymmetry in supramolecular chiroplasmonic assemblies with long-range order. *Science* **2021**, *371*, 1368-1374.

(9) Nikoobakht, B.; El-Sayed, M. A. Preparation and Growth Mechanism of Gold Nanorods (NRs) Using Seed-Mediated Growth Method. *Chem. Mater.* **2003**, *15*, 1957-1962.

(10) Murphy, C. J.; Sau, T. K.; Gole, A. M.; Orendorff, C. J.; Gao, J.; Gou, L.; Hunyadi, S. E.; Li, T. Anisotropic Metal Nanoparticles: Synthesis, Assembly, and Optical Applications. *J. Phys. Chem. B* **2005**, *109*, 13857-13870.

(11) Wei, W.; Bai, F.; Fan, H. Oriented Gold Nanorod Arrays: Self-Assembly and Optoelectronic Applications. *Angew. Chem., Int. Ed.* **2019**, *58*, 11956-11966.

(12) Pérez-Juste, J.; Rodríguez-González, B.; Mulvaney, P.; Liz-Marzán, L. M. Optical Control and Patterning of Gold-Nanorod–Poly(vinyl alcohol) Nanocomposite Films. *Adv. Funct. Mater.* **2005**, *15*, 1065-1071.

(13) Murphy, C. J.; Orendorff, C. J. Alignment of Gold Nanorods in Polymer Composites and on Polymer Surfaces. *Adv. Mater.* **2005**, *17*, 2173-2177.

(14) Li, J.; Liu, S.; Liu, Y.; Zhou, F.; Li, Z.-Y. Anisotropic and enhanced absorptive nonlinearities in a macroscopic film induced by aligned gold nanorods. *Appl. Phys. Lett.* **2010**, *96*, 263103.

(15) Roskov, K. E.; Kozek, K. A.; Wu, W.-C.; Chhetri, R. K.; Oldenburg, A. L.; Spontak, R. J.; Tracy, J. B. Long-Range Alignment of Gold Nanorods in Electrospun Polymer Nano/Microfibers. *Langmuir* **2011**, *27*, 13965-13969.

(16) Zhang, H.; Hu, Z.; Ma, Z.; Gecevičius, M.; Dong, G.; Zhou, S.; Qiu, J. Anisotropically Enhanced Nonlinear Optical Properties of Ensembles of Gold Nanorods Electrospun in Polymer Nanofiber Film. *ACS Appl. Mater. Interfaces* **2016**, *8*, 2048-2053.

(17) Li, P.; Li, Y.; Zhou, Z.-K.; Tang, S.; Yu, X.-F.; Xiao, S.; Wu, Z.; Xiao, Q.; Zhao, Y.; Wang, H.; Chu, P. K. Evaporative Self-Assembly of Gold Nanorods into Macroscopic 3D Plasmonic Superlattice Arrays. *Adv. Mater.* **2016**, *28*, 2511-2517.

(18) Wei, W.; Wang, Y.; Ji, J.; Zuo, S.; Li, W.; Bai, F.; Fan, H. Fabrication of Large-Area Arrays of Vertically Aligned Gold Nanorods. *Nano Lett.* **2018**, *18*, 4467-4472.

(19) Correa-Duarte, M. A.; Sobal, N.; Liz-Marzán, L. M.; Giersig, M. Linear Assemblies of Silica-Coated Gold Nanoparticles Using Carbon Nanotubes as Templates. *Adv. Mater.* **2004**, *16*, 2179-2184.

(20) Nepal, D.; Onses, M. S.; Park, K.; Jespersen, M.; Thode, C. J.; Nealey, P. F.; Vaia, R. A. Control over Position, Orientation, and Spacing of Arrays of Gold Nanorods Using Chemically Nanopatterned Surfaces and Tailored Particle–Particle–Surface Interactions. *ACS Nano* **2012**, *6*, 5693-5701.

(21) Nakamura, S.; Mitomo, H.; Sekizawa, Y.; Higuchi, T.; Matsuo, Y.; Jinnai, H.; Ijiro, K. Strategy for Finely Aligned Gold Nanorod Arrays Using Polymer Brushes as a Template. *Langmuir* **2020**, *36*, 3590-3599.

(22) Zhang, H.; Liu, Y.; Shahidan, M. F. S.; Kinnear, C.; Maasoumi, F.; Cadusch, J.; Akinoglu, E. M.; James, T. D.; Widmer-Cooper, A.; Roberts, A.; Mulvaney, P. Direct Assembly of Vertically Oriented, Gold Nanorod Arrays. *Adv. Funct. Mater.* **2021**, *31*, 2006753.

(23) Li, F.; Wang, K.; Deng, N.; Xu, J.; Yi, M.; Xiong, B.; Zhu, J. Self-Assembly of Polymer End-Tethered Gold Nanorods into Two-Dimensional Arrays with Tunable Tilt Structures. *ACS Appl. Mater. Interfaces* **2021**, *13*, 6566-6574.

(24) Tebbe, M.; Mayer, M.; Glatz, B. A.; Hanske, C.; Probst, P. T.; Müller, M. B.; Karg, M.; Chanana, M.; König, T. A. F.; Kuttner, C.; Fery, A. Optically anisotropic substrates via wrinkle-assisted convective assembly of gold nanorods on macroscopic areas. *Faraday Discuss.* **2015**, *181*, 243-260.

(25) Cha, Y. J.; Kim, D. S.; Yoon, D. K. Highly Aligned Plasmonic Gold Nanorods in a DNA Matrix. *Adv. Funct. Mater.* **2017**, *27*, 1703790.

(26) Liu, Q.; Cui, Y.; Gardner, D.; Li, X.; He, S.; Smalyukh, I. I. Self-Alignment of Plasmonic Gold Nanorods in Reconfigurable Anisotropic Fluids for Tunable Bulk Metamaterial Applications. *Nano Lett.* **2010**, *10*, 1347-1353.

(27) Thomas, M. R.; Klein, S.; Greasty, R. J.; Mann, S.; Perriman, A. W.; Richardson, R. M. Nematic Director-Induced Switching of Assemblies of Hexagonally Packed Gold Nanorods. *Adv. Mater.* **2012**, *24*, 4424-4429.

(28) Umadevi, S.; Feng, X.; Hegmann, T. Large Area Self-Assembly of Nematic Liquid-Crystal-Functionalized Gold Nanorods. *Adv. Funct. Mater.* **2013**, *23*, 1393-1403.

(29) Liu, Q.; Campbell, M. G.; Evans, J. S.; Smalyukh, I. I. Orientationally Ordered Colloidal Co-Dispersions of Gold Nanorods and Cellulose Nanocrystals. *Adv. Mater.* **2014**, *26*, 7178-7184.

(30) Zhang, Y.; Liu, Q.; Mundoor, H.; Yuan, Y.; Smalyukh, I. I. Metal Nanoparticle Dispersion, Alignment, and Assembly in Nematic Liquid Crystals for Applications in Switchable Plasmonic Color Filters and E-Polarizers. *ACS Nano* **2015**, *9*, 3097-3108.

(31) Liu, X.; Qi, G.; Park, A. M. G.; Rodriguez-Gonzalez, A.; Enotiadis, A.; Pan, W.; Kosma, V.; Fuchs, G. D.; Kirby, B. J.; Giannelis, E. P. Scalable Synthesis of Switchable Assemblies of Gold Nanorod Lyotropic Liquid Crystal Nanocomposites. *Small* **2019**, *15*, 1901666.

(32) van der Zande, B. M. I.; Koper, G. J. M.; Lekkerkerker, H. N. W. Alignment of Rod-Shaped Gold Particles by Electric Fields. *J. Phys. Chem. B* **1999**, *103*, 5754-5760.

(33) Ahmed, W.; Kooij, E. S.; van Silfhout, A.; Poelsema, B. Quantitative Analysis of Gold Nanorod Alignment after Electric Field-Assisted Deposition. *Nano Lett.* **2009**, *9*, 3786-3794.

(34) Fontana, J.; da Costa, G. K. B.; Pereira, J. M.; Naciri, J.; Ratna, B. R.; Palffy-Muhoray, P.; Carvalho, I. C. S. Electric field induced orientational order of gold nanorods in dilute organic suspensions. *Appl. Phys. Lett.* **2016**, *108*, 081904.

(35) Greybush, N. J.; Charipar, K.; Geldmeier, J. A.; Bauman, S. J.; Johns, P.; Naciri, J.; Charipar, N.; Park, K.; Vaia, R. A.; Fontana, J. Dynamic Plasmonic Pixels. *ACS Nano* **2019**, *13*, 3875-3883.

(36) Fukagawa, T.; Tajima, R.; Yamaguchi, Y.; Tanaka, H.; Morikawa, K.; Tanaka, S.; Hatakeyama, Y.; Hino, K. Effect of an External DC Electric Field on the Order of Polymer-Capped Gold Nanorods: Formation of Smectic, Tetragonal, and Hexagonal Structures. *J. Phys. Chem. C* **2021**, *125*, 11085-11096.

(37) Ruijgrok, P. V.; Verhart, N. R.; Zijlstra, P.; Tchebotareva, A. L.; Orrit, M. Brownian Fluctuations and Heating of an Optically Aligned Gold Nanorod. *Phys. Rev. Lett.* **2011**, *107*, 037401.

(38) He, L.; Wang, M.; Ge, J.; Yin, Y. Magnetic Assembly Route to Colloidal Responsive Photonic Nanostructures. *Acc. Chem. Res.* **2012**, *45*, 1431-1440.

(39) Wang, M.; Yin, Y. Magnetically Responsive Nanostructures with Tunable Optical Properties. *J. Am. Chem. Soc.* **2016**, *138*, 6315-6323.

(40) Hurst, S. J.; Payne, E. K.; Qin, L.; Mirkin, C. A. Multisegmented One-Dimensional Nanorods Prepared by Hard-Template Synthetic Methods. *Angew. Chem., Int. Ed.* **2006**, *45*, 2672-2692.

(41) Oh, B.-K.; Park, S.; Millstone, J. E.; Lee, S. W.; Lee, K.-B.; Mirkin, C. A. Separation of Tricomponent Protein Mixtures with Triblock Nanorods. *J. Am. Chem. Soc.* **2006**, *128*, 11825-11829.

(42) Gupta, M. K.; König, T.; Near, R.; Nepal, D.; Drummy, L. F.; Biswas, S.; Naik, S.; Vaia, R. A.; El-Sayed, M. A.; Tsukruk, V. V. Surface Assembly and Plasmonic Properties in Strongly Coupled Segmented Gold Nanorods. *Small* **2013**, *9*, 2979-2990.

(43) Kim, K.; Xu, X.; Guo, J.; Fan, D. L. Ultrahigh-speed rotating nanoelectromechanical system devices assembled from nanoscale building blocks. *Nat. Commun.* **2014**, *5*, 3632.

(44) Jung, I.; Jang, H.-J.; Han, S.; Acapulco, J. A. I.; Park, S. Magnetic Modulation of Surface Plasmon Resonance by Tailoring Magnetically Responsive Metallic Block in Multisegment Nanorods. *Chem. Mater.* **2015**, *27*, 8433-8441.

(45) Jung, I.; Yoo, H.; Jang, H.-J.; Cho, S.; Lee, K.; Hong, S.; Park, S. Fourier Transform Surface Plasmon Resonance (FTSPR) with Gyromagnetic Plasmonic Nanorods. *Angew. Chem., Int. Ed.* **2018**, *57*, 1841-1845.

(46) Wang, X.; Feng, J.; Yu, H.; Jin, Y.; Davidson, A.; Li, Z.; Yin, Y. Anisotropically Shaped Magnetic/Plasmonic Nanocomposites for Information Encryption and Magnetic-Field-Direction Sensing. *Research* **2018**, *2018*, 7527825.

(47) Wang, M.; Gao, C.; He, L.; Lu, Q.; Zhang, J.; Tang, C.; Zorba, S.; Yin, Y. Magnetic Tuning of Plasmonic Excitation of Gold Nanorods. *J. Am. Chem. Soc.* **2013**, *135*, 15302-15305.

(48) Li, Z.; Jin, J.; Yang, F.; Song, N.; Yin, Y. Coupling magnetic and plasmonic anisotropy in hybrid nanorods for mechanochromic responses. *Nat. Commun.* **2020**, *11*, 2883.

(49) Wang, C.; Chen, J.; Talavage, T.; Irudayaraj, J. Gold Nanorod/Fe3O4 Nanoparticle "Nano-Pearl-Necklaces" for Simultaneous Targeting, Dual-Mode Imaging, and Photothermal Ablation of Cancer Cells. *Angew. Chem., Int. Ed.* **2009**, *48*, 2759-2763.

(50) Huang, L.; Ao, L.; Hu, D.; Wang, W.; Sheng, Z.; Su, W. Magneto-Plasmonic Nanocapsules for Multimodal-Imaging and Magnetically Guided Combination Cancer Therapy. *Chem. Mater.* **2016**, *28*, 5896-5904.

(51) Li, Z.; Yin, Y. Stimuli-Responsive Optical Nanomaterials. *Adv. Mater.* **2019**, *31*, 1807061.

(52) Li, Z.; Ye, Z.; Han, L.; Fan, Q.; Wu, C.; Ding, D.; Xin, H. L.; Myung, N. V.; Yin, Y. Polarization-Modulated Multidirectional Photothermal Actuators. *Adv. Mater.* **2021**, *33*, 2006367.

(53) Wei, Q.; Song, H.-M.; Leonov, A. P.; Hale, J. A.; Oh, D.; Ong, Q. K.; Ritchie, K.; Wei, A. Gyromagnetic Imaging: Dynamic Optical Contrast Using Gold Nanostars with Magnetic Cores. *J. Am. Chem. Soc.* **2009**, *131*, 9728-9734.

(54) Erb, R. M.; Libanori, R.; Rothfuchs, N.; Studart, A. R. Composites Reinforced in Three Dimensions by Using Low Magnetic Fields. *Science* **2012**, *335*, 199-204.

(55) Chen, X.; Ye, Z.; Yang, F.; Feng, J.; Li, Z.; Huang, C.; Ke, Q.; Yin, Y. Magnetic cellulose microcrystals with tunable magneto-optical responses. *Appl. Mater. Today* **2020**, *20*, 100749.

(56) Yan, M.; Fresnais, J.; Berret, J. F. Growth mechanism of nanostructured superparamagnetic rods obtained by electrostatic co-assembly. *Soft Matter* **2010**, *6*, 1997-2005.

(57) Townsend, J.; Burtovyy, R.; Aprelev, P.; Kornev, K. G.; Luzinov, I. Enhancing Mechanical and Thermal Properties of Epoxy Nanocomposites via Alignment of Magnetized SiC Whiskers. *ACS Appl. Mater. Interfaces* **2017**, *9*, 22927-22940.

(58) Chen, Z.; Townsend, J.; Aprelev, P.; Gu, Y.; Burtovyy, R.; Luzinov, I.; Kornev, K. G.; Peng, F. Magnetic Submicron Mullite Coatings with Oriented SiC Whiskers. *ACS Appl. Mater. Interfaces* **2018**, *10*, 11907-11919.

(59) Yuan, J.; Gao, H.; Schacher, F.; Xu, Y.; Richter, R.; Tremel, W.; Müller, A. H. E. Alignment of Tellurium Nanorods via a Magnetization−Alignment− Demagnetization ("MAD") Process Assisted by an External Magnetic Field. *ACS Nano* **2009**, *3*, 1441-1450.

(60) Llerena Zambrano, B.; Forró, C.; Poloni, E.; Hennig, R.; Sivananthaguru, P.; Renz, A. F.; Studart, A. R.; Vörös, J. Magnetic Manipulation of Nanowires for Engineered Stretchable Electronics. *ACS Nano* **2022**, *16*, 837-846.

(61) Correa-Duarte, M. A.; Grzelczak, M.; Salgueiriño-Maceira, V.; Giersig, M.; Liz-Marzán, L. M.; Farle, M.; Sierazdki, K.; Diaz, R. Alignment of Carbon Nanotubes under Low Magnetic Fields through Attachment of Magnetic Nanoparticles. *J. Phys. Chem. B* **2005**, *109*, 19060-19063.

(62) Zhang, M.; Magagnosc, D. J.; Liberal, I.; Yu, Y.; Yun, H.; Yang, H.; Wu, Y.; Guo, J.; Chen, W.; Shin, Y. J.; Stein, A.; Kikkawa, J. M.; Engheta, N.; Gianola, D. S.; Murray, C. B.; Kagan, C. R. High-strength magnetically switchable plasmonic nanorods assembled from a binary nanocrystal mixture. *Nat. Nanotechnol.* **2017**, *12*, 228-232.

(63) Mishra, S. R.; Dickey, M. D.; Velev, O. D.; Tracy, J. B. Selective and directional actuation of elastomer films using chained magnetic nanoparticles. *Nanoscale* **2016**, *8*, 1309-1313.

(64) Erb, R. M.; Martin, J. J.; Soheilian, R.; Pan, C.; Barber, J. R. Actuating Soft Matter with Magnetic Torque. *Adv. Funct. Mater.* **2016**, *26*, 3859-3880.

(65) Chapman, B. S.; Wu, W.-C.; Li, Q.; Holten-Andersen, N.; Tracy, J. B. Heteroaggregation Approach for Depositing Magnetite Nanoparticles onto Silica-Overcoated Gold Nanorods. *Chem. Mater.* **2017**, *29*, 10362-10368.

(66) Chen, H.; Shao, L.; Li, Q.; Wang, J. Gold nanorods and their plasmonic properties. *Chem. Soc. Rev.* **2013**, *42*, 2679-2724.

(67) Ge, J.; Hu, Y.; Biasini, M.; Beyermann, W. P.; Yin, Y. Superparamagnetic Magnetite Colloidal Nanocrystal Clusters. *Angew. Chem., Int. Ed.* **2007**, *46*, 4342-4345.

(68) Kozek, K. A.; Kozek, K. M.; Wu, W.-C.; Mishra, S. R.; Tracy, J. B. Large-Scale Synthesis of Gold Nanorods through Continuous Secondary Growth. *Chem. Mater.* **2013**, *25*, 4537-4544.

(69) Vigderman, L.; Zubarev, E. R. High-Yield Synthesis of Gold Nanorods with Longitudinal SPR Peak Greater than 1200 nm Using Hydroquinone as a Reducing Agent. *Chem. Mater.* **2013**, *25*, 1450-1457.

(70) Khlebtsov, B. N.; Khanadeev, V. A.; Ye, J.; Sukhorukov, G. B.; Khlebtsov, N. G. Overgrowth of Gold Nanorods by Using a Binary Surfactant Mixture. *Langmuir* **2014**, *30*, 1696-1703.

(71) Tebbe, M.; Kuttner, C.; Männel, M.; Fery, A.; Chanana, M. Colloidally Stable and Surfactant-Free Protein-Coated Gold Nanorods in Biological Media. *ACS Appl. Mater. Interfaces* **2015**, *7*, 5984-5991.

(72) Chen, R.; Christiansen, M. G.; Sourakov, A.; Mohr, A.; Matsumoto, Y.; Okada, S.; Jasanoff, A.; Anikeeva, P. High-Performance Ferrite Nanoparticles through Nonaqueous Redox Phase Tuning. *Nano Lett.* **2016**, *16*, 1345-1351.

(73) Shirmardi Shaghasemi, B.; Dehghani, E. S.; Benetti, E. M.; Reimhult, E. Host–guest driven ligand replacement on monodisperse inorganic nanoparticles. *Nanoscale* **2017**, *9*, 8925-8929.

(74) Stoner, E. C.; Wohlfarth, E. P. A mechanism of magnetic hysteresis in heterogeneous alloys. *IEEE Trans. Magn.* **1991**, *27*, 3475-3518.

(75) O'Konski, C. T.; Yoshioka, K.; Orttung, W. H. Electric Properties of Macromolecules. IV. Determination of Electric and Optical Parameters from Saturation of Electric Birefringence in Solutions. *J. Phys. Chem.* **1959**, *63*, 1558-1565.

(76) Maier, W.; Saupe, A. Eine einfache molekular-statistische Theorie der nematischen kristallinflüssigen Phase. Teil l1. *Z. Naturforsch. A* **1959**, *14*, 882-889.

(77) Maier, W.; Saupe, A. Eine einfache molekular-statistische Theorie der nematischen kristallinflüssigen Phase. Teil II. *Z. Naturforsch. A* **1960**, *15*, 287-292.

(78) Lemaire, B. J.; Davidson, P.; Ferré, J.; Jamet, J. P.; Petermann, D.; Panine, P.; Dozov, I.; Jolivet, J. P. Physical properties of aqueous suspensions of goethite (alpha-FeOOH) nanorods. *Eur. Phys. J. E* **2004**, *13*, 291-308.

(79) Hu, Z.; Fischbein, M. D.; Querner, C.; Drndić, M. Electric-Field-Driven Accumulation and Alignment of CdSe and CdTe Nanorods in Nanoscale Devices. *Nano Lett.* **2006**, *6*, 2585-2591.

(80) Ahmad, I.; Jansen, H. P.; Zandvliet, H. J. W.; Kooij, E. S. Hydrodynamic confinement and capillary alignment of gold nanorods. *Nanotechnology* **2015**, *27*, 025301.

(81) Butter, K.; Bomans, P. H. H.; Frederik, P. M.; Vroege, G. J.; Philipse, A. P. Direct observation of dipolar chains in iron ferrofluids by cryogenic electron microscopy. *Nat. Mater.* **2003**, *2*, 88-91.

(82) Krommenhoek, P. J.; Tracy, J. B. Magnetic Field-Directed Self-Assembly of Magnetic Nanoparticle Chains in Bulk Polymers. *Part. Part. Syst. Charact.* **2013**, *30*, 759-763.

(83) Tracy, J. B.; Crawford, T. M. Magnetic field-directed self-assembly of magnetic nanoparticles. *MRS Bull.* **2013**, *38*, 915-920.

(84) Yokoyama, D.; Sakaguchi, A.; Suzuki, M.; Adachi, C. Horizontal molecular orientation in vacuum-deposited organic amorphous films of hole and electron transport materials. *Appl. Phys. Lett.* **2008**, *93*, 173302.

(85) Yokoyama, D.; Setoguchi, Y.; Sakaguchi, A.; Suzuki, M.; Adachi, C. Orientation Control of Linear-Shaped Molecules in Vacuum-Deposited Organic Amorphous Films and Its Effect on Carrier Mobilities. *Adv. Funct. Mater.* **2010**, *20*, 386-391.

(86) Glor, E. C.; Ferrier, R. C.; Li, C.; Composto, R. J.; Fakhraai, Z. Out-of-plane orientation alignment and reorientation dynamics of gold nanorods in polymer nanocomposite films. *Soft Matter* **2017**, *13*, 2207-2215.

(87) van Rhee, P. G.; Zijlstra, P.; Verhagen, T. G. A.; Aarts, J.; Katsnelson, M. I.; Maan, J. C.; Orrit, M.; Christianen, P. C. M. Giant Magnetic Susceptibility of Gold Nanorods Detected by Magnetic Alignment. *Phys. Rev. Lett.* **2013**, *111*, 127202.

(88) Rosén, T.; Brouzet, C.; Roth, S. V.; Lundell, F.; Söderberg, L. D. Three-Dimensional Orientation of Nanofibrils in Axially Symmetric Systems Using Small-Angle X-ray Scattering. *J. Phys. Chem. C* **2018**, *122*, 6889-6899.

(89) Feng, S.; Xiong, X.; Zhang, G.; Xia, N.; Chen, Y.; Wang, W. Hierarchical Structure in Oriented Fibers of a Dendronized Polymer. *Macromolecules* **2009**, *42*, 281-287.

(90) Frankamp, B. L.; Boal, A. K.; Tuominen, M. T.; Rotello, V. M. Direct Control of the Magnetic Interaction between Iron Oxide Nanoparticles through Dendrimer-Mediated Self-Assembly. *J. Am. Chem. Soc.* **2005**, *127*, 9731-9735.

(91) Fabris, F.; Tu, K.-H.; Ross, C. A.; Nunes, W. C. Influence of dipolar interactions on the magnetic properties of superparamagnetic particle systems. *J. Appl. Phys.* **2019**, *126*, 173905.

(92) Park, J.; An, K.; Hwang, Y.; Park, J.-G.; Noh, H.-J.; Kim, J.-Y.; Park, J.-H.; Hwang, N.-M.; Hyeon, T. Ultra-large-scale syntheses of monodisperse nanocrystals. *Nat. Mater.* **2004**, *3*, 891-895.

4.7. Supporting Information

Magnetic Alignment for Plasmonic Control of Gold Nanorods Coated with Iron Oxide Nanoparticles

*Mehedi H. Rizvi, Ruosong Wang, Jonas Schubert, William D. Crumpler, Christian Rossner, Amy L. Oldenburg, Andreas Fery, and Joseph B. Tracy**

Supporting Movies:

Movie S1 (.mp4 format). Polarization effect on MagGNRs using single 1-inch cube magnet

Movie S2 (.mp4 format). Polarization effect on MagGNRs using circular Halbach array

Movie S3 (.mp4 format). Polarization effect on MagGNRs using two arrays of five ¼-inch cube magnets

Movie S4 (.mp4 format). Polarization effect on MagGNRs using single array of five ¼-inch cube magnets

Movie S5 (.mp4 format). Polarization effect on MagGNRs using two arrays of two 10-mm cube magnets

Movie S6 (.mp4 format). Polarization effect on MagGNRs using two 10-mm cube magnets

Movie S7 (.mp4 format). Magnetic separation of MagGNRs using two arrays of two 10-mm cube magnets

Movie S8 (.mp4 format). Polarization effect on MagGNRs on a magnetic stir plate at 60 rpm

Movie S9 (.mp4 format). Oscillating colors of MagGNRs on a magnetic stir plate at speeds up to 1000 rpm

Model for Quantifying Magnetic Alignment and Estimating $U_{barrier}$

MagGNRs consist of a GNR core coated with highly monodisperse superparamagnetic NPs. Application of an external magnetic field H induces a magnetic moment m in each NP, which is assumed to be identical and parallel to H. We attribute magnetic alignment of MagGNRs to a potential energy difference $U_{barrier}$ between states with m aligned parallel versus perpendicular to the long axis of the GNR core (Equation 3). This approach mimics the treatment of GNRs in an optical trap, where the energy difference between parallel and perpendicular orientations relative to the polarization of an electromagnetic field is modeled.[1] The distinction here is that magnetic interactions are responsible for the trapping behavior.

We model the magnetic potential energy of a MagGNR, U_{MagGNR}, which we assume is dominated by magnetic dipole-dipole interactions between each pair of NPs on the MagGNR, i.e., U_{MagGNR} is the sum of the energies needed to bring each NP of moment m in one-by-one from infinity to its position on the MagGNR. This can be done by tabulating the dipole-dipole interaction energy U_{ij} between each new NP, *j*, with each existing NP, *i*, already placed:

$$U_{MagGNR} = \sum_{j} \sum_{i>j} U_{ij} \,, \tag{S1}$$

where the dipole-dipole interaction energy is:

$$U_{ij} = \frac{\mu_0}{4\pi \left|\mathbf{r}_{ij}\right|^3} \left(\vec{\mathbf{m}}_i \cdot \vec{\mathbf{m}}_j - 3\left(\vec{\mathbf{m}}_i \cdot \hat{\mathbf{r}}_{ij}\right)\left(\vec{\mathbf{m}}_j \cdot \hat{\mathbf{r}}_{ij}\right)\right), \tag{S2}$$

r_{ij} is the displacement vector between the centers of NPs *i* and *j*, and μ_0 is the permeability of free space. For superparamagnetic NPs, the time-averaged moment will point parallel to H, and its strength will depend on H. Given that the moments are identical, $m_i = m_j = m$, the above simplifies to:

$$U_{ij} = \frac{\mu_0 |\mathbf{m}|^2}{4\pi |\mathbf{r}_{ij}|^3}\left(1-3\left(\hat{\mathbf{m}}\cdot\hat{\mathbf{r}}_{ij}\right)^2\right). \quad \text{(S3)}$$

We define γ_{ij} as the angle between r_{ij} and H, giving:

$$U_{ij}\left(\gamma_{ij}\right) = \frac{\mu_0 |\mathbf{m}|^2}{4\pi |\mathbf{r}_{ij}|^3}\left(1-3\cos^2\gamma_{ij}\right). \quad \text{(S4)}$$

While Equation S4 provides important insight as it carries a negative cosine-squared dependency on angle, the same as the optical trap,[1] γ_{ij} are not generally the same as the angle θ between the long axis of the GNR and H, since the displacement between each pair of NPs is not generally along the GNR. Intuitively, we might expect that, when calculating the sum in Equation S1, the components of r_{ij} perpendicular to the long axis of the GNR would cancel out, provided the NPs uniformly decorate the GNR. To analytically tabulate this effect, we rewrite Equation S3 in terms of θ and transform the coordinates from the lab frame (x,y,z) to the MagGNR frame (x',y',z') by rotation about the x-axis by ϕ and then about the z'-axis by θ. The diagram below depicts the new coordinate system translated along x' for clarity (i.e., the coordinate systems share the same origin, which is where the center of the MagGNR is located):

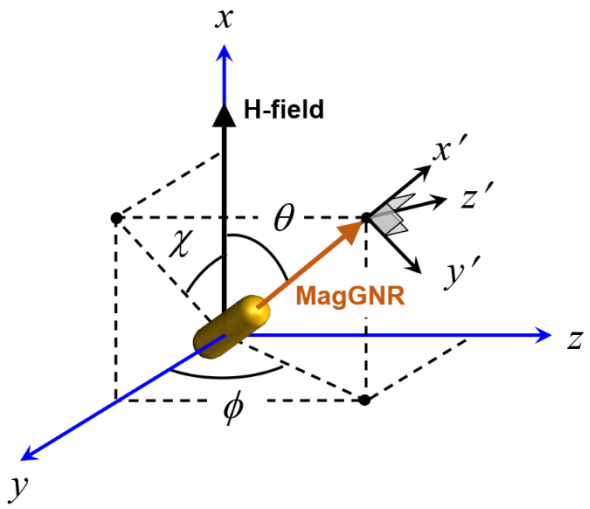

The components of r_{ij} along H can be written as:

$$\mathbf{r}_{ij} = \Delta x'_{ij}\hat{i}' + \Delta y'_{ij}\hat{j}' + \Delta z'_{ij}\hat{k}' , \tag{S5}$$

where $\Delta x'_{ij}$ and $\Delta y'_{ij}$ are the x'- and y'- displacement components between two NPs in the coordinate frame of the MagGNR (such that x' is along the long axis of the GNR). Using $\hat{\mathbf{m}} = \hat{i}$, we obtain:

$$\hat{\mathbf{m}} \cdot \hat{\mathbf{r}}_{ij} = \frac{\hat{i} \cdot \mathbf{r}_{ij}}{\left|\mathbf{r}_{ij}\right|} = \frac{\Delta x'_{ij}\cos\theta - \Delta y'_{ij}\sin\theta}{\left|\mathbf{r}_{ij}\right|} . \tag{S6}$$

There is no explicit $\Delta z'_{ij}$ dependence because the z'-axis is perpendicular to the x-axis. This is because we neglect a possible third rotation of the GNR coordinates about its long axis due to the assumed axisymmetry of the GNR. Substituting Equation S5 into Equation S3 and performing some algebraic manipulation gives:

$$U_{ij}(\theta) = \frac{\mu_0 \left|\mathbf{m}\right|^2}{4\pi \left|\mathbf{r}_{ij}\right|^3}\left(\left(1 - \frac{3\Delta y'^{\,2}_{ij}}{\left|\mathbf{r}_{ij}\right|^2}\right) - \left(\frac{3\left(\Delta x'^{\,2}_{ij} - \Delta y'^{\,2}_{ij}\right)\cos^2\theta}{\left|\mathbf{r}_{ij}\right|^2}\right) - \left(\frac{3\Delta x'_{ij}\Delta y'_{ij}\sin 2\theta}{\left|\mathbf{r}_{ij}\right|^2}\right)\right). \tag{S7}$$

Examining the three terms in parentheses, we see that the first term represents a constant offset independent of θ, which may be ignored because only potential energy differences are relevant to magnetic trapping (i.e., the potential energy offset can be arbitrarily set). The third term, being linear in both $\Delta x'_{ij}$ and $\Delta y'_{ij}$, is expected to sum to zero when applying Equation S1, since the NPs are uniformly distributed about the MagGNR centered at $x' = y' = 0$. Therefore, only the second term is relevant for determining θ-dependence of U_{ij}. Since the MagGNR is prolate with its long axis along x', we expect that the $\Delta x'^{\,2}_{ij}$ terms will be larger than the $\Delta y'^{\,2}_{ij}$ terms when summed, such that the final result has the familiar negative cosine-squared relationship:

$$U_{MagGNR}(\theta) \sim -\cos^2\theta \frac{3\mu_0 |\mathbf{m}|^2}{4\pi |\mathbf{r}_{ij}|^5} \sum_j \sum_{i>j} \left(\Delta x'^2_{ij} - \Delta y'^2_{ij}\right) = -nk_B T \cos^2\theta \quad \text{(S8)}$$

This shows explicitly how the trap depth n is related to the positions of the NPs and magnetic moments induced by the applied magnetic field. For example, the expression indicates how the greater the aspect ratio of the MagGNR, the more the $\Delta x'_{ij}{}^2$ terms dominate over the $\Delta y'_{ij}{}^2$ terms, thus increasing the trap depth.

Quantifying Magnetic Alignment from Optical Extinction Spectroscopy

In optical spectroscopy, we acquire extinction (also known as absorbance) A by measuring the optical intensity I incident and transmitted through a sample:

$$A = -\log_{10}\left(\frac{I_{transmitted}}{I_{incident}}\right), \quad \frac{I_{transmitted}}{I_{incident}} = e^{-C_{ext}Nz} = 10^{-A} \quad \text{(S9)}$$

where Beer's law is used to show that the extinction cross-section C_{ext} is proportional to A, via the number density of MagGNRs, N, and the optical path length through the sample z. Since much of the underlying optical scattering theory treats C_{ext}, this proportionality is used to connect theory with experimental measurements of A.

C_{ext} of a GNR is a sum of the absorption and scattering cross-sections C_{abs} and C_{sca}, respectively. In the Rayleigh approximation (particles small compared to the wavelength), each of these will depend upon the polarizability tensor α of the GNR:[2,3]

$$C_{abs} = k\frac{\mathrm{Im}\left(\mathbf{E}_0^{\,*}\cdot\boldsymbol{\alpha}\mathbf{E}_0\right)}{\mathbf{E}_0^{\,*}\cdot\mathbf{E}_0}$$
$$C_{sca} = \frac{k^4}{6\pi}\frac{\left(\boldsymbol{\alpha}\mathbf{E}_0^{\,*}\right)\cdot\left(\boldsymbol{\alpha}\mathbf{E}_0\right)}{\mathbf{E}_0^{\,*}\cdot\mathbf{E}_0}, \quad \text{(S10)}$$

where k is the wavenumber, and E_0 is the incident electric field. For GNRs of the aspect ratios and sizes in our experiments, both absorption and scattering may be significant, so both are included in this analysis.

If we define the long axis of the GNR as "1" and the two transverse axes as "2" (since they are degenerate), the polarizability tensor, in the frame of the GNR, can be written simply as:

$$\boldsymbol{\alpha}_{GNR} = \begin{pmatrix} \alpha_1 & 0 & 0 \\ 0 & \alpha_2 & 0 \\ 0 & 0 & \alpha_2 \end{pmatrix}, \quad \text{(S11)}$$

where α_1 is dominant at the LSPR wavelength and α_2 is dominant at the TSPR wavelength.

When a GNR is aligned with its long axis is exactly parallel or perpendicular to the polarization of the incident light, the extinction coefficients $C_{\mathrm{ext},1}$ and $C_{\mathrm{ext},2}$ can be obtained from Equations S10, S11:

$$C_{ext,1} = k\,\mathrm{Im}\left(\alpha_1\right) + \frac{k^4}{6\pi}\left|\alpha_1\right|^2$$
$$C_{ext,2} = k\,\mathrm{Im}\left(\alpha_2\right) + \frac{k^4}{6\pi}\left|\alpha_2\right|^2. \quad \text{(S12)}$$

In experiments in this work, the MagGNR orientations are described by polar angle θ and azimuthal angle ϕ relative to a magnetic field in the laboratory frame along the x-axis according to the figure above. To predict the optical response for such an arbitrary orientation, one must first write the GNR polarizability in the laboratory frame by appropriate rotation operations:

$$\boldsymbol{\alpha}_{lab}(\theta,\phi) = \mathbf{R}^{-1}(\theta,\phi)\boldsymbol{\alpha}_{GNR}\mathbf{R}(\theta,\phi), \tag{S13}$$

where

$$\mathbf{R}(\theta,\phi) = \begin{pmatrix} \cos\theta & \sin\theta\cos\phi & \sin\theta\sin\phi \\ -\sin\theta & \cos\theta\cos\phi & \cos\theta\sin\phi \\ 0 & -\sin\phi & \cos\phi \end{pmatrix}. \tag{S14}$$

Then, to predict the extinction coefficients for an electromagnetic field polarized along *x* (parallel to H) or *y* (perpendicular to H), we find $C_{\text{ext},\parallel}$ and $C_{\text{ext},\perp}$, after much simplification, respectively, as:

$$\begin{aligned} C_{ext,\parallel}(\theta) &= C_{ext,1}\cos^2\theta + C_{ext,2}\sin^2\theta \\ C_{ext,\perp}(\theta,\phi) &= C_{ext,1}\sin^2\theta\cos^2\phi + C_{ext,2}\left(\cos^2\theta\cos^2\phi + \sin^2\phi\right) \end{aligned} \tag{S15}$$

In this study, measurements of *A* were analyzed at the LSPR wavelength, in which case $\alpha_2 << \alpha_1$ and $C_{\text{ext},2} << C_{\text{ext},1}$. We obtain the simplification:

$$\begin{aligned} C_{ext,\parallel}(\theta) &= C_{ext,1}\cos^2\theta \\ C_{ext,\perp}(\theta,\phi) &= C_{ext,1}\cos^2\phi\sin^2\theta \end{aligned}. \tag{S16}$$

The measurements are collected over an ensemble of MagGNRs with an angular distribution f_θ, as in Equation 5, which is independent of ϕ. We may assume the MagGNRs have identical optical properties, so that the ensemble averages simplify as follows:

$$\begin{aligned} A_\parallel &\propto \left\langle C_{ext,\parallel}(\theta)\right\rangle = C_{ext,1}\left\langle\cos^2\theta\right\rangle \\ A_\perp &\propto \left\langle C_{ext,\perp}(\theta,\phi)\right\rangle = C_{ext,1}\left\langle\cos^2\phi\sin^2\theta\right\rangle = \frac{1}{2}C_{ext,1}\left\langle\sin^2\theta\right\rangle \end{aligned}, \tag{S17}$$

where both extinctions have the same constants of proportionality (determined by experimental conditions). Therefore, ratiometric parameters can be computed, such as the optical anisotropy:

$$\frac{A_{\parallel}}{A_{\perp}} = \frac{C_{ext,1}\left\langle \cos^2\theta \right\rangle}{C_{ext,1}\left\langle \sin^2\theta\cos^2\phi \right\rangle} = 2\frac{\left\langle \cos^2\theta \right\rangle}{\left\langle \sin^2\theta \right\rangle} \tag{S18}$$

and the 3D order parameter:

$$\begin{aligned} S_{3D,optical} &= \frac{A_{\parallel} - A_{\perp}}{A_{\parallel} + 2A_{\perp}} = \frac{C_{ext,1}\left\langle \cos^2\theta \right\rangle - C_{ext,1}\left\langle \sin^2\theta \right\rangle / 2}{C_{ext,1}\left\langle \cos^2\theta \right\rangle + C_{ext,1}\left\langle \sin^2\theta \right\rangle} \\ &= \left\langle \cos^2\theta \right\rangle - \frac{1}{2}\left\langle 1 - \cos^2\theta \right\rangle \\ &= \frac{3\left\langle \cos^2\theta \right\rangle - 1}{2} \end{aligned} \quad . \tag{S19}$$

Summary of Analysis of Alignment of MagGNRs

First, we express the 2D order parameter, $S_{2D} = 2\left\langle \cos^2\chi \right\rangle - 1$, in terms of the angles θ and ϕ defined in the above figure, so that it can be computed from knowledge of the 3D angular distribution. In this picture, the unit vector corresponding to the long axis of the MagGNR written in the laboratory frame is given by a rotation according to the inverse of the matrix R in Equation S14. (Note that the inverse of R is also its transpose.) This unit vector is thus:

$$\hat{g} = \mathbf{R}^{-1}\begin{pmatrix} 1 \\ 0 \\ 0 \end{pmatrix} = \hat{i}\cos\theta + \hat{j}\sin\theta\cos\phi + \hat{k}\sin\theta\sin\phi\,, \tag{S20}$$

and thus,

$$\cos^2\chi = \frac{{g_x}^2}{{g_x}^2 + {g_y}^2} = \frac{\cos^2\theta}{\cos^2\theta + \sin^2\theta\cos^2\phi}. \tag{S21}$$

Therefore, the ensemble average is:

$$\begin{aligned}\left\langle \cos^2\chi \right\rangle &= \int_0^{2\pi}\int_{-\pi/2}^{\pi/2} \frac{\cos^2\theta'}{\cos^2\theta' + \sin^2\theta'\cos^2\phi'} f_{\theta'}(n)\left|\sin\theta'\right| d\theta' d\phi' \\ &= 2\pi \int_{-\pi/2}^{\pi/2} \cos\theta' f_{\theta'}(n)\left|\sin\theta'\right| d\theta' \\ &= \left\langle \cos\theta \right\rangle\end{aligned} \quad , \tag{S22}$$

and

$$\begin{aligned}S_{2D} &= 2\left\langle \cos^2\chi \right\rangle - 1 \\ &= 2\left\langle \cos\theta \right\rangle - 1\end{aligned} . \tag{S23}$$

Now that we have expressions for the order parameters S_{2D} and S_{3D} in terms of ensemble averages over functions of θ, we can follow the method as in Equations 5-7 to compute their values for a known trap depth parameter n. Briefly summarized, this would be done by:

$$\begin{aligned}Z(n) &= 2\pi \int_{-\pi/2}^{\pi/2} \mathrm{e}^{n\cos^2\theta'} \left|\sin\theta'\right| d\theta' \\ f_\theta(n) &= \frac{\mathrm{e}^{n\cos^2\theta}}{Z(n)} \\ \left\langle \cos\theta \right\rangle &= 2\pi \int_{-\pi/2}^{\pi/2} \cos\theta' f_{\theta'}(n)\left|\sin\theta'\right| d\theta' \\ \left\langle \cos^2\theta \right\rangle &= 2\pi \int_{-\pi/2}^{\pi/2} \cos^2\theta' f_{\theta'}(n)\left|\sin\theta'\right| d\theta' \\ S_{2D} &= 2\left\langle \cos\theta \right\rangle - 1 \\ S_{3D} &= \frac{3\left\langle \cos^2\theta \right\rangle - 1}{2}\end{aligned} \quad , \tag{S24}$$

where the integrals are evaluated numerically in *Mathematica*.

Synthesis of Small Fe_3O_4 NPs

Oleylamine-stabilized magnetite (Fe_3O_4) NPs with average diameters of ~7 nm were synthesized by a reductive thermal decomposition method.[4] 1.05 g of iron(III) acetylacetonate was dissolved in a mixture of 15 mL benzyl ether and 15 mL oleylamine, which served as ligand and reducing agent, in a round-bottomed flask connected to a Schlenk line. The mixture was degassed at room temperature under vacuum for 1 hour, followed by backfilling with nitrogen and heating to 120 °C for another hour under inert atmosphere. The temperature was then quicky increased to 210 °C and held for another 1 hour. After allowing the product to cool to room temperature, 50 mL of ethanol was added to assist flocculation of the NPs during centrifugation at 4000 rpm (1753 *g*) for 5 min. The sedimented oleylamine-stabilized Fe_3O_4 NPs were then dispersed in 10 mL chloroform. An aliquot of 0.25 mL from this stock solution was diluted with chloroform to a total volume of 10 mL. PEI functionalization was then performed as described in the main text, by adding a solution of 100 mg of PEI dissolved in 30 mL of chloroform with vigorous stirring.

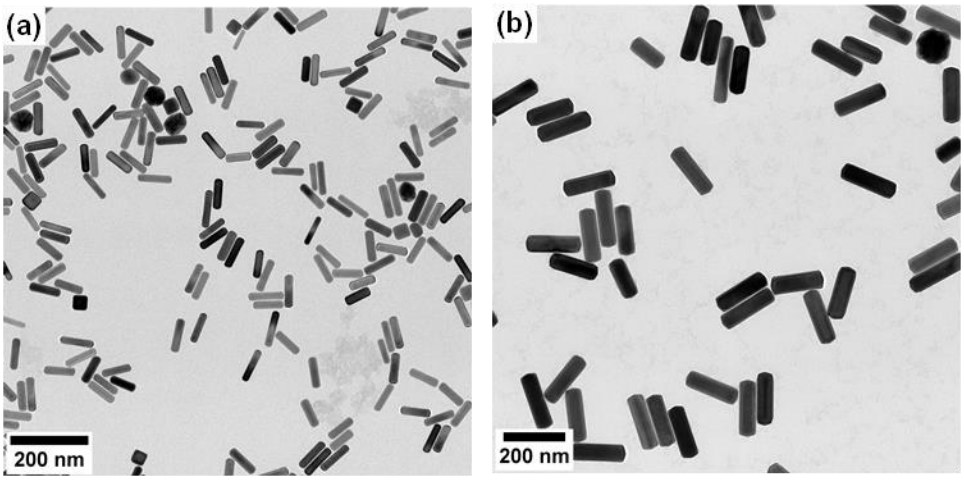

Figure S1. TEM images of (a) small and (b) large BSA-GNRs.

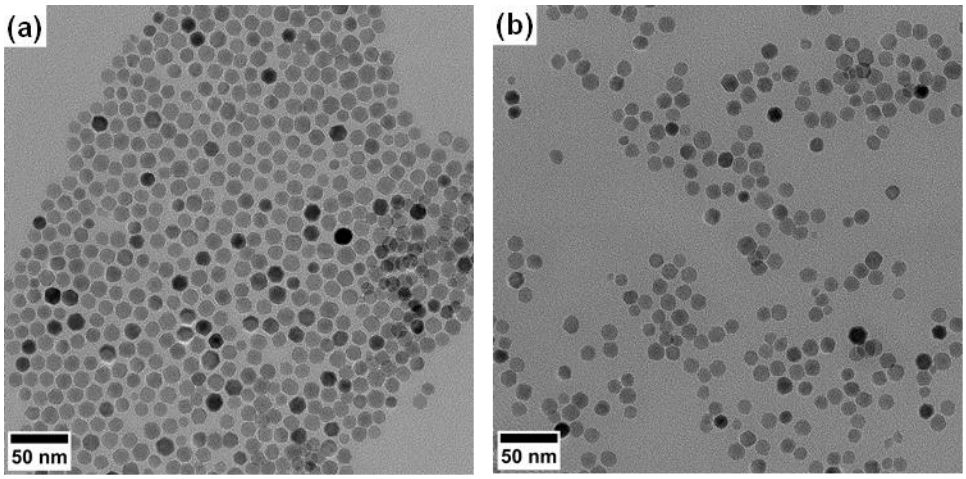

Figure S2. TEM images of Fe_3O_4 NPs (a) stabilized with native oleic acid ligands and (b) after functionalization with PEI.

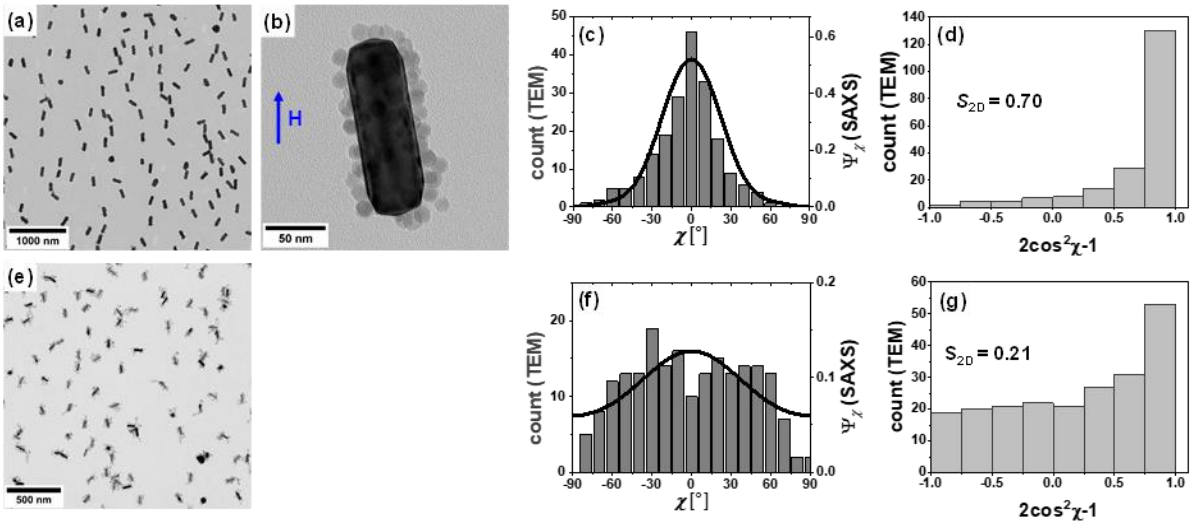

Figure S3. TEM images of large MagGNRs dried under 10 kOe magnetic field parallel to the grid and in the vertical direction in the images at (a) lower magnification (b) higher magnification. (c) Angular distribution and (d) S_{2D} calculated from measurements of 200 aligned large MagGNRs, overlaid with the corresponding distributions from SAXS measurements. The same (e) imaging in 10 kOe field, (f) measurements and tabulation of the angular distribution, and (g) calculation of S_{2D} were performed on 200 aligned small MagGNRs.

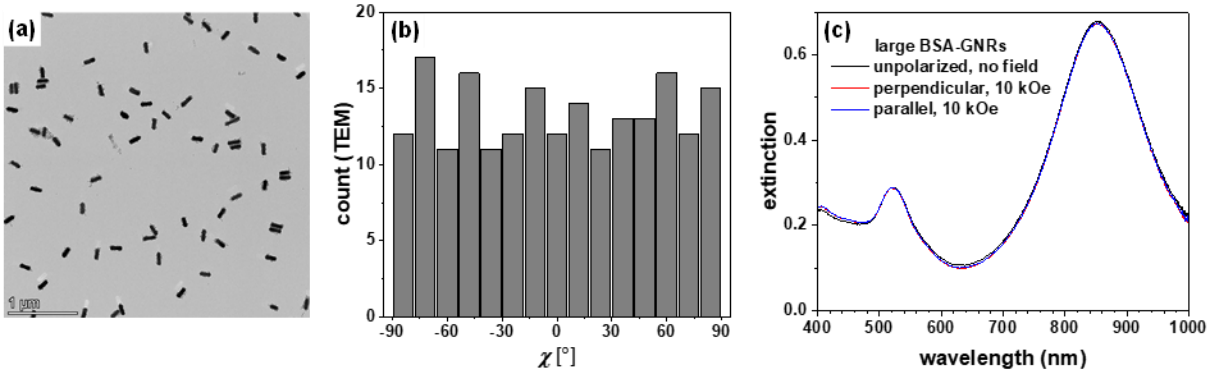

Figure S4. Control experiments confirming no alignment without combined use of magnetic overcoatings and magnetic fields. (a) Large MagGNRs dried without a magnetic field and imaged by TEM with (b) measurements of the angular distribution of 200 MagGNRs with respect to vertical direction. (c) Unpolarized and polarized optical extinction spectra of BSA-GNRs measured in 10 kOe field in an electromagnet.

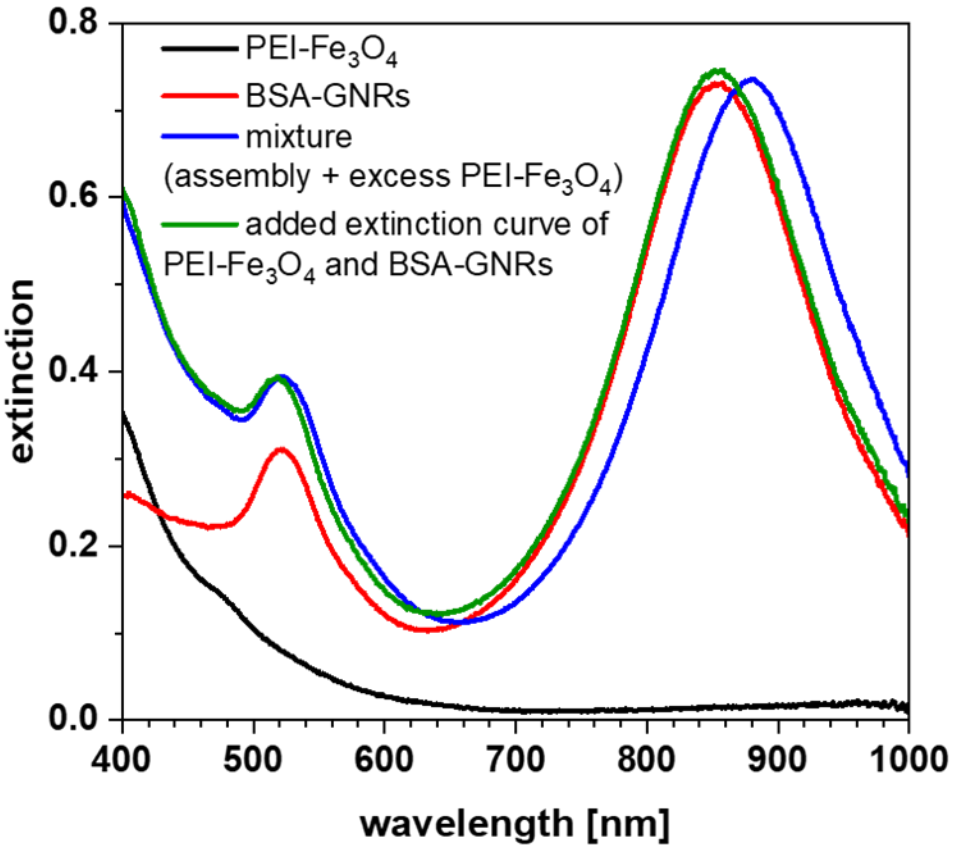

Figure S5. The extinction of the GNR core is preserved after assembly of MagGNRs. Extinction spectra of large BSA-GNRs and PEI-Fe_3O_4 before and after mixing for two hours and before purification are compared with their sum. The spectra have been adjusted to account for dilution effects. The mixture contains MagGNRs and excess PEI-Fe_3O_4 NPs. The LSPR intensity is not affected in the MagGNRs, and a redshift is observed, which is discussed in the main text. The consistent intensity of the LSPR during assembly validates normalization of the extinction spectra of BSA-GNRs and MagGNRs at the LSPR in Figure 4.2.

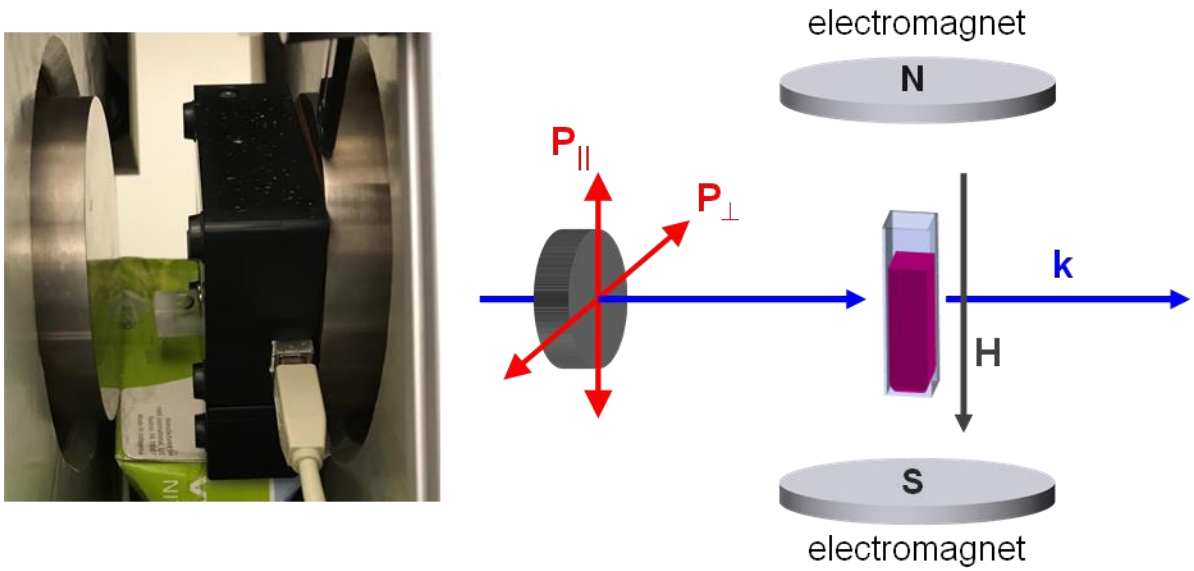

Figure S6. (Left) Photograph of the spectrophotometer placed between the poles of the electromagnet and (right) schematic (rotated 90° clockwise with respect to the photograph) of spectroscopy measurements in the electromagnet, with light of polarization **P** propagating along **k**.

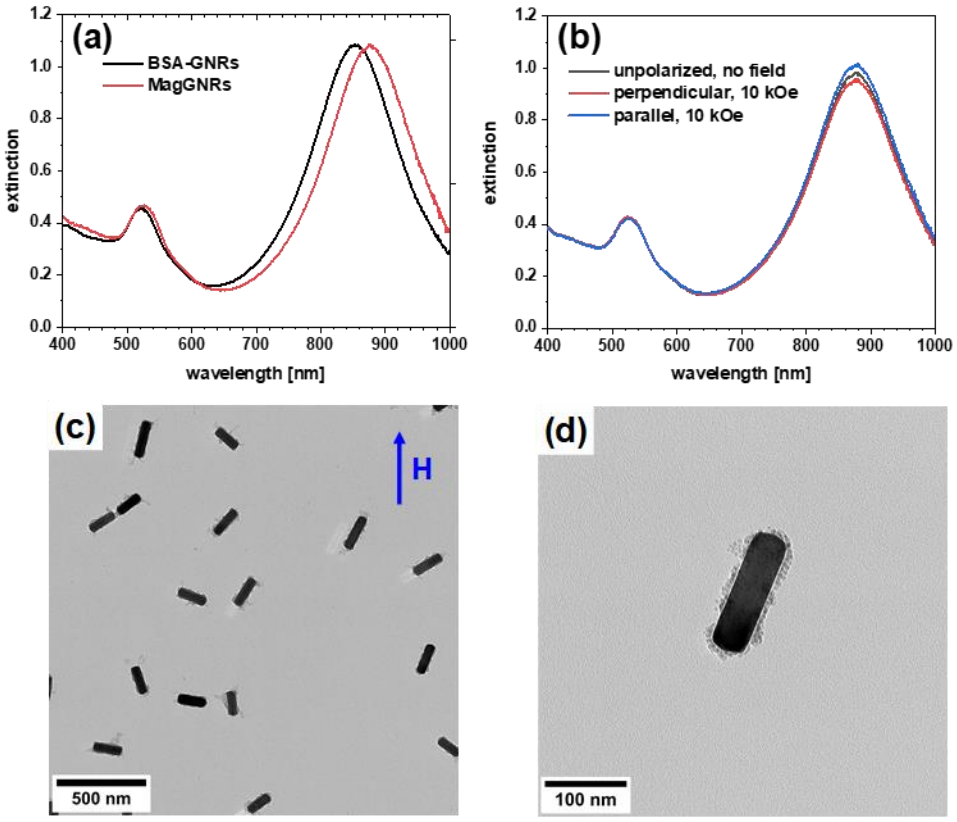

Figure S7. (a) Extinction spectra of large BSA-GNRs and MagGNRs prepared with small, 7 nm PEI-Fe_3O_4 NPs. (b) Polarized extinction spectra of these MagGNRs in a 10 kOe magnetic field. (c) TEM images after drying in a 10 kOe magnetic field, including (d) a magnified image of a single MagGNR.

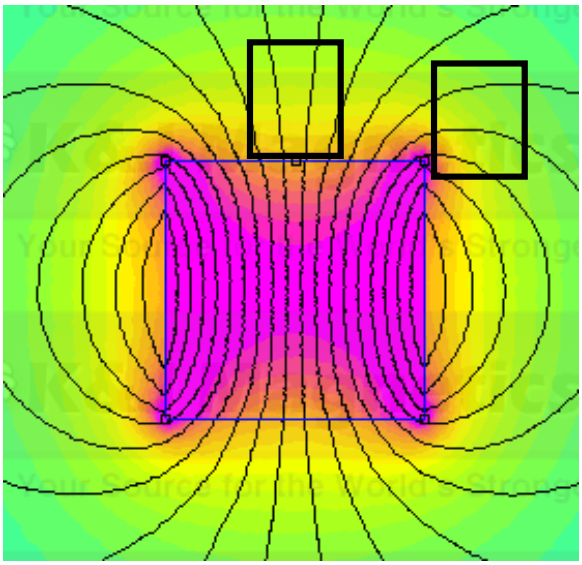

Figure S8. Magnetic field distribution around 1'' N52 cube magnet, calculated using https://www.kjmagnetics.com/calculator.asp. Approximate locations of the cuvettes with MagGNRs in Figure 4.4 a-c are indicated by overlaid rectangles.

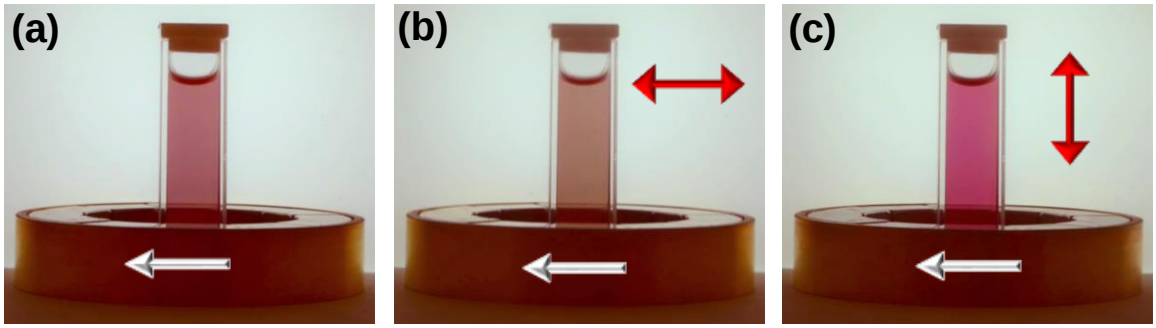

Figure S9. Photos of large MagGNRs in a horizontal magnetic field from a circular Halbach array (a) without polarizer film and with (b) horizontal and (c) vertical polarizer films. The magnetic field and polarizer directions are indicated by single-headed and double-headed arrows, respectively.

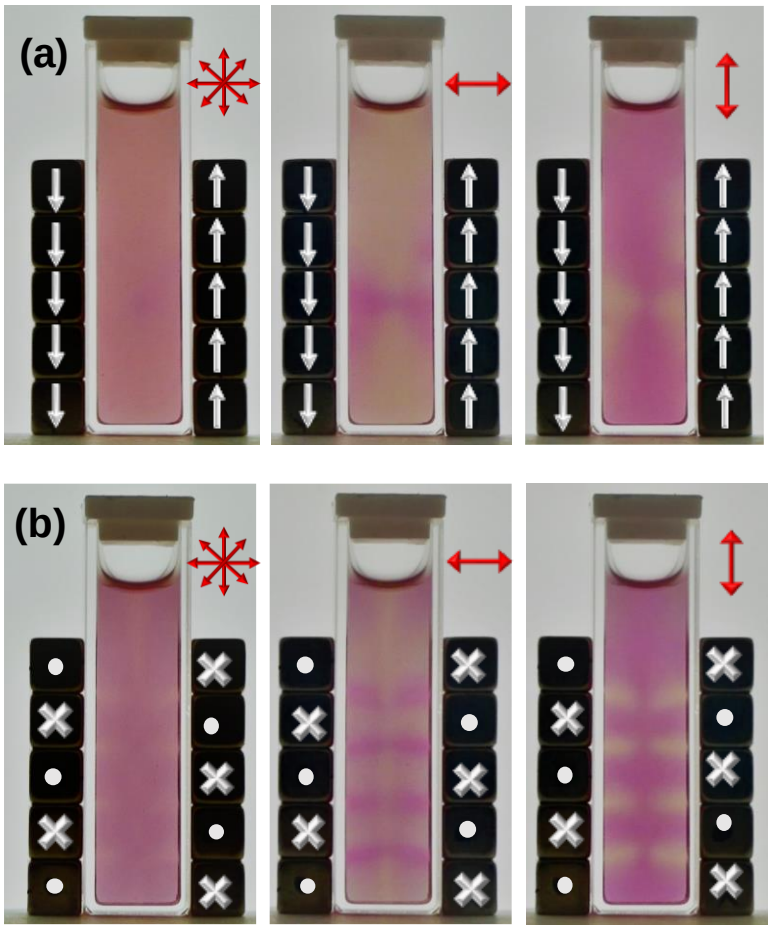

Figure S10. Photos of cuvette with large MagGNRs placed between arrays of five ¼" cube magnets without and with polarizer for (a) vertical, in-plane and (b) out-of-plane magnetic fields.

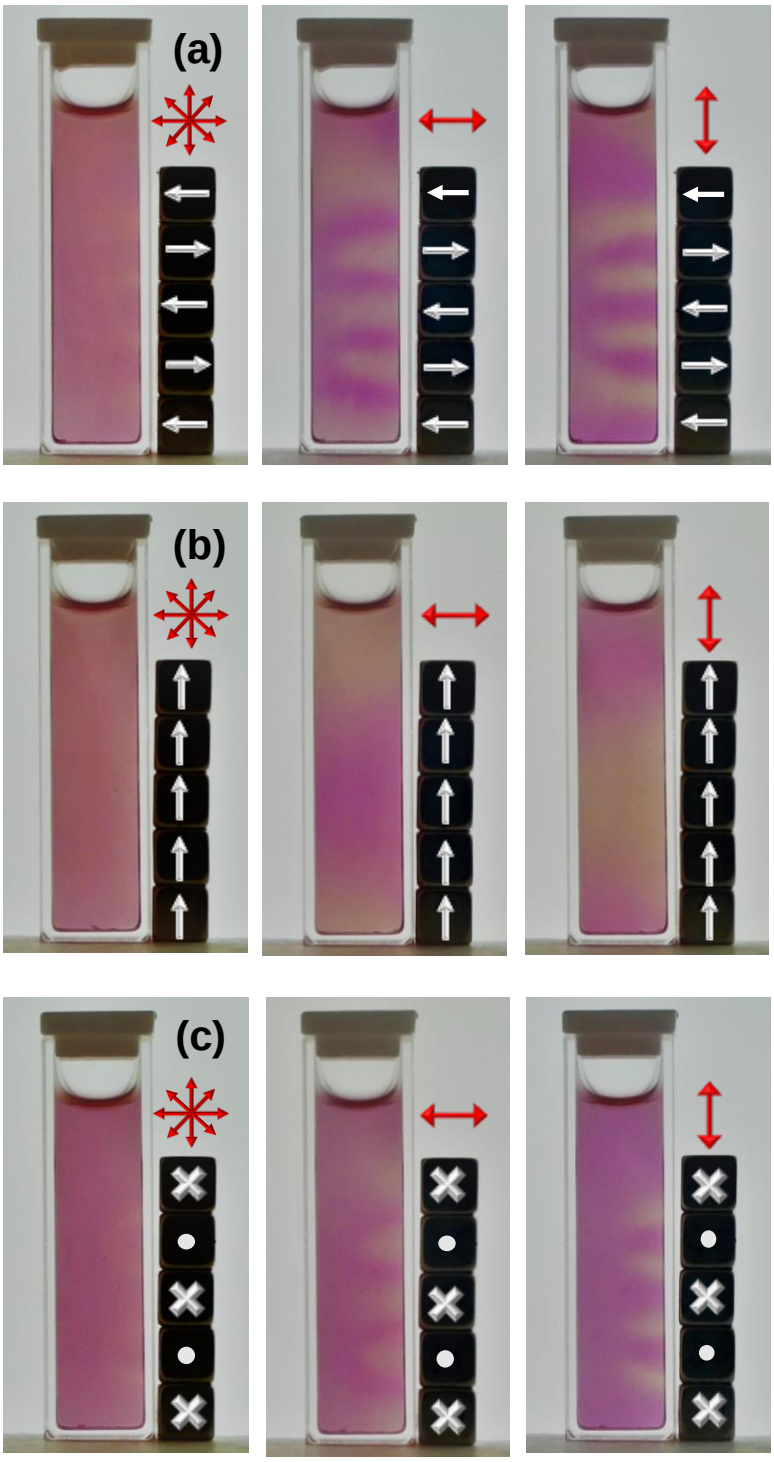

Figure S11. Photos of cuvette with large MagGNRs placed next to a single array of five ¼" cube magnets without and with polarizer for (a) horizontal, in-plane, (b) vertical, in-plane, and (c) out-of-plane magnetic fields.

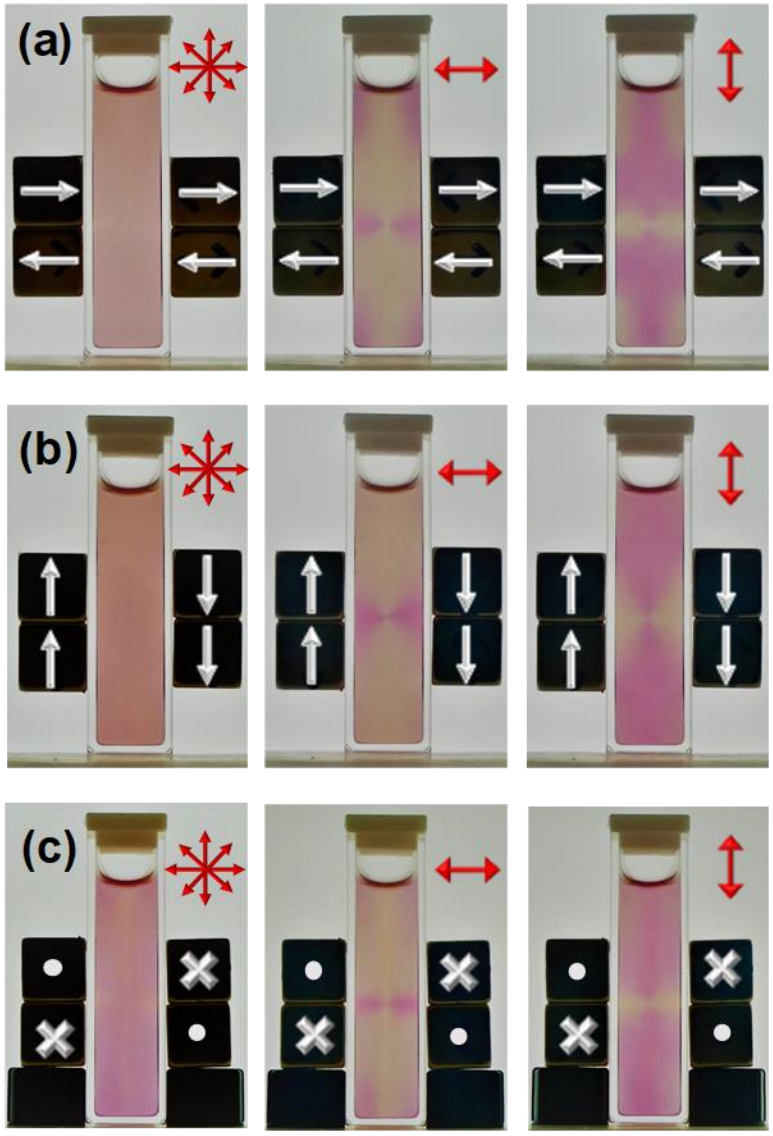

Figure S12. Photos of cuvette with large MagGNRs placed between arrays of two 10 mm cube magnets without and with polarizer for (a) horizontal, in-plane, (b) vertical, in-plane, and (c) out-of-plane magnetic fields.

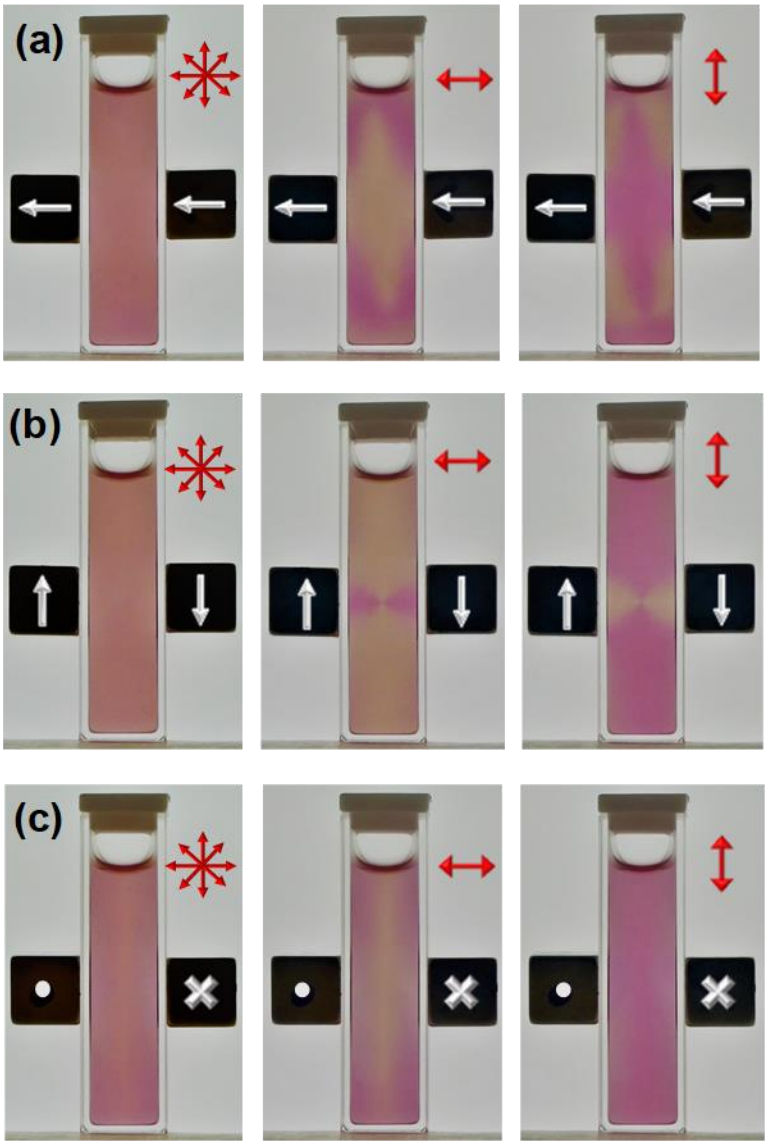

Figure S13. Photos of cuvette with large MagGNRs placed between a pair of 10 mm cube magnets without and with polarizer for (a) horizontal, in-plane, (b) vertical, in-plane (c) out-of-plane magnetic fields.

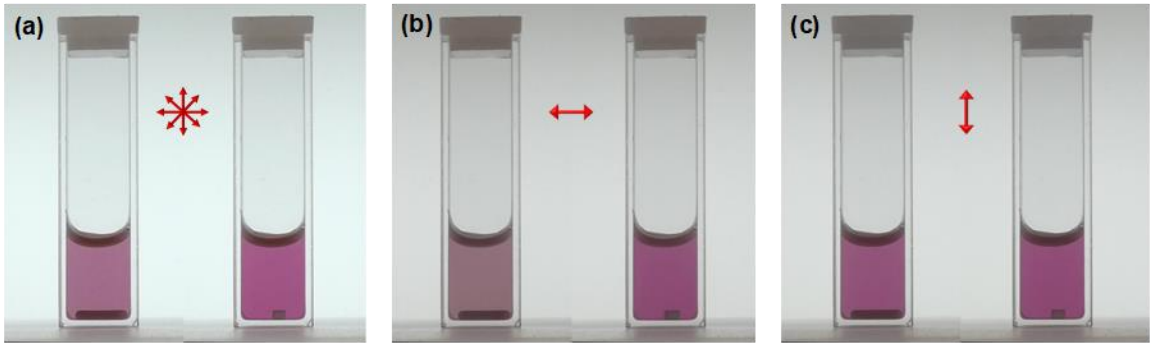

Figure S14. Pairs of snapshots from Movie S8 of large MagGNRs with a stir bar placed on a stir plate with the field (left photo) in-plane or (right photo) out-of-plane (a) without a polarizer, (b) with a horizontal polarizer, and (c) with a vertical polarizer.

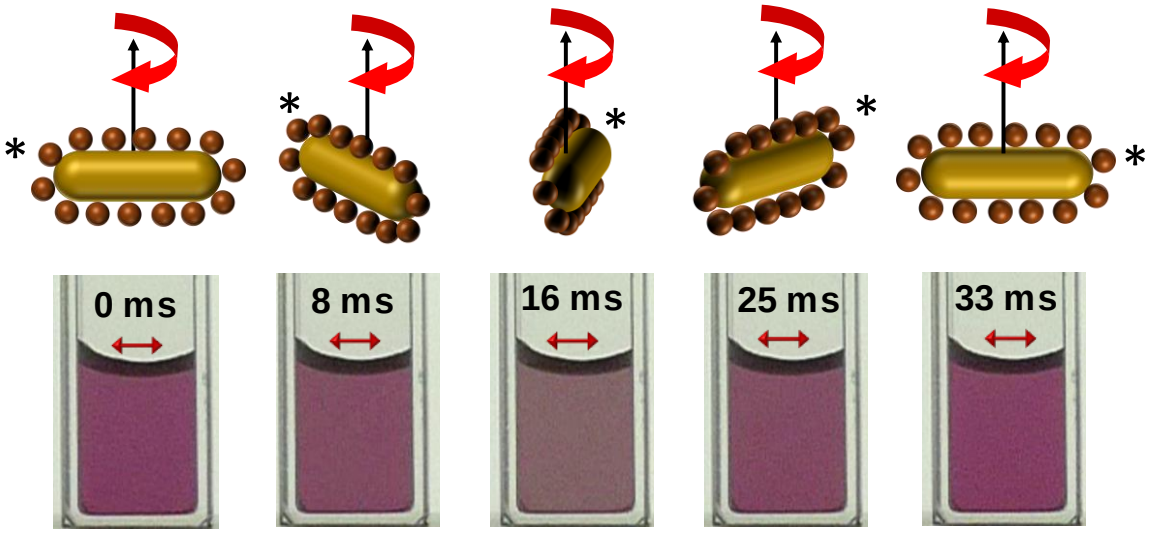

Figure S15. Snapshots from Movie S9 of large MagGNRs rotating on a stir plate set at 1000 rpm with a horizontal polarizer. Analysis of the video shows that 120 cycles of color change, corresponding to 60 full rotations, occur in 3.634 s, which is equivalent to speed of 991 rpm.

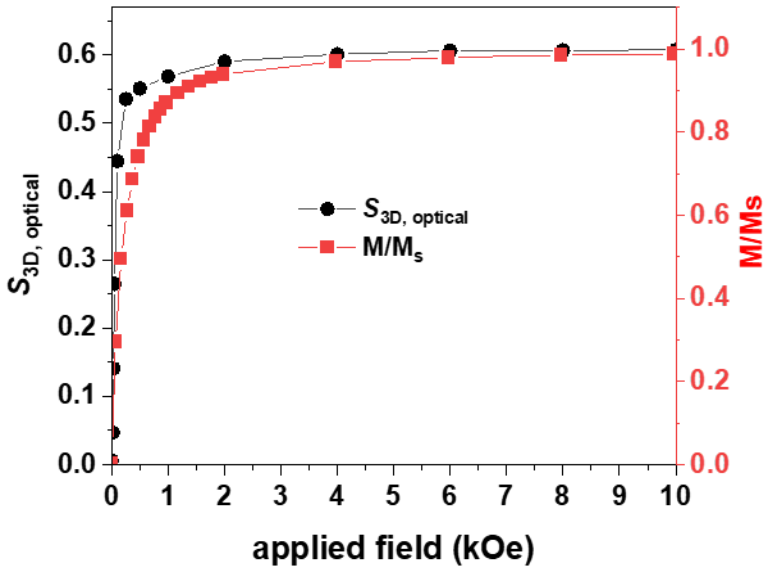

Figure S16. $S_{3D, optical}$ and magnetization of MagGNRs as a function of applied magnetic field.

References

(1) Ruijgrok, P. V.; Verhart, N. R.; Zijlstra, P.; Tchebotareva, A. L.; Orrit, M. Brownian Fluctuations and Heating of an Optically Aligned Gold Nanorod. *Phys. Rev. Lett.* **2011**, *107*, 037401.

(2) Bohren, C. F.; Huffman, D. R. *Absorption and Scattering of Light by Small Particles*. Wiley: Weinheim, Germany, 2004.

(3) Markel, V. A. Extinction, scattering and absorption of electromagnetic waves in the coupled-dipole approximation. *J. Quant. Spectrosc. Radiat. Transf.* **2019**, *236*, 106611.

(4) Xu, Z.; Shen, C.; Hou, Y.; Gao, H.; Sun, S. Oleylamine as Both Reducing Agent and Stabilizer in a Facile Synthesis of Magnetite Nanoparticles. *Chem. Mater.* **2009**, *21*, 1778-1780.

Chapter 5. Contribution to Other Significant Projects

In addition to my main research project on electrostatic assembly for multifunctional properties and magnetic manipulation, I have contributed to several collaborative projects. This chapter presents some of my contributions to other research projects.

5.1 Fe_3O_4 NPs for Hydrogel Composites

This project was led by Niels Holten-Andersen and Gareth McKinley at MIT, where they developed physical hydrogels using Fe_3O_4 NPs as crosslinkers. Fe_3O_4 NPs are crosslinked with 4-arm nitrocatechol-functionalized poly(ethylene glycol) (4nPEG) linker chains, which leads to arrested NP hydrogels through supramolecular interactions. My role in this project was to synthesize monodisperse, oleylamine-stabilized Fe_3O_4 NPs with an average diameter of 7 nm (Figure 5.1). The NPs were then further functionalized with catechol for gelation.

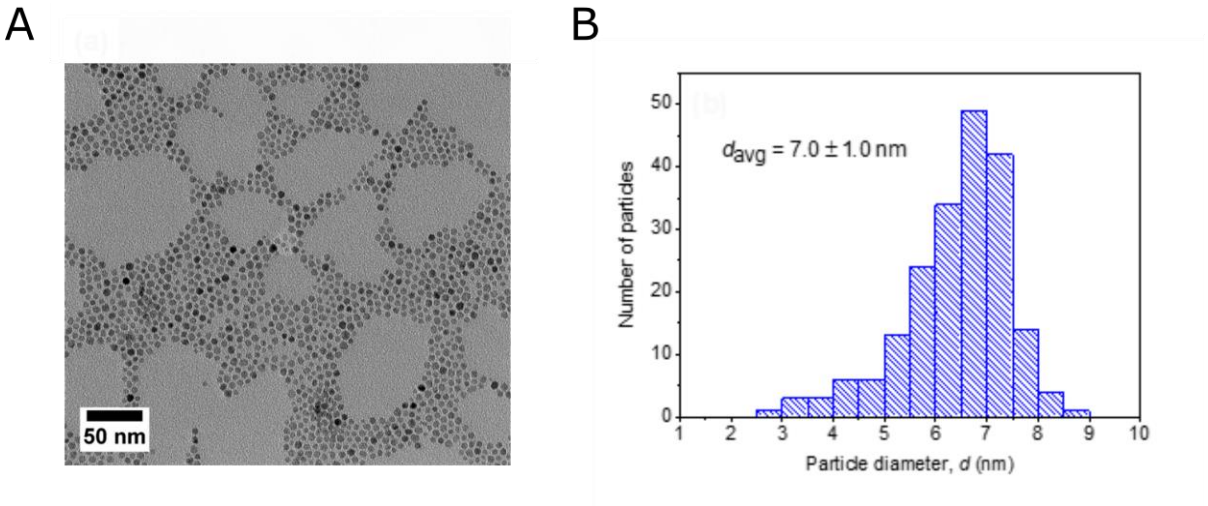

Figure 5.1. (A) TEM image of oleylamine-stabilized Fe_3O_4 NPs. (B) Size distribution of the NPs[1]

Results from his project have been published in two papers. The first paper reports the preparation and characterization of these NP-based hydrogels.[1] This work shows that the anisotropic interaction between NPs can be tailored by adjusting the relative amounts of NPs and

polymeric crosslinkers, which affects the mechanical properties stress relaxation. The anisotropic structure of the NP-based hydrogel reduced the percolation threshold. The second part of the project probes the microscopic origins of slow stress relaxation with a broad distribution of relaxation times in arrested NP-based hydrogels.[2]

5.2 Gold NPs in Shape Memory Polymer

In this project, Au NPs were dispersed in shape memory polymer films to investigate anisotropic plasmon coupling effects after stretching.[3] Au NPs form clusters in the polymer before stretching. Stretching led to stronger (weaker) plasmon coupling parallel (perpendicular) to the stretching direction and thus causes a red (blue) shift in the polarized extinction spectra for light polarized parallel (perpendicular) to the stretching direction. Upon heating to thermally drive shape recovery, the polymer film returns to the original, unstretched shape. Structural characterization shows complete nanoscale recovery of the clusters of NPs heating, which restored optical isotropy in polarized light.

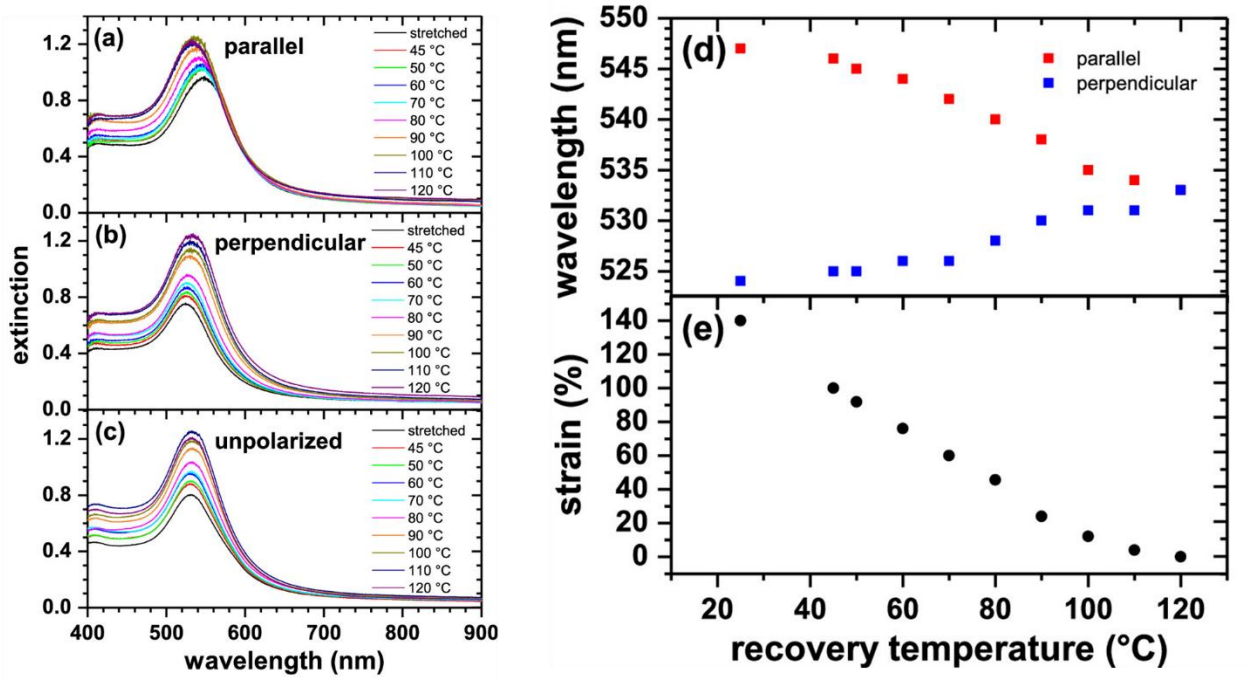

Figure 5.2. Polarized and unpolarized extinction spectra for stretched polymer films and during stepwise shape recovery for heating from 45 °C to 120 °C for light polarized (a) parallel or (b) perpendicular to the stretching direction and (c) for unpolarized light. (d) Wavelength corresponding to the extinction maximum for light with parallel and perpendicular polarization and (e) strain (%) measured from the changes in length of the film during stepwise thermal shape recovery.[3]

In this project, I collaborated with Prachi Yadav, as MS student in the Tracy research group. After Prachi's graduation, I synthesized Au NPs and performed some additional experiments, including stepwise thermal shape recovery experiment for the stretched films. The stretched polymer film recovers, and the optical anisotropy vanishes gradually with increasing recovery temperature from 45 °C to 120 °C. This temperature-dependent polarized optical response could be used for an optical thermal history sensor.

5.3 Gold NPs in Photo-Triggerable Transient Polymer

This project investigated photo-induced depolymerization of fibers composed of a flexible cyclic-poly(phthalaldehyde)/poly(ε-caprolactone) polymer blend, which is promising for applications in photolithography and electronic packaging.[4] The project was led by Ericka Ford from the Wilson College of Textiles at NCSU. The main result of this study is that adding 2 wt% Au NPs in the polymer blend sufficiently enhances daylight-induced transience assisted by photothermal heating from the plasmonic NPs. For this project, I synthesized 15 nm spherical oleylamine stabilized gold NPs.

5.4 Oleylamine Stripping of Fe_3O_4 NPs

Stripping ligands from NPs is commonly performed for different purposes, including to facilitate ligand exchange.[5] Controlled ligand stripping can also result in aggregation of NPs in well-defined clusters.[6] Ligand stripping often occurs during purification processes, where exposing NPs with hydrophobic ligands to polar solvents can strip ligands from the surface of the NPs and may drive undesired agglomeration.[7] Oleylamine-stabilized Fe_3O_4 NPs are of interest for catalysis and biomedical applications after appropriate ligand exchange. In this collaborative project led by Yaroslava Yingling from Materials Science and Engineering at NC State, methods are under development for simulating oleylamine stripping from Fe_3O_4 NPs and the subsequent effects on aggregation of the Fe_3O_4 NPs. Akhlak-Ul Mahmood is a PhD student working on developing the simulation methodologies, and I am providing experimental support to the project.

In this project, I synthesized oleylamine-stabilized Fe_3O_4 NPs following a published method,[8] which is also described in Chapter 5. After synthesis in benzyl ether and oleylamine, ethanol is added to drive flocculation of NPs and then centrifugation is performed followed by discarding the supernatant containing excess oleylamine and benzyl ether. The NPs are then

redispersed in hexanes. Further purification could be performed by adding ethanol to the NPs in hexanes, followed by centrifugation and discarding the supernatant. However, subsequent washing strips away bound oleylamine from the NPs, which is quantified by thermogravimetric analysis (TGA) under a nitrogen atmosphere (Figure 5.3). TGA after the first round of purification shows steep mass loss below 250 °C, which is attributed to unbound ligands, and the mass loss at higher temperature arises from decomposition of bound ligands.[9] Most of the free ligands are removed during the first round of purification, and successive rounds chiefly remove bound ligands. The additional weight loss between washing the NPs two and three times is mostly from bound ligands. The following ligand stripping experiments were carried out with NPs after a single purification step and were redispersed in hexane.

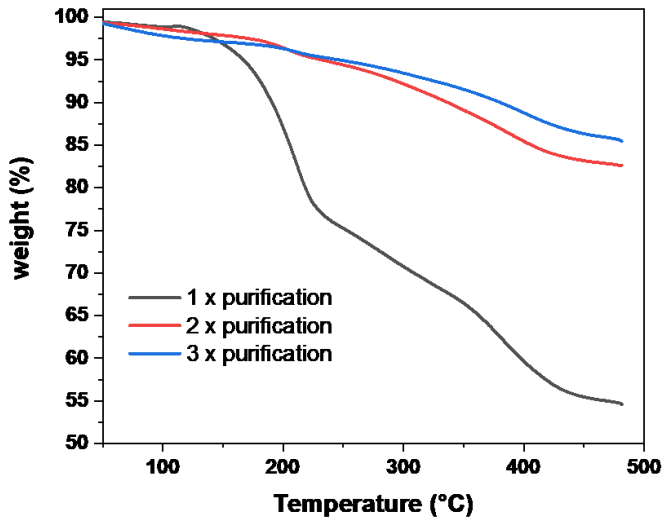

Figure 5.3. TGA of oleylamine-stabilized Fe_3O_4 NPs after different numbers of rounds of purification.

The ligand stripping phenomenon is sensitive to the sequence of adding solvents. We performed ligand stripping by adding ethanol to the NPs dispersed in hexane or NPs in hexane to ethanol to probe the effect of the sequence. Four different concentrations of ethanol were experimentally investigated, 20%, 35%, 50%, and 80%. The concentration of Fe_3O_4 NPs was kept

uniform for all four sets of experiments. For example, for 80% ethanol, 1 mL of NPs dispersed in hexane was added dropwise to 4 mL of ethanol. In the paired sample with the reverse sequence, 4 mL of ethanol was added dropwise to 1 mL of NPs. Both samples were centrifuged followed by removal of supernatant and drying the solids in preparation for TGA measurements. A distinct trend was observed in the TGA results for the different sequences (Figure 5.4). Adding ethanol to the NPs gradually increases the solvent polarity, which is favorable for ligand stripping. In contrast, when the NPs are added to ethanol, the NPs are initially surrounded by ethanol molecules, which drives agglomeration through hydrophobic interactions. The kinetics of ligand stripping might be slower than agglomeration. Consequently, agglomeration may shield the NPs from ligand stripping when they are added to ethanol. TGA shows greater weight loss when the NPs are added to ethanol. The effect is consistent for all four different proportions of ethanol. The effect of the sequence of addition diminishes with decreasing ethanol concentration because of less agglomeration at lower ethanol concentrations.

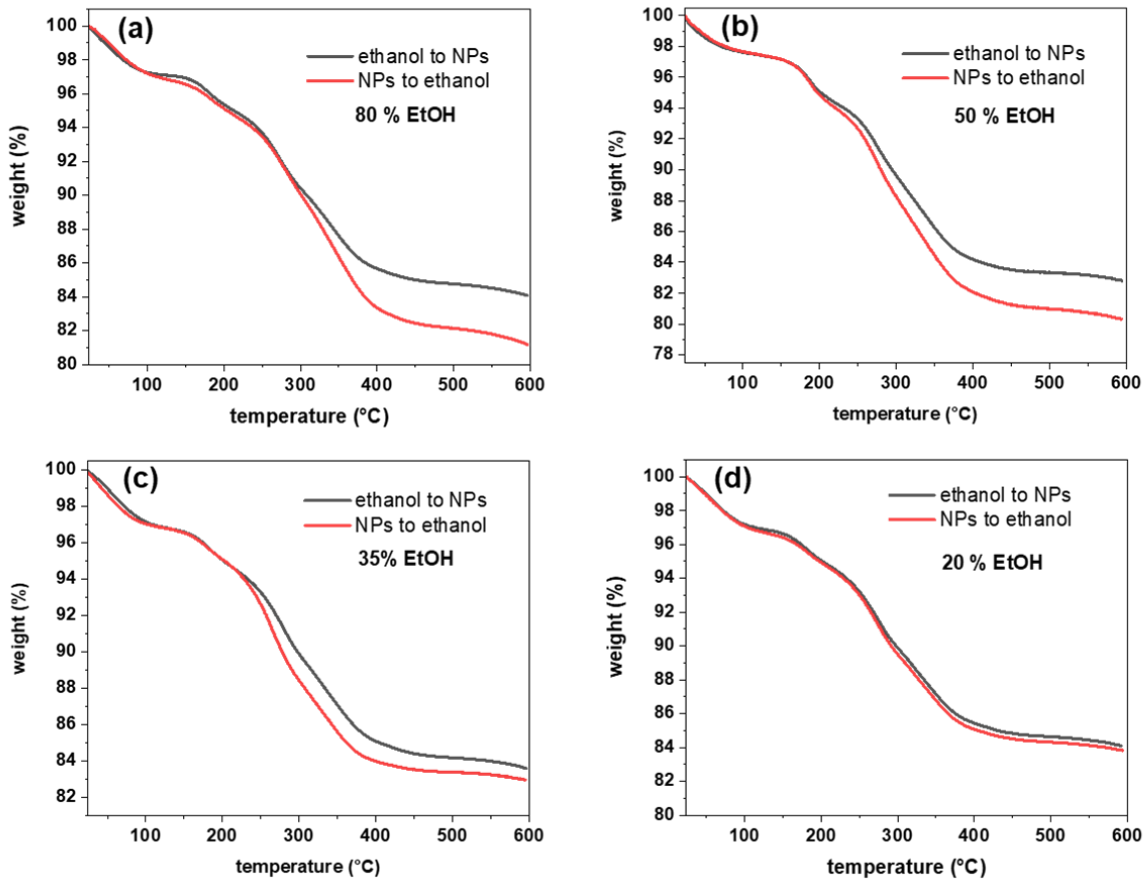

Figure 5.4. TGA of Fe_3O_4 NPs initially in hexanes after ligand stripping with (a) 80 v% (b) 50 v%, (c) 35 v% and (d) 20 v% ethanol for two different sequences of mixing NPs with ethanol.

The concentration of ethanol also influences ligand stripping. Increasing the ethanol concentration is expected to promote ligand stripping. However, agglomeration could shield ligand stripping at high ethanol concentrations. Therefore, we developed the following protocol to study ligand stripping with incremental addition of ethanol, where each sample has a total volume of 3 mL. From 10 mL of the stock NP solution in hexanes, 2 mL was taken in a glass vial and followed by adding 1 mL of hexanes to the vial, the 0 v% ethanol sample. 0.421 mL of ethanol was added slowly to remaining 8 mL of the NP stock solution under magnetic stirring. 2.1 mL of the resulting mixture was transferred to another glass vial, to which 0.9 mL of 5 v% ethanol was then added,

resulting in the 5 v% ethanol sample. To the remaining 6.32 mL of partially diluted stock solution, 0.351 mL of ethanol was slowly added to achieve 10 v% ethanol. To 2.22 mL of this 10 v% ethanol NP solution in a separate vial, 0.78 mL of 10 v% ethanol was added, resulting in the 10 v% sample. A similar approach was followed to prepare samples with a higher concentration of ethanol. During sample preparation, the total volume and concentration of NPs were kept identical to eliminate all variables except for the solvent concentration. Each NP solution was magnetically stirred for two hours before centrifuging (Thermo Scientific Sorvall Legend X1R with Fiberlite F15-6x100y rotor) at 12,500 rpm (17120 *g*) for 90 min and followed by removing the supernatant and drying the solid in a fume hood. TGA was performed to measure the fraction of NPs and ligands present in the pellet.

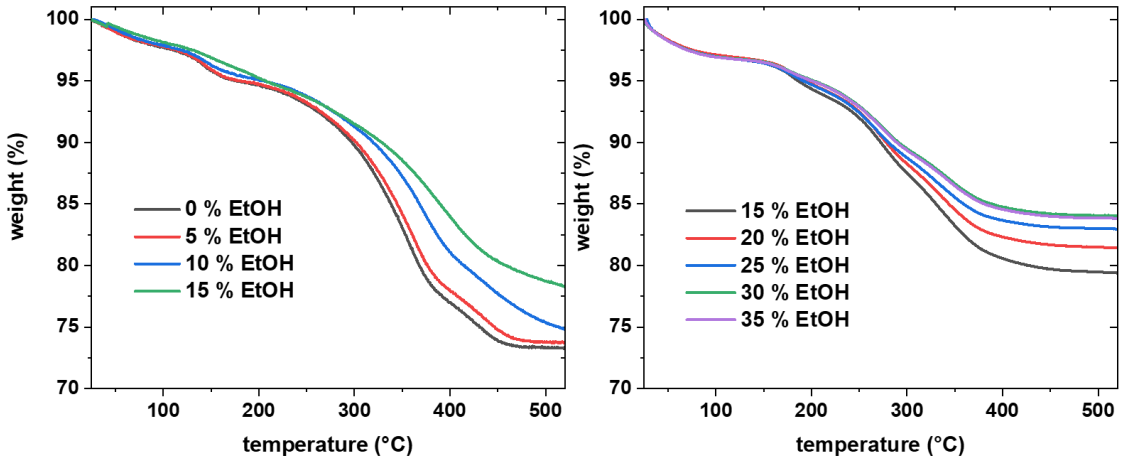

Figure 5.5. TGA of ligand-stripped Fe_3O_4 NPs prepared using different concentrations of ethanol.

When increasing the concentration of ethanol used in ligand stripping experiments, the weight loss in TGA measurements decreases, which is attributed to stripping more ligands.

5.5. References

(1) Song, J.; Rizvi, M. H.; Lynch, B. B.; Ilavsky, J.; Mankus, D.; Tracy, J. B.; McKinley, G. H.; Holten-Andersen, N. Programmable Anisotropy and Percolation in Supramolecular Patchy Particle Gels. *ACS Nano* **2020**, *14*, 17018-17027.

(2) Song, J.; Zhang, Q.; de Quesada, F.; Rizvi, M. H.; Tracy, J. B.; Ilavsky, J.; Narayanan, S.; Del Gado, E.; Leheny, R. L.; Holten-Andersen, N.; McKinley, G. H. Microscopic dynamics underlying the stress relaxation of arrested soft materials. *Proceedings of the National Academy of Sciences* **2022**, *119*, e2201566119.

(3) Yadav, P. R.; Rizvi, M. H.; Kuttich, B.; Mishra, S. R.; Chapman, B. S.; Lynch, B. B.; Kraus, T.; Oldenburg, A. L.; Tracy, J. B. Plasmon-Coupled Gold Nanoparticles in Stretched Shape-Memory Polymers for Mechanical/Thermal Sensing. *ACS Applied Nano Materials* **2021**, *4*, 3911-3921.

(4) Li, S.; Rizvi, M. H.; Lynch, B. B.; Tracy, J. B.; Ford, E. Flexible Cyclic-Poly(phthalaldehyde)/Poly(ε-caprolactone) Blend Fibers with Fast Daylight-Triggered Transience. *Macromol. Rapid Commun.* **2021**, *42*, 2000657.

(5) Heuer-Jungemann, A.; Feliu, N.; Bakaimi, I.; Hamaly, M.; Alkilany, A.; Chakraborty, I.; Masood, A.; Casula, M. F.; Kostopoulou, A.; Oh, E.; Susumu, K.; Stewart, M. H.; Medintz, I. L.; Stratakis, E.; Parak, W. J.; Kanaras, A. G. The Role of Ligands in the Chemical Synthesis and Applications of Inorganic Nanoparticles. *Chem. Rev.* **2019**, *119*, 4819-4880.

(6) Fu, J.; He, L.; Xu, W.; Zhuang, J.; Yang, X.; Zhang, X.; Wu, M.; Yin, Y. Formation of colloidal nanocrystal clusters of iron oxide by controlled ligand stripping. *Chem. Commun.* **2016**, *52*, 128-131.

(7) Mohrhusen, L.; Osmić, M. Sterical ligand stabilization of nanocrystals versus electrostatic shielding by ionic compounds: a principle model study with TEM and XPS. *RSC Advances* **2017**, *7*, 12897-12907.

(8) Xu, Z.; Shen, C.; Hou, Y.; Gao, H.; Sun, S. Oleylamine as Both Reducing Agent and Stabilizer in a Facile Synthesis of Magnetite Nanoparticles. *Chem. Mater.* **2009**, *21*, 1778-1780.

(9) Lan, F.; Bai, J.; Wang, H. The preparation of oleylamine modified micro-size sphere silver particles and its application in crystalline silicon solar cells. *RSC Advances* **2018**, *8*, 16866-16872.

CHAPTER 6. Conclusion and Outlook

Colloidal self-assembly is a versatile technique for synthesizing multicomponent nanostructures. The thesis presents an electrostatic core/satellite assembly technique for composite NPs with different types of core and satellite NPs functionalized with anionic BSA and cationic PEI that have good colloidal stability. Multiple layers of satellite NPs are reported. The assembly technique is sensitive to pH, which offers vast tunability and reversibility of assembly with pH. Core/satellite assembly with optimized sizes of GNRs and Fe_3O_4 NPs allows significant alignment of the MagGNRs under modest magnetic fields. This development allows magnetic manipulation without degrading the optical properties. MagGNRs have potential applications in multimodal imaging, therapy, and drug delivery.

Future studies could investigate assembly with other types of NPs as core and satellite NPs. For example, incorporating quantum dots as satellite NPs could be useful for probing and controlling plasmon-exciton coupling. Besides pH, the molecular weight of PEI could be another lever for controlling assembly. Moreover, changing the molecular weight might allow control over the distance between core and satellite NPs, which could tune the strength of the interaction between core and satellite NPs. Using microfluidics for assembly and purification could be useful for further tailoring the properties of core/satellite NPs and possibly for scaling up the method for applications.

Another important aspect that needs further investigation is the stability of the assembled core/satellite NPs in high ionic strength solvents like buffers. Thermal stability might also be important for some applications like photothermal heating. Silica overcoating of the core/satellite NPs might impart stability at higher temperatures and could control the solubility in different solvent environments.

Magnetic alignment of MagGNRs of different aspect ratios is promising for colorimetric applications, and further optimization is required to achieve significant alignment of MagGNRs with LSPRs in the visible spectrum. Increasing the size of Fe_3O_4 satellite NPs while maintaining superparamagnetic properties might provide improved alignment without agglomeration. Coupling magnetic alignment with photothermal heating could give magnetically modulated photothermal heating. Alignment of MagGNRs could also potentially be integrated with 3D printing processes. Use of magnetic fields to pattern the alignment of MagGNRs might also be useful for obtaining structures with novel chiroptical properties.